

Process and Structural Health Monitoring of Composite Structures with Embedded
Fiber Optic Sensors and Piezoelectric Transducers

by

Casey James Keulen

B.Eng., University of Victoria, 2005

M.A.Sc., University of Victoria, 2007

A Dissertation Submitted in Partial Fulfillment of the
Requirements for the Degree of

DOCTOR OF PHILOSOPHY

in the Department of Mechanical Engineering

© Casey James Keulen, 2012

University of Victoria

All rights reserved. This dissertation may not be reproduced in whole or in part, by
photocopying or other means, without the permission of the author.

Process and Structural Health Monitoring of Composite Structures with Embedded
Fiber Optic Sensors and Piezoelectric Transducers

by

Casey James Keulen

B.Eng., University of Victoria, 2005

M.A.Sc., University of Victoria, 2007

Supervisory Committee

Dr. Afzal Suleman, Supervisor

(University of Victoria, Department of Mechanical Engineering)

Dr. Mehmet Yildiz, Supervisor

(Sabanci University, Faculty of Engineering and Natural Sciences)

Dr. Martin Byung-Guk Jun, Departmental Member

(University of Victoria, Department of Mechanical Engineering)

Dr. Nikitas Dimopoulos, Outside Member

(University of Victoria, Department of Electrical and Computer Engineering)

Supervisory Committee

Dr. Afzal Suleman, Supervisor

(University of Victoria, Department of Mechanical Engineering)

Dr. Mehmet Yildiz, Supervisor

(Sabanci University, Faculty of Engineering and Natural Sciences)

Dr. Martin Byung-Guk Jun, Departmental Member

(University of Victoria, Department of Mechanical Engineering)

Dr. Nikitas Dimopoulos, Outside Member

(University of Victoria, Department of Electrical and Computer Engineering)

ABSTRACT

Advanced composite materials are becoming increasingly more valuable in a plethora of engineering applications due to properties such as tailorability, low specific strength and stiffness and resistance to fatigue and corrosion. Compared to more traditional metallic and ceramic materials, advanced composites such as carbon, aramid or glass reinforced plastic are relatively new and still require research to optimize their capabilities. Three areas that composites stand to benefit from improvement are processing, damage detection and life prediction. Fiber optic sensors and piezoelectric transducers show great potential for advances in these areas. This dissertation presents the research performed on improving the efficiency of advanced composite materials through the use of embedded fiber optic sensors and surface mounted piezoelectric transducers.

Embedded fiber optic sensors are used to detect the presence of resin during the injection stage of resin transfer molding, monitor the degree of cure and predict the remaining useful life while in service. A sophisticated resin transfer molding

apparatus was developed with the ability of embedding fiber optics into the composite and a glass viewing window so that resin flow sensors could be verified visually. A novel technique for embedding optical fiber into both 2- and 3-D structures was developed. A theoretical model to predict the remaining useful life was developed and a systematic test program was conducted to verify this model.

A network of piezoelectric transducers was bonded to a composite panel in order to develop a structural health monitoring algorithm capable of detecting and locating damage in a composite structure. A network configuration was introduced that allows for a modular expansion of the system to accommodate larger structures and an algorithm based on damage progression history was developed to implement the network.

The details and results of this research are contained in four manuscripts that are included in Appendices A-D while the body of the dissertation provides background information and a summary of the results.

Contents

Supervisory Committee	ii
Abstract	iii
Table of Contents	v
List of Tables	vii
List of Figures	viii
Acknowledgements	x
Dedication	xii
1 Introduction	1
1.1 Introduction	1
1.2 Motivation	2
1.3 Objectives	3
1.4 Organization of Dissertation	4
2 State of the Art Review	6
2.1 Flow Monitoring	6
2.2 Cure Monitoring	8
2.3 Lamb Wave Based Structural Health Monitoring	14
2.4 Remaining Useful Life Prediction	19
3 Summary of Contributions	23
3.1 Process Monitoring	23
3.1.1 Experimental RTM Apparatus	24
3.1.2 Fiber Optic Ingress/Egress	25

3.1.3	Development of Etched Fiber Sensor	26
3.1.4	Flow Monitoring	27
3.1.5	Cure Monitoring	31
3.2	Structural Health Monitoring	33
3.2.1	Hex Network	34
3.2.2	Damage Location Algorithm	35
3.2.3	Experimental Investigation	37
3.3	Prediction of Remaining Useful Life	40
3.3.1	Theoretical Development	41
3.3.2	Experimental Verification	45
4	Conclusions and Future Work	54
	Bibliography	58
A	Multiplexed FBG and Etched Fiber Sensors for Process and Health Monitoring of 2-&3-D RTM Components	69
B	An Experimental Study on the Process Monitoring of Resin Transfer Molded Composite Structures Using Fiber Optic Sensors	70
C	Damage Detection of Composite Plates by Lamb Wave Ultrasonic Tomography with a Sparse Hexagonal Network Using Damage Progression Trends	71
D	Prediction of Fatigue Response of Composite Structures by Monitoring the Strain Energy Release Rate with Embedded fiber Bragg Gratings	72

List of Tables

Table 3.1	Fatigue test data	48
Table 3.2	Fatigue life prediction results	49

List of Figures

Figure 1.1	Life of smart composite structure	5
Figure 2.1	Typical FBG data during cure cycle [62]	13
Figure 2.2	Hybrid EFPI/FBG sensor	14
Figure 2.3	Symmetric S_0 wave (top) and anti-symmetric A_0 wave (bottom)	15
Figure 2.4	Various PZT transducers	16
Figure 3.1	Layout and schematic of RTM apparatus	24
Figure 3.2	a) Through thickness ingress/egress arrangement (left) and b) schematic of fiber sealing (right)	26
Figure 3.3	a) Looped etched fiber sensor (left) and b) etching jig (right) .	27
Figure 3.4	a) Interrogation system (left) and b) sensors in RTM prior to injection (right)	28
Figure 3.5	CW from top left: a) resin approaching sensor, b) resin just after contacting sensor, c) mold midway through injection . . .	29
Figure 3.6	Photo-diode output vs. injection time for panel	29
Figure 3.7	Semicircular tube with embedded fiber optic sensors	30
Figure 3.8	Plot of photo-diode output vs. injection time for tube	30
Figure 3.9	CW from top left: Bragg wavelength vs. time during injection and cure of RTM process: a) first, b) second and c) third experiments)	31
Figure 3.10	Etched fiber sensor data recorded throughout the RTM process	33
Figure 3.11	Degree of cure as a function of time	33
Figure 3.12	a) Hexagonal network showing actuator-sensor paths from transducer A (left) and b) expansion of a single unit cell (right) . . .	34
Figure 3.13	a) Composite panel with hex network (left), b) hex network with induced damage (right)	37
Figure 3.14	a) Recieved Lamb wave signals at all seven damage states along path $A-G$ (left) and b) close up of A_0 wave (right)	39

Figure 3.15 a) SDC results with no damage progression factor (left) and b) SDC results with a damage progression factor of 1.10 (right) *Damage location indicated by yellow cross, colorbar indicating value of P from equation (3.1)	40
Figure 3.16 a) Power amplitude results with no damage progression factor (left) and b) Power amplitude results with a damage progression factor of 1.10 (right) *Damage location indicated by yellow cross, colorbar indicating value of P from equation (3.1)	40
Figure 3.17 Expanded strain energy during fatigue loading	41
Figure 3.18 a) Variation of energy release rate (left) and b) ε - N plot (right)	48
Figure 3.19 a) Wavelength vs. time for five second intervals at the beginning and b) end of the test	50
Figure 3.20 Wavelength and strain vs. stress	50
Figure 3.21 a) Results for Specimen 3-1: strain data (left) and b) prediction of remaining cycles (right)	51
Figure 3.22 a) Results for Specimen 4-2: strain data (left) and b) prediction of remaining cycles (right)	52
Figure 3.23 Temperature and load vs. percent of test	53

ACKNOWLEDGEMENTS

I would like to thank:

Dr. Afzal Suleman, my co-supervisor for both my Master's and PhD degrees for his advice and support both academically and professionally over the past seven years. Thank you for offering me this fantastic opportunity to continue my education.

Dr. Mehmet Yildiz, my co-supervisor for both my Master's and PhD degrees for his advice, guidance and input into virtually every aspect of my research. I especially thank him for his invitation to work under him in his lab at Sabanci University in Istanbul, Turkey for four months. It was an amazing experience for me both academically and personally that gave me insight into a culture and way of life I was not familiar with. I thank you very much.

Department of Mechanical Engineering, University of Victoria, for allowing me to pursue my education and obtain my degrees. The professors are inspirational and the facilities are terrific. I would also like to specifically thank both Sandra and Art Makosinski for their support with everything from op-amps to red bean cakes.

TUBITAK, Sabanci University and Istanbul Technical University, For funding, hosting and allowing me access to their world class facilities. The skills and experience I gained there will be highly beneficial to me for the rest of my career. I will never forget the five to six hour daily round trip commute from Sabanci University to Istanbul Technical University.

My colleagues at UVic, Kerem Karakoc, Baris Ulutas, Ricardo Paiva, Andre Carvalho, Bruno Rocha and Joana da Rocha for their support, assistance and friendship.

The Advanced Composites and Polymer Processing Lab, at Sabanci University and the colleges I had the pleasure of working with while there: Fazli Fatih Melemez, Talha Boz, Pandian Chelliah and Ataman Deniz. I hope we continue to work together in the future.

My family and friends, for providing support and more importantly a chance to forget all about my studies and relax every once in a while.

My wife Aissa Keulen, for her relentless support and encouragement for me to pursue my dreams academically, professionally and personally. And the personal sacrifices she has made to allow me to do this.

To all of you, Thank you!

Casey Keulen

DEDICATION

To Gail, John and Aissa

Chapter 1

Introduction

1.1 Introduction

Composite materials are becoming increasingly more valuable in a plethora of engineering applications because they offer advantages over traditional metallic materials like low specific strength and stiffness, good fatigue resistance, excellent corrosion resistance and highly tailorable physical properties. They are standard materials in aerospace, rail, marine, wind energy, pressure vessels and sporting equipment and are currently making their way into many more applications. A recent study by the Freedonia Group Inc. estimates that the demand for high performance composites will rise almost 15% per year to reach \$10.2 billion in 2016 in the United States alone [39].

Two major drawbacks of composites however, are the relatively difficult processing characteristics and damage assessment. A major drawback of liquid composite molding occurs during the resin injection stage. Due to a high resistance to resin (a relatively viscous material) flow through the fiber reinforcement (a material with low permeability) and geometry changes throughout the mold, it is not always possible to achieve a uniform flow pattern through the mold [81]. This can lead to regions of the mold that do not become fully saturated with resin known as 'dry spots', which have a profound effect on the physical properties of the composite. If the degree of cure is known in real time then the composite may be removed from the mold at the optimal time however, the degree of cure is not easily known without intrusive instrumentation that degrades the integrity of the structure. Another drawback lies in the difficulty of assessing damage. For example internal flaws may be present that are not

visible. These defects may grow, leading to catastrophic failure with little warning. With traditional inspection methods it is difficult, time consuming and expensive to detect and assess damage.

To mitigate some of these drawbacks, sensors and transducers can be embedded within or bonded to the surface of the material and used for process monitoring, structural health monitoring and remaining useful life prediction. Fiber optics can be embedded within the material and used to sense various parameters during processing and service. These measurements can then be used to assess the quality of the composite and predict the remaining useful life. Networks of piezoelectric transducers bonded to the surface can be used to detect and locate flaws in real time, thereby reducing the need for regularly scheduled inspection. Composites utilizing these techniques are generally referred to as 'smart composites'.

The life of a smart composite structure is described in Figure 1.1. Essentially there are three main stages: conception and design, manufacturing and service. The conception and design phase involves the design, specification and requirements of the composite as well as the design of the sensing technique such as sensor selection, sensing technique/algorithm and sensor location. Once the conception and design stage is complete the structure is ready to be manufactured. During this stage the mold, materials and equipment are prepared, the resin is injected into the mold, the resin is cured and the structure is demolded and finished. Once manufactured, it is put into service. Inevitably, the structure will be under loading and environmental changes that will affect its integrity. At some point it may be damaged. At this point the presence and severity of the damage must be assessed and a decision to ignore, repair or retire the structure must be made.

The research presented in this dissertation utilizes fiber optic sensors and piezoelectric transducers at each stage of a composite structure's life to monitor the process and structural health to improve the efficiency of the structure. The contributions include the development of manufacturing techniques and sensor/transducer systems with theories and algorithms to support them.

1.2 Motivation

The two driving motivators behind this research are human safety and accurate assessment of manufacturing and operational parameters to enhance efficiency. It is of utmost importance that the structural integrity of critical composite structures

is accurately known to ensure the safety of those relying on them. Currently, manual inspection is carried out on a routine schedule, costing operators a great deal of money. Also, many structures are simply replaced after a predetermined number of service cycles resulting in the potential for perfectly good structures to be discarded while those that develop flaws or damage prematurely are left in operation. Due to the numerous processing variables that can contribute to flaws in the material during manufacture, regulatory bodies have imposed high safety factors. This detracts from their light-weight benefits and adds to the cost as more constituent material is required.

With composite materials, failure is often rapid and catastrophic due to its non-ductile nature. Various types of damage can occur (fiber fracture, matrix cracking, fiber buckling, fiber-matrix interface failure, delamination, etc.) and interact to cause a number of failure modes [33]. With real-time knowledge of the existence of these flaws, the operator can react appropriately to ensure safety and economic efficiency. Flaws may exist depending on the processing method and operating parameters. If undetected, structures with these flaws can go into service with the potential of detrimental consequences.

If the properties of a composite structure could be monitored in real time to ensure initial quality during the manufacturing stage, detect damage while in service and predict the remaining useful life, composite structures could be designed to be much more efficient and be utilized to their full capacity.

1.3 Objectives

The overall objective of this work is to research and develop techniques for increasing the manufacturing and operating efficiency and reliability of composite structures by employing integrated sensor/transducer networks. Embedded fiber optic sensors and piezoelectric transducers are used for this purpose to achieve the overall objective.

The first sub-objective is to enhance the processing stage by employing a combination of embedded fiber Bragg grating (FBG) sensors and etched fiber sensors multiplex on a single optical fiber. The embedded fiber optic sensors will detect the presence of resin during the injection stage of a resin transfer molding process and subsequently monitor the degree of cure.

The second sub-objective is to develop an integral structural health monitoring system to detect the presence and location of damage in a structure using a network

of piezoelectric transducers based on tomography. Advancements and contributions are made to the current state of the art of these systems by introducing an algorithm that makes use of data from previous damage states and applying it to a modular sparse network that can be expanded to cover large areas.

The third sub-objective is to develop a technique to predict the remaining useful life of a composite structure under fatigue loading based on information gathered from embedded fiber Bragg grating sensors. The technique will use the previous loading history of the structure to calculate the remaining useful life on a cycle-by-cycle basis to give an estimate of the number of remaining cycles to failure.

1.4 Organization of Dissertation

The bulk of the work is contained in the Appendices. Each of the four Appendices contains a journal manuscript based on the work outlined in the dissertation with the objectives corresponding to the aforementioned sub-objectives. The organization of the dissertation is as follows:

- Chapter 1 presents an introduction and brief background to the dissertation along with the motivation and objectives of this work.
- Chapter 2 provides a state of the art review to bring the reader up to speed with recent advancements.
- Chapter 3 presents a summary of the specific contributions made in each manuscript and a brief explanation of their value.
- Chapter 4 concludes the dissertation by briefly summarizing the work completed and contributions made along with suggestions for future work in the area.

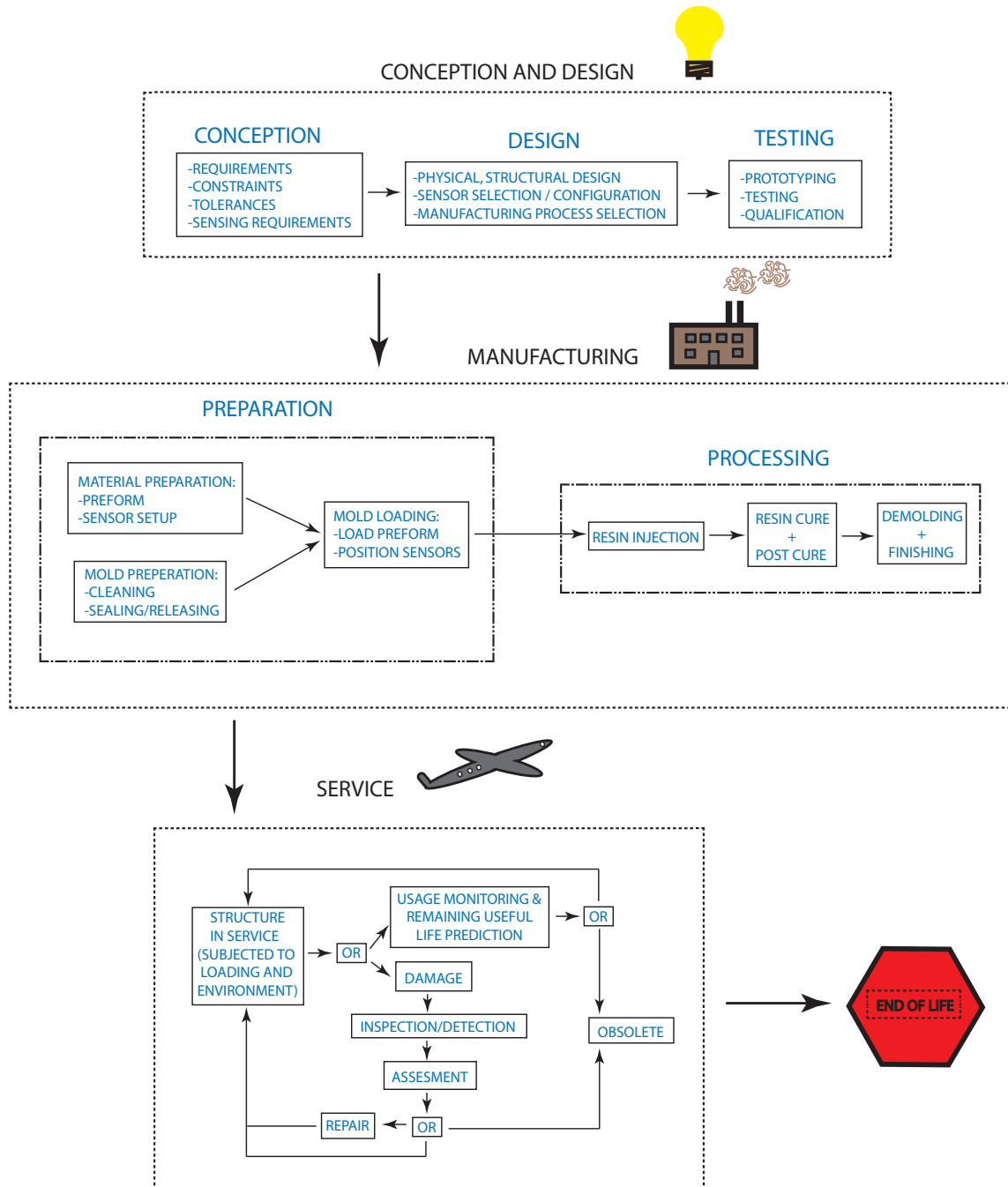


Figure 1.1: Life of smart composite structure

Chapter 2

State of the Art Review

This chapter presents a state of the art review in order to give the reader enough information to appreciate the material presented in the later chapters.

2.1 Flow Monitoring

Embedded fiber optic sensors have been utilized in a number of applications in the field of liquid composite molding (LCM), which includes composite material processing techniques such as resin transfer molding (RTM) and vacuum assisted resin transfer molding (VARTM). Some fiber optic sensors have the ability to sense the presence of resin. These sensors can be embedded inside the fiber reinforcement to sense when the resin has completely saturated the part. With this knowledge the infusion can continue until the sensors indicate that the part is complete before the infusion is stopped, ensuring full saturation. This reduces wasted material due to excess resin being pumped into the mold or parts that are not fully saturated and must be discarded. Also, this gives the manufacturer a higher degree of certainty that the parts are free of non-visible resin voids, which results in a reduction in quality assurance requirements. Taking this technique one step further, processing could be automated by integrating the sensors with a control system to automate the mold by opening and closing inlets and outlets in order to optimally infuse the part, allowing the resin to cure and automatically unloading the part.

Mainly due to the wide spread use of prepreg materials in aerospace, resin flow front detection has been investigated less than cure and health/damage monitoring however, many researchers have used fiber optics to detect the flow front of resin

during LCM processes.

Ahn, S.H. et al [2] used etched fiber sensors (EFS) to detect the arrival of resin at various locations within a fiber reinforcement preform in order to determine its 3D permeability. The sensors were embedded in a transparent RTM mold so that results could be verified by visual inspection. These results enabled the authors to verify their derived expressions for 3D permeability of the preform.

Lekakou, C. et al [52] used sensors that consist of simply the fiber optic core with an acrylic coating. They investigated two arrangements; one that had periodic sections of the coating removed (similar to EFSs) and another with the entire coating removed completely exposing the core. The latter arrangement allowed the resin position to be monitored continuously, rather than discretely allowing for a potentially more accurate system.

Bernstein, J.R. et al [5] published their results on the development of a fiber optic sensor for monitoring the flow in a VARTM process. The sensor operates by measuring the reflectivity from small gaps in a length of optical fiber. Each gap is created by placing the ends of two cleaved fibers into a groove in a piece of polycarbonate. Initially, light is launched down the fiber; some light bridges the gap and continues through the next fiber while some light is reflected. As resin fills the gap more light is transmitted down the fiber and less light is reflected back. Since light is still transmitted, a number of sensors may be multiplexed on a single fiber. An optical time domain reflectometer (OTDR), a device that sends a pulse of light down the fiber and records the magnitude of the reflections over time is used to interrogate the sensor network and differentiate the sensors. Their initial testing proved the ability of the sensors to detect resin flow in a VARTM process.

Resin film infusion is a process where a thermoset resin film is placed between a mold and fiber reinforcement. The film/fiber/mold is enclosed under a vacuum bag and heated to allow the film to become liquid, flow through the fiber and cure. Antonucci, V. et al [3] used a Fresnel sensor to monitor the flow of resin during a resin film infusion process (RFI). A Fresnel sensor simply consists of a cleaved end of optical fiber. Measurements are made based on the intensity of light reflected from the cleaved end, which is a function of the refractive medium it is surrounded by.

Dunkers, J.P. et al [18] developed a fiber optic real time system to sense resin at various locations on a single fiber using two, long-period gratings (LPG) and a polychromatic source. Long period gratings are similar in nature to FBGs however function differently as they couple light out of the core. When resin contacts the

LPG the light that would be coupled out of the core is contained thereby allowing more light to be transmitted. A single fiber with two LPGs was located inside an RTM mold, resin was injected and the sensors were monitored. An optical spectrum analyzer was used to scan the reflected spectrum and measure the wavelength and amplitude. This allowed for the flow front to be detected as well as the distinction between the two LPGs. The same sensors were later used for cure monitoring. The results show that LPGs can be used to reliably monitor the presence of resin.

Eum, S. et al [21] took a similar approach to Dunkers, using LPGs to monitor flow. In their research, they used optical frequency domain to interrogate the sensors along the length of the grating and short-time Fourier transformation to separate the presence of flow from compressive strain.

Fiber Bragg gratings have also been used for flow monitoring. Since FBGs are sensitive to both temperature and strain, the presence of resin causes a shift in wavelength due to flow-induced strain or a temperature differential.

Gupta, N. et al [32] used FBG sensors in a modified VARTM process to detect the presence of resin. Two techniques were used; the first involved simply inserting the FBGs into the laminate during the infusion and monitoring a wavelength shift, the second used an etched fiber sensor that was multiplexed with an FBG. The EFS was located inside the mold while the FBG was outside. Light was launched through the fiber, traveling through the EFS then FBG. The magnitude of the reflection from the FBG was monitored. At this point the magnitude is a function of the refractive index of the resin as it controls how much light passes through the EFS and reaches the FBG.

2.2 Cure Monitoring

Once a part is fully infused, the resin must cure before it may be removed from the mold. In most liquid composite molding techniques the cure phase takes the longest and is considered the bottleneck when trying to increase process efficiency. The chemical reaction that takes place when the resin is curing is exothermic, which means it produces heat. As the resin cures the temperature inside the part rises steadily until it reaches a peak then declines. With most resins, after the temperature has reached a maximum the part is ready to be removed from the mold thereby allowing the mold to be used for the next part. If the temperature inside the part is monitored, the peak may be detected and the part can be removed at an optimal

time, rather than a predetermined time, which may not be optimal depending on the atmospheric conditions such as temperature and humidity. Fiber optic sensors that sense temperature can be embedded in the part and used for this very purpose. Other parameters can also be used to monitor cure such as refractive index or viscosity.

A number of direct methods for monitoring the degree of cure currently exist [77]. Traditional methods are based on thermal and dynamic analysis. Other techniques include the addition of photochromic, thermochromic compounds, or other dyes to the resin. Changes of color, absorbance and transmittance as a function of time and temperature during cure can be monitored and correlation of spectral changes in the resin with polymerization and cross-link density can be made. Electrical resistance measurements and dielectric analysis techniques have also been successfully used to determine the completion of cure by monitoring capacitance, dissipation and DC electrical resistance of the resin.

The drawback of the aforementioned techniques is that they cannot make local measurements, only global. This is a concern as the degree of cure can vary throughout the composite due to factors such as thickness, fiber packing or thermal gradients induced by uneven mold heating. Some of these techniques also require the resin to be in a neat form (only resin, no reinforcement fiber) or the addition of chemicals that remain in the resin after cure that can negatively impact the composite. To overcome these issues, dielectric probes have been designed that measure the degree of cure in a local area. The disadvantage of these probes, however is that they are intrusive when embedded within the composite thereby rendering the composite unfit for service.

Fiber optic sensors are ideal for monitoring the cure as they can be embedded within the material with little to no effect on the host composite and make localized measurements [91]. A variety of fiber optic based sensors for this very purpose have been investigated.

Afromowitz, M.A. et al [1] reported on a novel technique to monitor the degree of cure based on the change in refractive index using an optical fiber sensor. The sensor consists of two lengths of conventional glass optical fiber with a third length of fiber bonded between the two that is composed of the polymer resin to be monitored. The sensor is placed in the polymer resin while in liquid form and light is launched into one end and monitored through the other. Initially the liquid polymer resin and cured polymer fiber have different refractive indices thereby allowing light to transfer through the fiber. As the cure progresses the refractive index of the polymer resin approaches that of the polymer fiber and allows more light to escape until full cure,

at which point the polymer fiber cannot transfer light because the fiber and resin are essentially one homogeneous material. The advantage of this type of technique is that the sensor imposes little to no effect on the polymer it is monitoring since it is the same material once cured. The disadvantage is that it is not practical to produce a small polymer fiber for each type of polymer one wishes to monitor.

In the early 1990s, various researchers [63, 54, 55] used Raman spectroscopy to monitor the cure of neat epoxy with a fused-silica distal mode optical fiber sensor that monitors a volume of material in the shape of a cone at the fiber terminus. This technique was applied to liquid molding of a high volume fraction composite however, it was in a form that required the user to insert the distal end of the fiber into a Teflon tube that had been previously filled with the epoxy mixture which renders the molded part useless. Furthermore, the researchers suggest that the determination of percent cure was not as precise as the laboratory sample mainly due to the fluorescence from surrounding glass fibers, which contributed to a higher background reading.

Davis, A. et al [13] reported on an acoustic based technique for cure monitoring that uses fiber optic sensors to detect ultrasonic waves that are generated in the material. The technique uses a laser that sends a pulse of light through a fiber optic that has a terminated end directed at the surface of the epoxy. The pulse is absorbed and results in localized heating which creates a thermoelastic expansion leading to the generation of ultrasonic waves. The speed of the waves is monitored by a Michelson interferometer with one arm embedded in the resin. As the resin cures, the ultrasonic wave speed increases. Fomitchov, P.A. et al [24] developed a similar system that was integrated into a resin transfer molding apparatus. The system consists of a fiberized laser ultrasonic source and an embedded ultrasonic sensor based on an intrinsic fiber optic Sagnac interferometer. Bulk ultrasonic waves are generated by the laser source, through the composite and detected by the sensor.

A number of researchers have used fluorescence monitoring sensors to detect the extent of cure in polymer based composites [53, 7, 12, 71]. While Wang, F.W. et al [96] rejected intrinsic fluorescence monitoring because they observed batch-to-batch variations in their spectral response and the approach could not be generalized to other epoxy systems, others have continued research. Levy, R.L. et al [53] developed a fluorescence based fiber optic sensor that they used to monitor changes in the intrinsic fluorescence intensity of carbon fiber/epoxy laminates during cure in an autoclave. While curing in the autoclave the intensity of the signal peaked then declined. They attributed this result to an instrumental effect and suggested that an

empirical relation based on signal intensity could be developed. They also observed shifts in the wavelength of the fluorescence emission maximum and correlated this signal with the degree of cure for the late stages of isothermal cure. Their later work involved developing the sensor to have two roles: monitoring the cure and the absorbed water content in the fully cured composite while in service. The absorbed water content varies as a function of temperature and humidity and has an impact on the expansion and strength of a composite. Paik, H.J. et al [71] also used a fiber optic probe with a fiber optic fluorimeter to monitor the intrinsic fluorescence of an epoxy cure reaction by doping the resin with trace levels of fluorescence.

Research has also been done on the use of evanescent wave for cure monitoring. In 1996, Crosby, P.A. et al [10] demonstrated the feasibility of using evanescent wave spectroscopy and refractive index based optical fiber sensors for epoxy resin. Data from the sensors was compared to conventional test results from differential scanning calorimetry (DSC). The results show that both sensors accurately monitor the degree of cure. The evanescent wave spectroscopy based sensors can be used to obtain quantitative information on the actual concentrations of the active functional groups in the epoxy resin system while the refractive index based sensors are not capable of sensing direct information they are simpler and less costly to implement. Woerdeman, D.L. et al [102] developed a sensor based on an evanescent wave fluorescence measurement. The wavelength shifts were monitored during liquid molding and the monomer conversion was extracted from calibration curves. They later incorporated a CCD camera and fast detector to provide real-time monitoring of fast reacting resin systems [66].

Fernando, G.F. et al [23] developed a multi-purpose fiber optic sensor based on an extrinsic Fabry-Perot interferometer (EFPI). The sensor was developed to monitor the cure as well as detect the ingress of moisture in the cured resin, monitor vibration characteristics of impact damaged composites and separate strain and temperature measurements. A small slot was created in the cavity of a typical EFPI sensor to allow epoxy to enter. The power that was transmitted through the sensor was monitored to give an indication of the cure. Essentially the change in refractive index of the resin allowed for cure monitoring while still allowing the sensor to be used for the other aforementioned uses.

Cusano, A. et al [11] used a Fresnel sensor to monitor the cure of thermoset composites. A Fresnel sensor simply consists of a cleaved end of optical fiber. Measurements are made based on the intensity of light reflected from the cleaved end,

which is a function of the refractive medium it is surrounded by.

Dunkers, J.P. et al [18] used an LPG to monitor the cure of epoxy resin. LPGs are similar in nature to FBGs however function differently as they couple light out of the core. When immersed in a medium the amount of light coupled back into the core is a function of the refractive index of that medium. A fluorophore was grafted to the exterior of the LPG to make it sensitive to the cure. By sensing the fluorescence intensity change and blue spectral shift the LPGs can monitor the cure.

Fiber Bragg gratings have been used extensively by various researchers for cure monitoring by [15, 62, 42] among others. This is partly due to the fact that if implemented appropriately, FBGs can be used for flow monitoring, cure monitoring and structural health monitoring [47]. Most techniques focus on the structural health monitoring considering the process monitoring a secondary bonus.

Dunphy, J.R. et al [19] were among the first to investigate FBGs for cure and strain monitoring of composites in 1990. Murukeshan, V.M. et al [62] also investigated the potential of FBGs for cure monitoring. Their technique was to simply place the FBG inside the laminate and monitor the shift in Bragg wavelength during the curing process. No attempt was made to separate the effects of strain and temperature change, simply to monitor the overall effect on the FBG. Their results show that repeatable curves can be observed and suggest that a deviation from these curves indicate an anomaly in the cure process. Figure 2.1 shows a plot of the change in Bragg wavelength vs. time for various specimens. From the plot it can be observed that the Bragg wavelength initially goes through a steady linear increase, likely due to the temperature increase from the exothermic reaction. Then there is a period where the wavelength fluctuates. This is during the vitrification process when the resin is changing from a liquid to a solid and bonding to the optical fiber. The fluctuations are likely due to bonding/slipping at the resin/optical fiber interface. Eventually the fluctuations cease and the Bragg wavelength slowly decreases until it reaches a steady state. The decrease can be attributed to a decrease in temperature as the composite is releasing heat from the reaction. There will also typically be an offset from the initial Bragg wavelength that is attributed to internal strain in the composite.

Other properties related to the curing process have also been monitored such as pressure distribution, temperature and residual stress [77]. These properties are important to the quality, strength and performance of the final product.

Udd, E. et al [92] reported on a simple pressure sensor based on a microbend sensor that consists of a fiber optic sandwiched between two layers of fiber reinforcement;

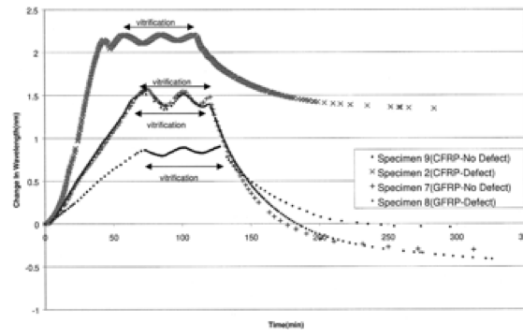


Figure 2.1: Typical FBG data during cure cycle [62]

a light source is connected to one end and a detector is connected to the other. As pressure on the laminate is increased, either within an autoclave or two-sided mold, the fiber is compressed between reinforcement fibers in the composite causing microbends which reduce transmitted light. The magnitude of the microbends is a function of pressure. Various types of fiber were tested and Corning 1521 single-mode fiber was found to be the most sensitive with a 20% loss in power with 2.07MPa of pressure.

In composite laminates residual stress can occur due to elevated cure/post cure temperatures. This is a result of the composite assuming a solid physical shape at a temperature greater than ambient, then put into service at ambient temperature or any temperature different from that of the cure/post cure.

In 1990, Dunphy, J.R. et al [19] were among the first to report on the use of fiber Bragg gratings for monitoring the development of residual stress.

Kalamkarov, A.L. et al [43] used an EFPI sensor to monitor the residual strain during a pultrusion process. They found that the strain after cooling was so great that it crushed the glass capillary tube. This resulted in the development of a reinforced sensor that was able to survive the process however less sensitive to temperature.

Kang, H.K. et al [44] used a hybrid EFPI/FBG sensor to monitor the temperature and development of strain during cure. Their sensor consists of a traditional EFPI with an FBG at the terminal end of the fiber that is connected to the instrumentation inside a capillary tube that creates the cavity of the EFPI as described in Figure 2.2. Since the FBG is shielded from strain, it is only sensitive to temperature change. This allows the strain and temperature reading from the EFPI to be separated. The disadvantage of this technique is that only one sensor may be used per fiber optic, a number of sensors cannot be multiplexed.

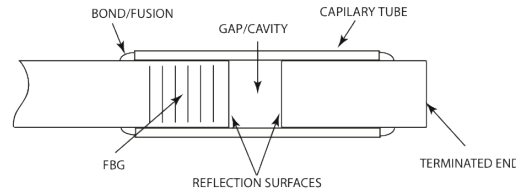


Figure 2.2: Hybrid EFPI/FBG sensor

2.3 Lamb Wave Based Structural Health Monitoring

Lamb waves have been used in nondestructive testing and evaluation (NDT&E) and structural health monitoring (SHM) applications since the 1960's [25, 104]. Detection schemes, reconstruction algorithms and transducers to utilize Lamb waves for these applications have all been extensively investigated [86, 75].

In the 1990's Hutchins, D.A. et al [40, 35, 41] and Nagata, Y. et al [64] were among the first to apply Lamb waves to NDE using medical imaging and seismic tomography techniques to both metallic and composite materials. Damage detection by ultrasonic waves is achieved through the emission of Lamb waves and acquisition of the response of the structure. A pulse-echo or pitch-catch scanning method is employed. The main applications are to beams and plates; since many aerospace systems can be modeled as these basic structural components they are ideal candidates for test specimens. Lamb waves are elastic, guided waves that propagate parallel to the surface in thin structures with free boundaries. Plates are the best example however, Lamb waves can also propagate in structures with a shallow curvature. The most advantageous characteristics of these waves are their susceptibility to interferences caused by damages or boundaries (the features of interest) and low amplitude loss.

When Lamb waves propagate they travel in one of two possible ways with respect to the plate's mid-plane. If the motion is symmetric about the mid-plane (the peaks and troughs of the waves are in phase) then it is a symmetric mode and if the motion is not symmetric (the peaks and troughs are 180° out of phase) it is an anti-symmetric mode. Figure 2.3 describes these modes looking from the side of a plate if the waves are traveling left or right. An infinite number of modes exist, each mode is referred to as an A mode or S mode if it is anti-symmetric or symmetric respectively, with a subscript indicating its order. For example the lowest order/frequency symmetric mode is referred to as an S_0 mode while the second lowest order/frequency anti-

symmetric mode is referred to as an A_1 mode. Each mode exists at a different frequency depending on the properties of the material. At lower frequency-thickness values less modes exist. It is advantageous to operate in a frequency-thickness range where only the S_0 and A_0 modes exist, which is generally below $1.5MHz\text{-}mm$.

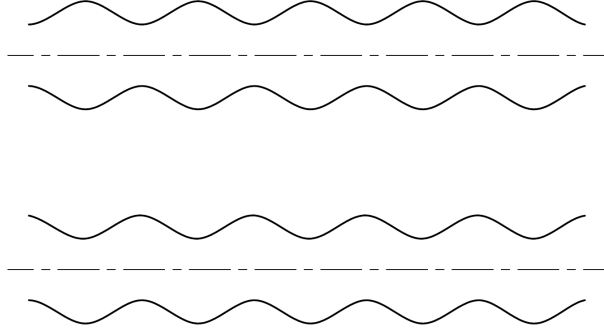


Figure 2.3: Symmetric S_0 wave (top) and anti-symmetric A_0 wave (bottom)

Numerous studies have been conducted to determine the optimal implementation of Lamb waves. A_0 and S_0 modes are favored due to the fact that they have clearly separated propagation velocities and can be generated without any other modes, as higher frequency ranges would include these modes as well as higher modes. Studies have shown that the S_0 mode performs better for internal defects like delaminations [27, 97, 79], while the A_0 mode is more sensitive to surface damages. By studying different configurations for sensor positioning, Su, Z. et al [85] concluded that mode separation can be achieved and as a result, it is possible to enhance the desired mode. Furthermore, when comparing the A_0 with S_0 mode, the latter presents a higher propagation velocity and lower attenuation, which makes it preferable.

Other studies are based on the most adequate waveform to activate Lamb waves. It has been determined that a narrow bandwidth signal with a finite number of peaks is best for avoiding wave dispersion and control the actuation frequency. Wilcox, P.D. et al [101] executed a deep study on this matter. Essentially, a balance between the wave packet duration and stimulated frequency precision must be established. Rocha, B. et al [78] concluded that a five peak sine burst modulated by a Hann window provided a reasonable compromise between a short signal and clear actuation of the desired frequency. Equation (2.1) describes the actuation signal.

$$f(t) = A \sin(2\pi f_t) \sin\left(\frac{2\pi f}{10} t\right) \quad (2.1)$$

Various actuators have been investigated and applied to Lamb wave actuation

and acquisition. Lead zirconate titanate (PZT) piezoelectric materials are the most widely used for transducers. Various transducers are shown in Figure 2.4 with a Canadian penny for reference ($\varnothing = 19mm$, $t = 1.45mm$). PZTs can be integrated into structures, are lightweight, present a wide actuation frequency range, require little power and can be manufactured in almost any conceivable shape and size. Since PZTs are piezoelectric they mechanically deform when subjected to a voltage differential and conversely, produce a voltage differential when deformed, allowing them to act as both actuator and sensor making them ideal for SHM applications [29, 72].



Figure 2.4: Various PZT transducers

Along with other properties PZTs are usually characterized by their strain constants: d_{ij} , where i is the polarization direction and j is the direction of strain. The larger the value of d_{ij} , the larger the strain for a given charge. For surface mounted PZT disks, d_{31} is the most important as it represents the strain constant for polarization along the PZT disk's normal axis with strain in the disk's plane direction. Size and shape are also critical and must be selected in order to achieve optimal results [103, 67]. Experiments and numerical simulations have been performed extensively. Giurgiutiu, V et al [28] studied the relationship between PZT transducer size and related actuation capacity. Mathematical and experimental results show that depending on transducer size, there are particular actuation frequencies that allow for the highest actuation amplitude possible. The durability of actuators and their response under extreme conditions like high/cryogenic temperatures and large strains have been investigated by researchers such as [9, 6].

Networks are a common technique for damage detection. They consist of groups of transducers that act together to detect damage. They often use waves reflected off damage to triangulate a location or construct a tomogram. Studies have been performed on network optimization, such as Chakrabarty, K. et al [8]. The main objective was to minimize a cost function that included coverage area and cost. Staszewski,

W.J. et al [84] conducted optimization for a network, seeking the best positioning and number of sensors for a direct wave analysis damage assessment. Other researchers have based their selection on mode shapes [31] and eigenvalues [89] of the test specimen as performance metrics. By numerical simulation on an aluminum structure, Lee, B.C. et al [50] determined that the sensor should be placed near the damage in order to detect it by analyzing the transmitted wave. In reality the damage location is unknown and therefore the reflection wave is the best indicator with sensors positioned near the border as the best arrangement.

Linear phased arrays are another technique used to detect damage. They consist of a number of transducers aligned in a linear arrangement that actuate waves sequentially with a short time delay such that the waves combine to produce a wave front that can be focused in a desired direction. The main advantage of this approach is that because the wave front is produced by constructive interference from a number of waves, it has a much greater magnitude than a single wave. The test specimen can be scanned for damage (similar to radar) by sweeping the wave front. Bao, J. [4] et al studied this approach in depth. By simulation and experiment with a phased array, Bao was able to detect the location of a $19mm$ crack.

There is a plethora of techniques used to analyze Lamb wave signals. The raw signal is acquired in the form of amplitude vs. time. Basic information such as wave modes, propagation velocities and boundary reflections can be extracted from this information with little processing. To obtain more information various processing methods are used such as the signal root-mean-square (RMS) and energy density by Hilbert transform. Still, further processing is necessary when comparing a baseline signal to a damaged one. Usually, normalization and data shifting is necessary to synchronize both responses. Michaels, J.E. et al [60] used both normalization and data shifting during a four network damage detection experiment on an aluminum plate. Using this approach and with sensors close to the damages created, $6.4mm$ holes, were successfully detected.

Time reversal is also used for damage location. It involves emitting the inverse of a sensed wave. Assuming that there is no damage present, the actuator (now acting as a sensor) should receive a signal very similar to the one initially sent. Baseline and damage comparison is not necessary. Sohn, H, et al [83] successfully applied this method for delamination detection on a composite panel. On the delaminated plate, the received signal mismatched the original created by the actuator. This approach also focuses its search on the direct paths established between sensor and actuator.

With this limitation only a relatively high density network or 1D specimen could be used however, very small damages can be detected. Prada, C. et al [73] was able to detect damages of $0.4mm$ on a $250mm$ diameter isotropic billet. Xu, B. et al [105] concluded that single mode tuning is the best way to enable the time reversal approach.

Mode separation and identification is the main reason for frequency domain analysis. Processing techniques include Fourier transform (FT), fast Fourier transform (FFT) and two-dimensional FFT (2D-FFT). The latter is used for identifying different modes. Joint time frequency domain analysis can be achieved by short-time Fourier transform, Wigner-Ville distribution (WVD) and wavelet transform (WT). By these methods, analysis conjugate both time and frequency variation along the timed response. The most commonly used is the WT. Kessler, S.S. et al [46] used WT to extract information from tests on a carbon fiber composite strip with damage in the form of a through hole, cracked matrix and delamination. Paget, C.A. et al [70] conducted experimental impact tests on a composite panel. WT was used to decompose the time-series data attained from the transducers. Relative coefficients changed accordingly from no damage to three increasing levels of impact energy providing useful information on damage assessment.

After signal acquisition and appropriate processing is performed, damage detection/location algorithms may be implemented. For networks, two algorithms are commonly used: pitch-catch and pulse-echo. Pitch-catch is based on the detection of the scattered wave caused by damage in the direct path between the actuator and sensor. The simplest approach involves creating a sufficiently dense grid established by numerous direct paths between every sensor pair available. Ihn, J.B. et al [38] successfully tested this technique on an Airbus aircraft panel. Cracks starting at $4mm$ were detected. The pulse-echo technique relies on the fact that the reflection produced by the damage can be retrieved by the sensors in the network. This approach requires a lesser number of transducers in comparison with pitch-catch. The shortcomings are related to damping causing the reflected waves to decrease below detectable level before reaching a sensor. Raghavan, A. et al [76] carried out tests for damage location using a network. Holes starting at $5mm$ in diameter, were detected and located. Rocha, B. et al [78] later detected through holes of $1mm$ in diameter and slots $2mm$ long in an aluminum plate.

Tomography reconstruction is another technique that uses an array however, with this technique the array surrounds the detection area in a circular or rectangular

arrangement. One transducer actuates a wave while the others sense the wave, this is repeated until each transducer has had a chance to actuate. A number of studies have been conducted that use an array with tomography techniques to locate damage. Hutchins, D.A., et al was one of the first to employ Lamb wave tomography to detect damage [35, 41] however the technique required the part to be immersed in water. Prasad, S.M. et al [74] were among the first to use surface bonded transducers on composite materials to detect damage with Lamb wave tomography. Hay, T.R. et al [34] demonstrated the use of this technique to detect simulated corrosion on an aluminum plate. Velson, J.K. et al [94] demonstrated this technique on pipes thereby verifying its ability to operate on a curved surface. Michaels, J.E. et al [59] and Yan, F. et al [106] both investigated the use of a sparse network in order to reduce the number of transducers required. Various damage metrics have been used to construct tomograms. Time-of-flight and amplitude are the most commonly used however, various researchers [34, 94, 58, 57] have studied the signal difference coefficient (SDC) which is a statistical comparison between the damaged state and undamaged state. More recently Moustafa, A. et al [61] used the fractal dimension based on a modified box-counting algorithm.

2.4 Remaining Useful Life Prediction

Once a structure is put into a cyclic loading situation, a prediction of the remaining useful life is highly beneficial so that the operator knows the optimal time to take the structure out of service. Generally, life cycle predictions are made during the design process and not during service. On the other hand research has been done on detecting damage in real time (SHM). Little work however, has been done on bridging the gap between fatigue life prediction and SHM [111].

Research into the detection of damage using embedded fiber optic sensors has been performed by various researchers [49]. It appears that Doyle et al were among the first to monitor the reduction in stiffness of composites during fatigue with an FBG [17]. Many researchers attempt to characterize the change in the reflection spectrum of an FBG to detect and measure the density of cracks based on the fact that a non-uniform strain distribution along an FBG causes broadening of the reflected spectrum [87, 20, 110, 88, 86]. Epaarachchi, J.A. et al [20] used FBG sensors that operate in the near infrared region ($\sim 830nm$) to investigate fatigue of $[0/90]_{2S}$ glass fiber woven cloth/vinylester and concluded that this type of FBG responds the same as those in

the $1550nm$ range. Takeda, N. et al [87] attempted to correlate crack density with broadening of FBG spectrum using a theoretical model for crack density. Yashiro, S. et al [110] proposed a numerical approach to correlate the reflection spectrum of the embedded FBG sensor to damage. The approach consists of two parts; first the finite element method was used to predict the damage induced strain distribution in the FBG gage region then a numerical model was used to predict the change in the FBG reflection spectrum due to this strain distribution. Takeda, N. et al [88] proposed a method of addressing multiple damages near a stress concentration by a technique based on a layer-wise finite element analysis with cohesive elements for various cracks. The estimation procedure is based on the mathematical optimization as an inverse problem, not using an extensive database (e.g. experimental results).

On the other side of the problem, a considerable amount of research has been devoted to fatigue prediction modeling. In the past, researchers have shown that $S-N$ curves (stress range vs. number of cycles) of unidirectional FRP composites have virtually no clear threshold stress level as established in metals. Hence, life prediction models based on $S-N$ curves of unidirectional FRP composites may not be applicable for FRP composite materials [56]. It is recognized that a certain threshold level of strain in resin does exist for indefinite fatigue life however, it is very low, around 5-10% of the ultimate strain of the composite material [65].

The field of fatigue life modeling of composite materials is very extensive. The topic has been under research for over forty years and there is still no widely accepted model applicable to all situations that most engineers agree upon. Many excellent references that cover a variety of available models exist such as [33, 90, 14] among others.

Fatigue prediction models can be classified into three types: fatigue life models that do not take into account degradation mechanisms instead use $S-N$ curves, phenomenological models for residual stiffness/strength and progressive damage models [14]. The first type is referred to as fatigue life models. They extract information from $S-N$ curves and propose a failure criteria. They do not take into account the accumulation of damage; only predict the number of cycles to fatigue failure under given loading conditions. The second type, phenomenological models, attempt to describe the evolution of the strength or stiffness of the material. These are not classified as progressive damage models as they predict strength and stiffness based on macroscopically observable properties rather than actual damage mechanisms. The last type, progressive damage models, attempt to describe the deterioration of properties based

on underlying damage mechanisms that lead to macroscopically observable results. A subcategory of fatigue models referred to as cumulative damage models use the above three models to sum various damage or fatigue conditions to predict the remaining life.

One of the first fatigue life models was proposed by Hashin and Rotem [80] as:

$$\sigma_A = \sigma_A^u \quad \text{and} \quad \left(\frac{\sigma_T}{\sigma_T^u} \right)^2 + \left(\frac{\tau}{\tau^u} \right)^2 = 1 \quad (2.2)$$

where σ_A and σ_T are the stresses along the fibers and transverse to the fibers, τ is the shear stress and σ_A^u , σ_T^u and τ^u are the ultimate tensile, transverse tensile and shear stress, respectively. Because the ultimate strengths are functions of the fatigue stress level, stress ratio and number of cycles, the criterion is expressed in terms of three S - N curves that are determined experimentally. The criteria are only valid for laminates with unidirectional plies.

Much research was done on phenomenological models to predict the stiffness degradation of composites by Whitworth, H.A. et al [100, 98], and Yang, X.W. et al [107].

Along these lines, Hwang, W. and Han, K.S. introduced the fatigue modulus concept [37]. The fatigue modulus concept is described as the slope of applied stress and resultant strain at a specific cycle. The degradation rate of the modulus is assumed to follow a power function:

$$\frac{dF}{dn} = -Acn^{c-1} \quad (2.3)$$

where F is the fatigue modulus, n is the number of cycles and A and c are material constants. They assume that the applied stress σ_a varies linearly with the resultant strain such that: $\sigma_a = F(n_i)\varepsilon(n_i)$, where $F(n_i)$ and $\varepsilon(n_i)$ are the fatigue modulus and strain at loading cycle n_i , respectively. The strain life, N can be calculated by integrating (2.3) from $n_1 = 0$ to $n_2 = N$ and introducing the strain failure criteria, which states that failure occurs when the fatigue strain reaches the ultimate static strain to obtain: $N = [B(1 - r)]^{1/c}$, where $B = F_0/A$ and $r = \sigma_a/\sigma_u$ is the ratio of applied cyclic stress to ultimate static stress where c is a material constant.

Hwang, W. and Han, K.S. [36] also proposed three cumulative damage models based on the fatigue modulus. Lee, L.J. et al [51] used a stiffness degradation model to predict failure.

Whitworth, H.A. used the residual stiffness model to propose a cumulative damage

model [99]. In this model the damage function is defined as:

$$D = \left[\frac{H \cdot (1 - \bar{S})^a}{1 - \bar{S}^a} \right] \cdot \frac{n}{N} \quad (2.4)$$

where $\bar{S} = S/R(0)$ is the normalized applied stress range ($R(0)$ is the ultimate strength and S is the applied stress range) and a and H are parameters. When $D = 0$ no cycles have been applied and when $D = 1$ failure has occurred. This model degenerates into the Miner damage model when a becomes unity, i.e. when the stiffness degrades linearly until failure.

This model has been extended to predict the remaining life of specimens subject to variable amplitude loading. Whitworth, H.A. used the variable amplitude approach to convert a number of cycles at a particular stress to a number of cycles at a reference stress. These stress values are summed and when the values equal one, failure occurs.

Initially, researchers tried to apply the Palmgren-Miner (aka: Miner) damage model to composite materials as a cumulative damage technique however, this approach was not successful. The main reasons the Palmgren-Miner rule is not adaptable to fiber reinforced composites are the diversification of the fatigue damage, the non-uniformity of the damage development and the non-elastic behavior of composites during cyclic loading. At present, a cumulative damage model to accurately predict the development of each damage type has not been developed [108].

The aforementioned models take factors such as stress, strain, stiffness and number of cycles and develop abstract material properties to develop a formulation. Other researchers have investigated other properties as an indication of fatigue. Dharan, C.K.H. et al [16] has proposed to use the hysteresis per loading cycle as a more sensitive measure of damage in composites subjected to cyclic loading. Hysteresis that results from the phase lag between stress and strain, has been employed to provide a qualitative assessment of damage in composites. Various geometric features of the hysteresis loop have been used empirically as damage parameters. Van Paepegem, W. et al [93] proposed the degradation of the Poisson ratio as a damage parameter. The evolution of the Poisson ratio and longitudinal strain is monitored over time. Experimental results have shown that this is a reliable indicator of degradation however, this is not easily applied in practice, as it is difficult to differentiate between the Poisson effect and transverse loading.

Chapter 3

Summary of Contributions

The contributions of this dissertation are contained in the four journal manuscripts included in Appendix A through D. A summary of the main contributions and their relevance to the overall objective is presented below in a logical progression of the life of a composite structure from manufacture to service to failure. The contributions are organized according to their relevant areas rather than in the manuscript they were presented in order to give a broad picture.

3.1 Process Monitoring

This section summarizes the contributions made in the area of process monitoring and effectively summarizes the work and outcome of the manuscripts presented in Appendices A and B. The objectives of this section are to enhance the processing stage by employing a combination of embedded fiber Bragg grating sensors (FBG) and etched fiber sensors (EFS) multiplexed on a single optical fiber. The embedded fiber optic sensors will detect the presence of resin during the injection stage of the resin transfer molding process and subsequently monitor the degree of cure. To do this a number of tasks were carried out before any process monitoring experiments could be performed. The primary tasks are listed below:

- Design and build an experimental RTM apparatus with the ability to visually characterize the flow of resin during injection.
- Develop a suitable technique for embedding optical fiber into structures produced in the aforementioned RTM apparatus.

- Develop an etched fiber sensor that is robust enough to be embedded in the RTM process and multiplexed with fiber Bragg gratings.
- Employ multiplexed EFS and FBG sensors for flow detection in both quasi-2D and 3D RTM'd structures.
- Employ these sensors for cure monitoring of structures produced in the RTM apparatus

3.1.1 Experimental RTM Apparatus

To produce RTM'd composite structures with embedded fiber optics, a sophisticated laboratory-scale apparatus was designed and built. The apparatus has the flexibility of accommodating different mold designs and thicknesses, with the feature of a glass view-port to allow for visual monitoring of resin flow during the injection process. It has been tested by producing composite parts with different geometries such as flat panels, hollow and foam cored square and semicircular tubes made from various types of reinforcements.

The general layout of the experimental apparatus is shown in Figure 3.1. The apparatus can be separated into seven separate components: the injection system, injection valve, mold, manipulating/clamping fixture, catch-pot, vacuum pump and temperature controller. It can be described as a clamshell system with the mold mounted on it. For a mold to be used with this apparatus it must have an area within $533mm \times 850mm$. Any thickness is possible with minor modifications to the clamping system.

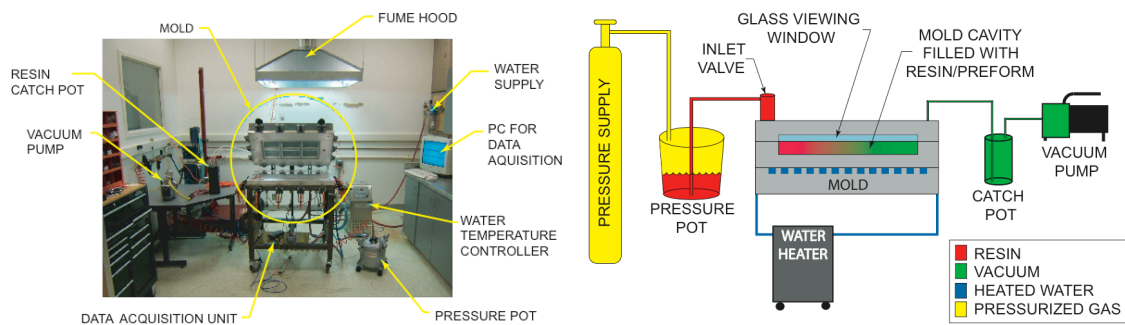


Figure 3.1: Layout and schematic of RTM apparatus

3.1.2 Fiber Optic Ingress/Egress

Fiber optic ingress/egress is one of the most important issues for the application of embedded fiber optic sensors in real composite components [30]. It has been addressed by various researchers [91, 45, 30] however, little information on ingress/egress with RTM is available in the literature. The closed nature of the RTM process as well as the extremely fragile nature of optical fiber makes the ingress/egress of FBG sensors into the mold a challenge. Sealing issues also arise due to the extremely small diameter of the optical fiber.

When optical fiber is embedded with the in-plane method, the ingress/egress point of the optical fiber is located at the edge of the composite. This eliminates the possibility of trimming the outer edges of the composite to size, a very common practice in the industry. To remove a composite part from a mold it must be removed normal to the mold, therefore the embedded fibers must enter and exit through the mold so that upon removal, the fibers are not severed. A novel through thickness ingress/egress method has been developed, which can overcome the limitations of the in-plane method and be applied to closed mold processes such as RTM.

A method to achieve a through thickness ingress/egress that is suitable to pressurized injection molding such as RTM has been developed. Two major obstacles were overcome when developing this technique: sealing the optical fiber and protecting the fiber as it entered the mold.

Optical fiber is quite delicate and must maintain a minimum bend radius before it fractures. When a through thickness fiber ingress technique is used, the fiber sees an abrupt 90° bend as it travels through the mold and into the thin composite part as shown in Figure 3.2a. This is inherent to any through thickness ingress/egress technique.

To protect the fiber with minimal disturbance to the composite material a thin hypodermic tube is placed around the fiber. This protects the fiber through the radius of the bend as well as reinforces it at the ingress/egress point once the part is removed from the mold. As one would imagine it is difficult to seal around something as small as an optical fiber having an outer diameter of $250\mu m$ without permanently caulking or bonding the fiber into the mold. A tapered silicone stopper was used to seal around the hypodermic tube as shown in Figure 3.2b. A custom fitting is used to keep the stopper and fiber in place.

The novelty of this technique lies in the use of the tapered silicon stopper and

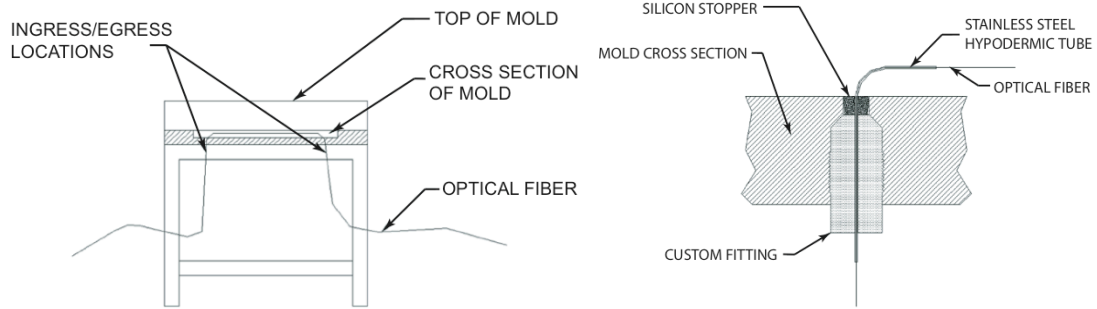


Figure 3.2: a) Through thickness ingress/egress arrangement (left) and b) schematic of fiber sealing (right)

custom fitting. One technique briefly reported by Kosaka, T. et al [48] involves the use of a plastic plug that seals the fiber into the mold and remains bonded to the surface of the composite once it is demolded. The detraction of this technique is that the plastic can become debonded from the composite while in service thereby severing the fiber and rendering the system useless. Also, the fiber must be sealed to the plastic, likely with a sealant that requires time to cure and cannot be removed or adjusted if required. The technique developed and described here overcomes these detractions by using a tapered silicon stopper that applies radial pressure to the hypodermic tube as it is fit into the cavity in the mold, thereby sealing it instantly without any sealant. This allows the fiber to be adjusted at any point prior to injection. Since the stopper is silicon, it is easily removed after molding. This technique can be applied to a mold of any thickness over 10mm by simply adjusting the length of the fitting. This modularity comes in useful considering the wide variation of RTM molds. The fitting also allows the injection pressure to be quite high since it is threaded into the mold, making this technique applicable to higher-pressure injection techniques such as SRIM and thermoplastic injections.

3.1.3 Development of Etched Fiber Sensor

A novel variation of the basic etched fiber sensor is used in this study. This variation involves looping the fiber to create a bend in the etched portion of the fiber. This is done to allow more light to escape from the sensor while still leaving some of the cladding to physically protect it. This variation is a more robust version of the sensor that is easier to handle and implement. Another benefit of looping the fiber is that the sensitivity can be tuned by adjusting the radius of the loop. As the radius of

the loop increases the amount of transmitted light increases. This option is desirable when multiple sensors are used on a single strand of fiber and minimum light loss is desired so that all sensors can make readings. Figure 3.3a shows the sensor with a Canadian quarter for reference ($\varnothing = 23.81mm$); note the etched section in the upper right portion of the loop.

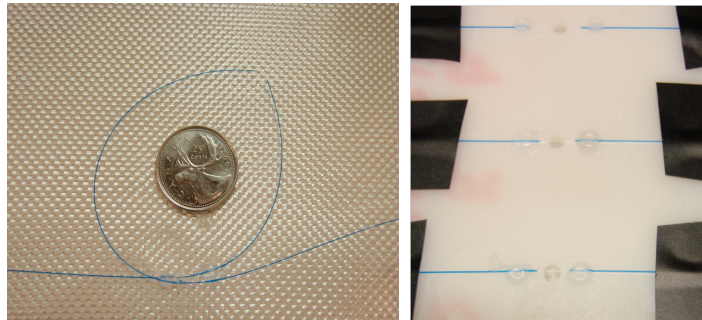


Figure 3.3: a) Looped etched fiber sensor (left) and b) etching jig (right)

The sensors are made by exposing the cladding to a 48% room temperature hydrofluoric (HF) acid solution for a specified amount of time. Since the fibers are to be embedded into an epoxy matrix composite material, polyimide coated fibers are used because they don't react with epoxy. A small section of polyimide coating (the length of the desired etching) is removed from the fiber, usually 3-5mm long. The fiber is placed in a Teflon jig and held in place by melted wax. The Teflon jig has a 3mm diameter spot face that is roughly 5mm deep with a 1mm wide, 1mm deep groove that runs along the surface and over the spot face. Teflon is used for the jig because it does not react with HF. The fiber is placed in the groove and the section with the coating removed is aligned over the spot face. Wax is melted and dripped over the fiber to hold it in place in the jig. Once secured in the jig a few drops of HF are placed in the spot face ensuring that the HF is fully surrounding the fiber. The HF is kept in contact with the fiber until the desired amount of cladding is removed. Once etched, the wax is melted and the sensor may be easily removed from the jig. Figure 3.3b shows the fibers positioned in the jig. At this point the sensor is extremely delicate and easily broken.

3.1.4 Flow Monitoring

Flow monitoring experiments were performed during the resin transfer molding process on two different specimens: a quasi-2D panel and 3D semicircular tube. The

general procedure was similar for both specimens and involved embedding the optical fiber in the mold, closing it and injecting the resin. The optical fiber was connected to a photo-detector and measurements were logged throughout the injection process.

The first experiment was performed on a quasi-2D panel. An optical fiber containing three EFS sensors (EFS#1,2,3) and two FBG sensors (FBG#1,2) was embedded into the mold on the upper ply of the laminate; the mold was closed and the resin was injected. Etched fiber sensor readings were recorded with a photo-detector and data logger while the FBGs were manually observed with an optical spectrum analyzer (OSA). A simple circuit was used to interrogate the sensors as shown in Figure 3.4a. A broad band light source (BBS) was connected to one end of the optical fiber, the fiber ran through the mold, a 50:50 coupler was connected to the other end of the fiber with one branch of the coupler going to the photo-diode and the other to the OSA.

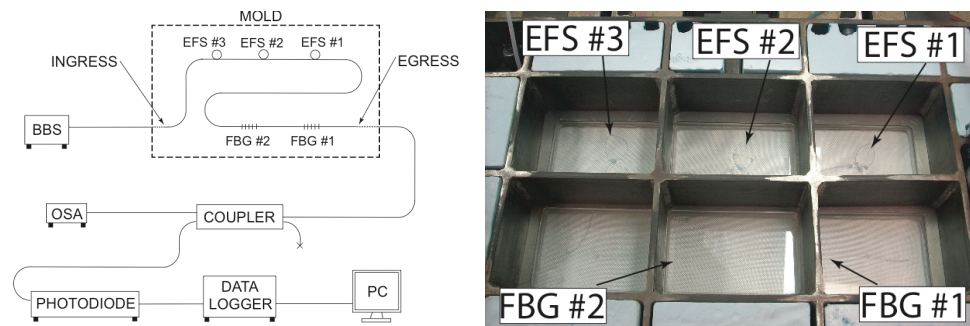


Figure 3.4: a) Interrogation system (left) and b) sensors in RTM prior to injection (right)

Figure 3.4a shows the sensors through the glass viewing window prior to injection, while Figure 3.4b shows the locations of the sensors in the mold. Figure 3.5a shows the resin approaching EFS#1 while Figure 3.5b shows the resin just after the sensor is saturated and the transmitted light intensity is reduced. This occurs roughly 2.4 minutes into the injection. Figure 3.5c shows the whole mold midway through the injection.

Figure 3.6 shows a plot of the photo-diode voltage output vs. injection time. It can clearly be seen that as the resin reaches the first sensor at roughly 2.4 minutes there is a sharp and sustained drop in the transmitted light. Another drop occurs at roughly 7.7 minutes when the resin reaches the second sensor and again at 12.2 minutes when the resin reaches the third sensor. Once the mold was saturated and the injection complete, the light source was turned off to ensure that the readings could



Figure 3.5: CW from top left: a) resin approaching sensor, b) resin just after contacting sensor, c) mold midway through injection

be differentiated from a change in minimal transmitted light and no transmitted light. When the light source was off, the photo-diode output was zero. The light source was turned back on and the transmitted light intensity was the same as before it was turned off, therefore indicating that light was indeed being transmitted. During this time the FBG sensors were manually observed with the OSA to ensure that they were still functional. Due to the arrangement of the sensors on the fiber (FBG before EFS) no change in power was noticed when resin contacted the EFS sensors therefore demonstrating that the EFS do not effect the FBG sensors as long as they are situated after the FBGs on the fiber. The FBG output is not included here however this technique has been thoroughly researched by others such as Novo, C. et al [68] and Eum, S. et al [21, 22].

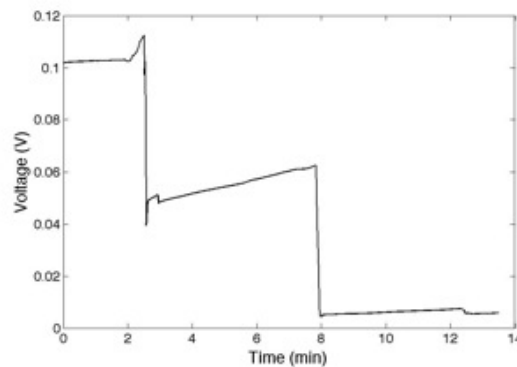


Figure 3.6: Photo-diode output vs. injection time for panel

To demonstrate the versatility and applicability of these sensors to more realistic

structures, an optical fiber containing two EFS sensors was embedded in a hollow tube with a 3D semicircle cross section using the aforementioned RTM apparatus. The sensors were embedded between the fourth and fifth layers on the curved surface of the semicircle. The flat side of the semicircle is visible through the viewing window however the curved surface is not. Due to the relatively small radius of the tube and uniform resin flow it can be assumed with a high level of confidence that the resin is in contact with the sensors and their output can be verified. This is a more realistic experiment for these sensors since the majority of industrial molds are not translucent.



Figure 3.7: Semicircular tube with embedded fiber optic sensors

The sensors were interrogated in a manner similar to that shown in Figure 3.4. Figure 3.7 shows the specimen with the embedded sensors visible. Figure 3.8 shows the resin arrival at the first and second EFS at roughly 2.9 and 4.0 minutes respectively.

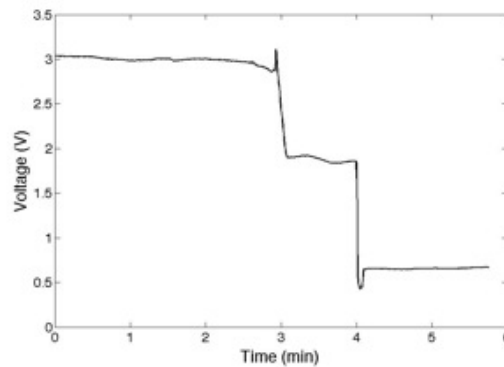


Figure 3.8: Plot of photo-diode output vs. injection time for tube

3.1.5 Cure Monitoring

As described in more detail in Appendix 2, several experiments for cure monitoring of RTM'd composite plates were performed using both FBG and etched fiber sensors. A number of experiments were conducted in the aforementioned RTM apparatus: three with FBG sensors and one with EFS sensors. Each used a laminate composed of nine layers of biaxial glass fiber reinforcement and epoxy resin. The Bragg wavelength shift of the FBG sensor was monitored by a Micron Optics interrogator, model *sm230* and the transmitted light intensity of the EFS was monitored with a photo-detector.

Experiments with the FBG sensors were conducted first. FBGs were positioned between the fourth and fifth plies for the first two experiments and between the seventh and eighth plies for the third experiment. The first two experiments utilized a single FBG while the third utilized three multiplexed on a single fiber. Figure 3.9 shows the Bragg wavelength vs. time for the embedded FBGs during each experiment.

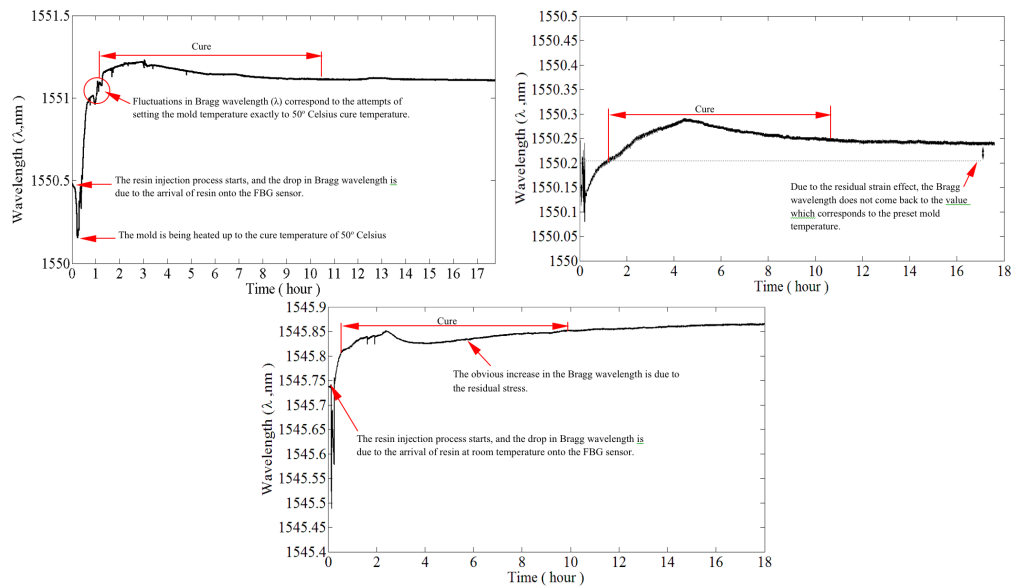


Figure 3.9: CW from top left: Bragg wavelength vs. time during injection and cure of RTM process: a) first, b) second and c) third experiments)

In the first experiment, room temperature resin was injected at roughly 30°C. The first sudden drop in Bragg wavelength in Figure 3.9a is due to the arrival of room temperature resin at the FBG sensor. Subsequently, the mold is heated to cure temperature of 50°C, resulting in an increase of the Bragg wavelength. The fluctuations in Figure 3.9a correspond to a region where the temperature of the mold was set to the cure temperature. Since the cure process is exothermic, the released

heat further increases the shift in Bragg wavelength. As the energy release rate of the exothermic process diminishes, the water cooling system in the RTM mold attempts to bring the temperature to the preset cure temperature. This is observed as a decrease in the Bragg wavelength. Given the presence of the residual stress build-up (due to various effects such as thermal gradients, shrinkage, and differentials in thermal expansion coefficients) in the composite, the Bragg wavelength does not return to its original value. This case is much more obvious in Figure 3.9c because the FBG sensor was positioned on the seventh ply (off-neutral axis). The closer the sensor is to the neutral axis the less strain effect it experiences. As the polymerization reaction nears completion, the shift in Bragg wavelength levels off. The region marked with two vertical lines corresponds to the curing of the epoxy system. In the second and third experiments, the resin was injected into a mold heated to 50°C. A drop in the wavelength was observed upon arrival of the resin to the FBG sensor. As the resin gradually reaches the cure temperature the center wavelength of the FBG sensors increases. The horizontal line in Figure 3.9b indicates the preset mold temperature. Regardless of experimental conditions the tendency of wavelength versus processing time is identical, thereby implying the effectiveness of FBG sensors for cure monitoring for RTM composites.

Experiments were also conducted to investigate the effectiveness of etched sensors for cure monitoring in an operational RTM processing system. Three etched sensors multiplexed on a length of bare optical fiber were embedded between the fifth and sixth plies of the laminate in the RTM mold. The sensors were monitored during the resin injection process and throughout the curing process. The first etched sensor was located near the mold inlet, the second in the middle of the mold and the last was positioned towards the outlet port. In the same experiment, an FBG sensor was placed between the same fiber layers in the middle of the mold.

The EFS sensors were recorded throughout the injection and cure of the resin. Figure 3.10 shows a plot of transmitted light intensity vs. time during cure. It can be seen that there is a steady drop from roughly 7 to 11 hours when the resin completely cures. After eleven hours the output remains relatively steady indicating that the resin has reached full cure. These results correspond with those from the FBG sensor.

To validate the cure monitoring abilities of the sensors investigated, polymer extraction experiments were performed to determine the degree of cure as a function of process time. Several samples of the epoxy resin system were prepared and cast

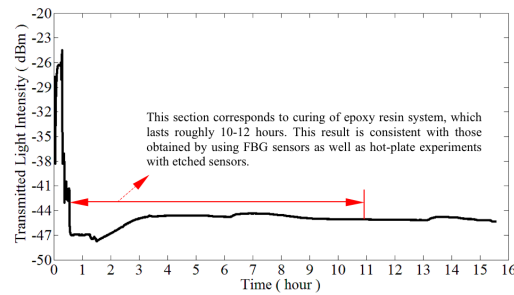


Figure 3.10: Etched fiber sensor data recorded throughout the RTM process

in a Teflon mold. The samples were cured at 50°C for various durations between 2 and 14 hours. The sample was removed from the mold, its mass was measured and placed in a solution of tetrahydrofuran solvent. The solvent removes the uncured epoxy resin over a period of 24 hours leaving the fully cured part behind. After removing the remaining sample from the solution it was dried in an oven and the final mass measured to determine the percentage of cure. The results of the extraction experiments are shown in Figure 3.11. It can be concluded that this specific epoxy resin system completes its cure period under these conditions in 12-14 hours. This result is consistent with the data obtained with the optical sensors.

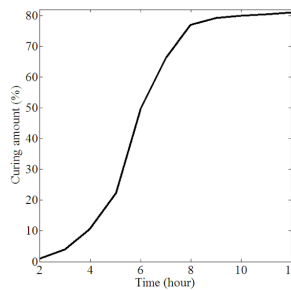


Figure 3.11: Degree of cure as a function of time

3.2 Structural Health Monitoring

Once a composite structure goes through the processing phase described above, it is put into service. During this time damage may occur that the operator must have knowledge of in order to safely operate the structure. The primary objective of this section is to develop an integral structural health monitoring system to detect the presence and location of damage in a structure using a network of piezoelectric

transducers based on tomography. Advancements and contributions are made to the current state of the art of these systems by introducing a novel network configuration that can be expanded to cover larger areas and a detection algorithm that incorporates trends in data that indicate the presence of damage.

3.2.1 Hex Network

The technique developed in this research aims to provide a practical, modular network that is reasonably sparse and can be expanded to cover a large area. Generally, tomography requires a dense network of transducers that cannot be easily expanded to cover a larger inspection area. The proposed technique makes use of a reasonably sparse hexagonal network, which is modular in the sense that it uses a unit cell that can be repeated to expand the network to cover a large inspection area. The unit cell consists of 12 transducers arranged in a hexagonal pattern as in Figure 3.12a. The network can be expanded by simply increasing the number of unit cells as shown in Figure 3.12b. A further benefit is that two unit cells can share three transducers which means that another unit cell only requires nine new transducers.

Lead zirconate titanate (PZT) transducers were selected for this application because they can act as both an actuator and a sensor. Inspection begins by actuating one transducer to send Lamb waves through the material and recording the signals with the remaining transducers. This is then repeated 11 times such that each transducer acts as an actuator once. Since there is one actuator and 11 sensors, there are 11 actuator-sensor pairs per transducer with direct paths between them as shown in Figure 3.12a.

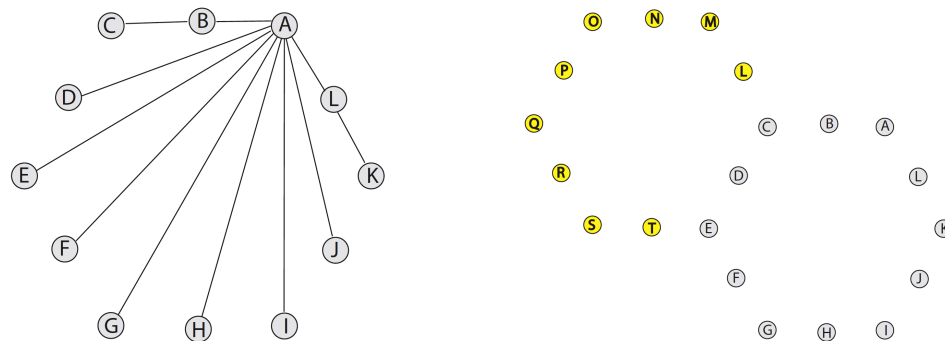


Figure 3.12: a) Hexagonal network showing actuator-sensor paths from transducer A (left) and b) expansion of a single unit cell (right)

3.2.2 Damage Location Algorithm

Once data is collected in undamaged and various damaged states, a technique must be implemented to locate the damage. Various techniques have been developed; each relies on a difference between the damaged and undamaged state. Such techniques include: delay-and-sum beam-forming [95], the time-difference-of-arrival method [58], the energy arrival method [59] and the filtered back-projection method [34].

The algorithm selected for this research was the reconstruction algorithm for probabilistic inspection of damage (RAPID) [26]. It was developed for networks based on 8-16 transducers, has inherently good signal-to-mean-noise ratios [57], can accept various input parameters and produce reasonably accurate results [34].

Changes in the transmitted Lamb wave signal are related to a change in the material properties between two sensors. The probability of defect presence at a certain point can be reconstructed from the severity of the signal change and its relative position to the actuator/sensor pair [26]. The RAPID algorithm is based on two assumptions: i) all effects from every possible actuator/sensor pair can be expressed as a linear summation across the entire inspection region, ii) information from a specific actuator/sensor pair contribute to the defect distribution estimation of a sub-region in the vicinity of the path between the pair.

Equation (3.1) describes the RAPID algorithm:

$$P(x, y) = \sum_{k=1}^N p_k(x, y) = \sum_{k=1}^N A_k \left(\frac{\beta - R}{\beta - 1} \right) \quad (3.1)$$

where $P(x, y)$ is the probability of the existence of a defect at position (x, y) , the Cartesian coordinate of a point in the inspection area, A_k is the damage metric as described below, β is a scaling factor that defines the sub-region the actuator/sensor pair has an effect on (essentially an ellipse with the actuator and sensor at its foci) and $R(x, y)$ is described in Equation 3.2 as:

$$R(x, y, x_{1k}, y_{1k}, x_{2k}, y_{2k}) = \frac{\sqrt{(x - x_{1k})^2 + (y - y_{1k})^2} + \sqrt{(x - x_{2k})^2 + (y - y_{2k})^2}}{\sqrt{(x_{1k} - x_{2k})^2 + (y_{1k} - y_{2k})^2}} \quad (3.2)$$

where (x_{1k}, y_{1k}) is the Cartesian coordinate of the actuator and (x_{2k}, y_{2k}) is the Cartesian coordinate of the sensor.

A_k is a damage metric that is extracted from the Lamb wave signals. It can be

based on various phenomenon such as a reduction in transmitted power, reduction in magnitude of waves or delay in arrival time. More recently Moustafa, A. et al [61] used the fractal dimension with a modified box-counting algorithm however, the most commonly used metric is the signal difference coefficient (SDC) used by [34, 94, 106] among others. This metric will be used as a baseline to compare results with the proposed algorithm. The signal difference coefficient between two data sets is defined as:

$$SDC = 1 - |\rho_{ab}| \quad (3.3)$$

where:

$$\rho_{ab} = \frac{1}{S} \frac{\sum_{i=1}^S (a_i - \mu_a)(b_i - \mu_b)}{\sqrt{\left\{ \sum_{i=1}^S (a_i - \mu_a)^2 \right\} \left\{ \sum_{i=1}^S (b_i - \mu_b)^2 \right\}}} \quad (3.4)$$

and S is the total number of samples, a_i and b_i are the initial data and damaged data at sample i , respectively and μ_a and μ_b are the arithmetic mean value of the initial data set and damaged data set, respectively.

Most damage detection systems rely solely on detecting damage as it occurs, ie. by comparing the change in the damaged state with the undamaged state. In reality however, damage often begins as a small flaw that slowly increases in size while in service. As the damage grows, information can be collected that can be used to locate the damage before it is large enough to be detected by algorithms without this information. In this work, a novel technique is developed that incorporates information from the damage progression into the RAPID algorithm to increase the effectiveness and enable its use in sparse networks where it may otherwise not be applicable.

To incorporate damage progression information, the magnitude of power from the transmitted Lamb waves is compared with that from the previous state (the previous hole size in the case of this study). If the power is less there is the possibility that either damage is progressing in that path or external noise has caused a decrease in the signal. A history of the progression is recorded and if the power consistently drops for a particular path the probability of damage in that location is multiplied by an amplification factor. This is done in order to differentiate between noise and damage progression. Naturally, the initial damage states will not accurately show a damage progression however, as the trend continues across more damage states the accuracy of the prediction increases and the results become more reliable.

3.2.3 Experimental Investigation

To investigate the potential of the proposed network, experiments were conducted on a composite panel with a single unit cell of 12 transducers arranged in a hexagonal pattern as in Figure 3.12a. Reference data was collected while the material was in pristine condition and again with incrementally greater induced damage in the form of a through hole. The data was processed using the RAPID algorithm in order to determine the location of the damage.

A $420\text{mm} \times 420\text{mm}$ panel, composed of eight plies of 139gsm , unidirectional T700 carbon fiber with West System 105/206 epoxy was laminated in a $[0/90/\pm 45]_S$ orientation to produce a 1.23mm thick quasi-isotropic composite. A jig was machined to locate and bond 12, 1mm thick, 7.56mm diameter PZT transducers to the panel in a 75mm circumradius hexagonal array. The panel and network are shown in Figure 3.13a, while a close up of the network showing the damage location is shown in Figure 3.13b. Each transducer was assigned a letter as indicated in Figures 3.12 and 3.13. The coordinates of the transducers are: A : (247.50, 274.95), B : (210.00, 274.95), C : (172.50, 274.95), D : (153.75, 242.48), E : (135.00, 210.00), F : (153.75, 177.53), G : (172.50, 145.05), H : (210.00, 145.05), I : (247.50, 145.05), J : (266.25, 177.53), K : (285.00, 210.00) and L : (266.25, 242.48) in mm from the lower left corner. Damage was induced at: (228.75, 241.85).

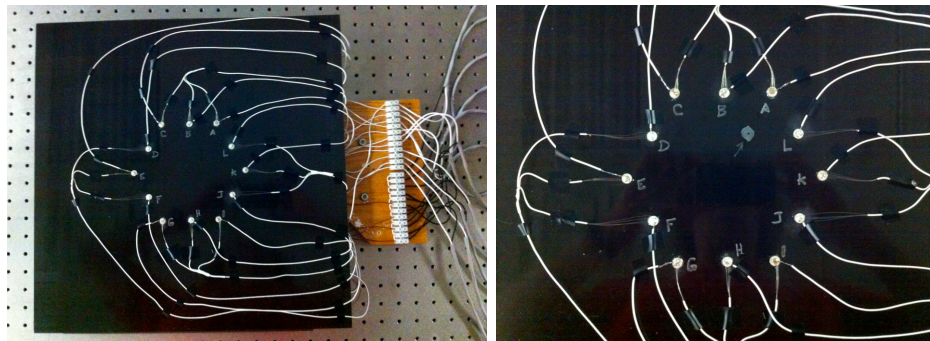


Figure 3.13: a) Composite panel with hex network (left), b) hex network with induced damage (right)

A National Instruments NI PXI-5421 arbitrary waveform generator was used to generate a signal while a NI PXI-5105 digitizer/oscilloscope was used to acquire the signal. Both units were installed in a NI PXI-1033 chassis and controlled with a custom National Instruments LabView program. A model A-303 amplifier from A.A. Labs was used to amplify the generated signal.

An actuation signal consisting of a sine wave with five peaks modulated by a Hann window was employed. An amplitude of $\pm 8V$ was produced by the waveform generator and amplified by a factor of 20 before it was sent to the actuator resulting in a maximum amplitude of $\pm 160V$. The actuation frequency was selected based on a number of criteria. In order to only actuate the S_0 and A_0 modes, the frequency-thickness product was kept below $1.5MHz\text{-}mm$. A frequency scan from $100kHz$ to $400kHz$ was performed to determine the frequency that maintained the greatest transmitted amplitude. It was found that the frequency range of $260\text{-}270kHz$ transmitted the greatest amplitude, therefore $265kHz$ was used for the experiments.

With these properties selected, the waveform generator was programmed to output the actuation signal at $100MHz$. Data was acquired at $60MHz$ for 30×10^3 samples ($500\mu s$). An ASCII text file was written after each run and saved for data processing.

Once the aforementioned experimental apparatus was setup, a number of experiments were performed with various damage conditions. Each experiment consists of actuating one transducer and sensing the other 11, then actuating the adjacent transducer and sensing the remaining 11. This process is repeated until all 12 transducers have actuated the system once. At this point the hole size is increased and the process is repeated.

Initially, the experiment was conducted on the panel in pristine condition before damage was inflicted in the form of a hole drilled through the panel at a location such that it intersected the paths between PZT pairs $A\text{-}G$ and $C\text{-}K$ as shown in Figure 3.13b. The initial diameter of the hole was $1.59mm$, which was increased to $2.38mm$, $3.18mm$, $4.00mm$, $4.76mm$ and finally $6.35mm$.

The main objective of this work is to develop a modular sparse network. To achieve this, an algorithm that uses damage progression information is introduced. With this algorithm, two damage metrics were implemented. The first is based on the SDC in order to investigate the effects of the proposed algorithm on a conventional metric. The second damage metric is based on the transmitted power of the signal from an FFT analysis. For both metrics, a comparison between the results with and without the damage progression algorithm is made to assess the effectiveness. A third case was also considered that neglected information from every second sensor, essentially creating a more sparse network of six transducers. This did not produce any reasonable results therefore implying that a minimum of 12 transducers are required in this situation.

Figure 3.14a presents an example of the received S_0 and A_0 waveforms actuated by

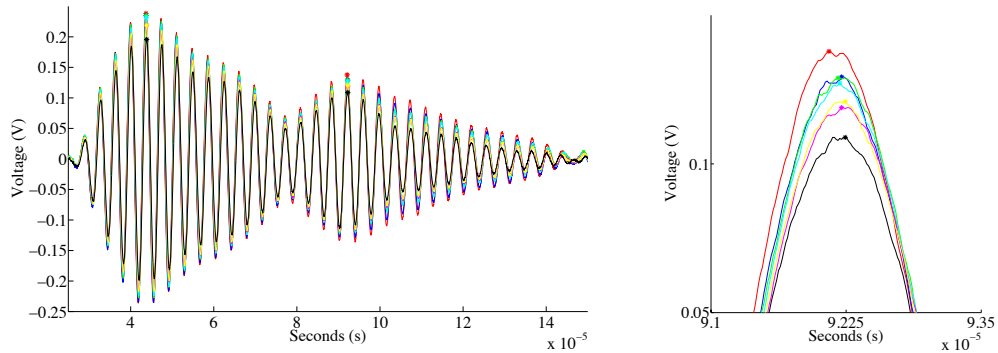


Figure 3.14: a) Received Lamb wave signals at all seven damage states along path *A-G* (left) and b) close up of A_0 wave (right)

transducer *A* and received by transducer *G*. All damage states are plotted together on the same chart with their peaks marked with an asterisk (*). Figure 3.14b shows a close up of the A_0 peak; a consistent decrease in amplitude due to damage is clearly seen. Signals like these from all paths are processed to determine if a decreasing trend exists.

To bench mark the results, the SDC was calculated for each actuator-sensor path and implemented in the RAPID algorithm. A contour plot indicating the probability of damage is presented in Figure 3.15a. The damage location is indicated with the yellow cross and circle. With this information no damage could be detected. This is reasonable according to Michaels, J.E. [57] who reported that the technique was not highly effective on large, sparse arrays. The aforementioned damage progression information was also implemented with the SDC metric. The results are shown in Figure 3.15b. While the algorithm was not able to detect the exact location of the damage it did locate a region close to the general location of the damage therefore showing a marked increase.

In the second implementation, the transmitted power was used as the damage metric. An FFT analysis was performed on data from every actuator-sensor path to extract the magnitude of transmitted power. The RAPID algorithm was implemented and the results are shown in Figure 3.16a. At this point the algorithm has located three possible damage locations compared to zero locations with the SDC metric. The algorithm was implemented with the damage progression information as shown in Figure 3.16b. With this information the algorithm has located a small region of damage roughly the same size within a 12mm radius. While these results are not

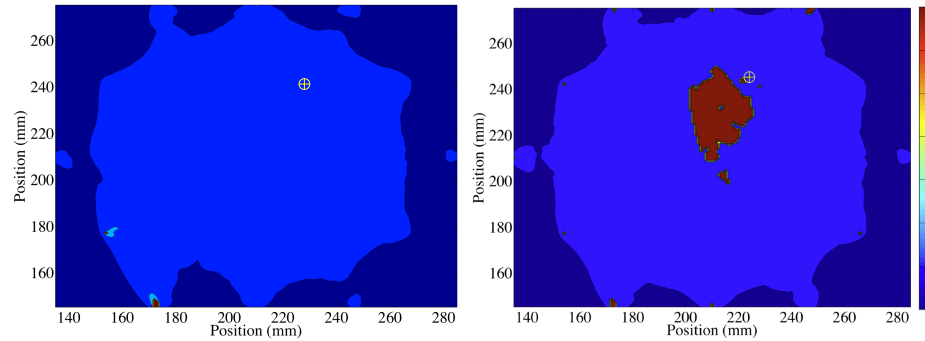


Figure 3.15: a) SDC results with no damage progression factor (left) and b) SDC results with a damage progression factor of 1.10 (right) *Damage location indicated by yellow cross, colorbar indicating value of P from equation (3.1)

highly accurate they do demonstrate that the use of information from the damage progression does increase the probability of damage detection and allows a large, sparse network to be used.

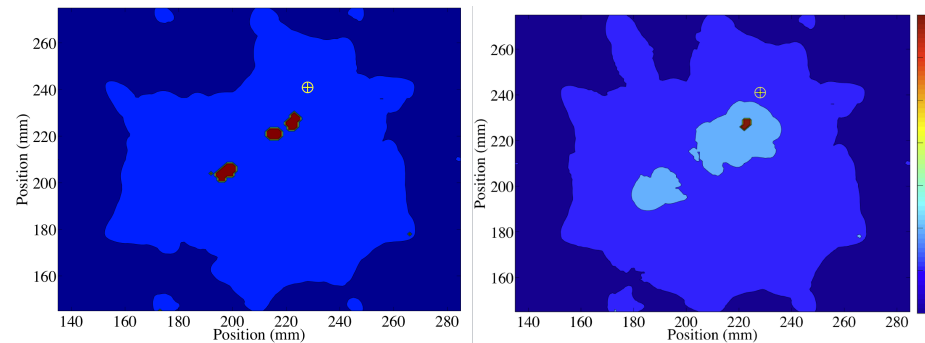


Figure 3.16: a) Power amplitude results with no damage progression factor (left) and b) Power amplitude results with a damage progression factor of 1.10 (right) *Damage location indicated by yellow cross, colorbar indicating value of P from equation (3.1)

3.3 Prediction of Remaining Useful Life

While in service, various levels of loading occur that cause the structural integrity of a composite structure to degrade. Accurate knowledge of these loads and a prediction of the remaining useful life of the structure is highly useful for the operator in terms of safety and efficiency. The primary objective of this section is to develop a technique to predict the remaining useful life of a composite structure under fatigue loading based on information gathered from embedded fiber optic sensors. The technique will use

the previous loading history of the structure to calculate the remaining useful life on a cycle-by-cycle basis to give an estimate of the number of remaining cycles to failure before it must be taken out of service.

3.3.1 Theoretical Development

The relevant data collected from an FBG is in the form of strain and number of cycles. The stiffness of composite materials under fatigue loading gradually decreases over time. This means that the modulus of elasticity is not constant, it is a function of the load history and the stress-strain relationship (Hooke's law) can no longer be applied to extract the magnitude of stress from strain. Therefore, a suitable model cannot use stress as an input, it must use strain.

A promising method of predicting the remaining useful life using only strain was developed by Natarajan, V. et al [65]. The method relies on the strain energy release rate and takes advantage of the fact that it is linear throughout Stage II, 20%-95% as shown in Figure 3.17. It follows a similar approach to the fatigue modulus concept proposed by Hwang, W. et al [37]. An example of the progression of the release of strain energy from a composite during fatigue is shown in Figure 3.17.

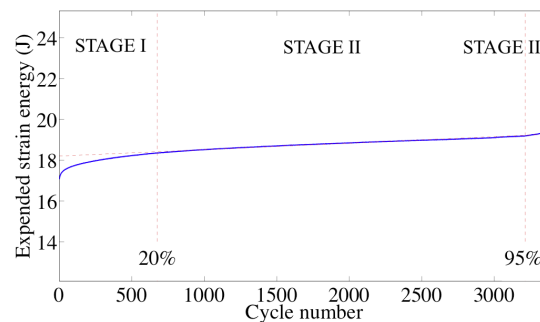


Figure 3.17: Expended strain energy during fatigue loading

To apply this model, the material must be characterized to obtain a relationship between applied strain, ultimate strain and the energy release rate. The method assumes that there is a specific amount of strain energy in the material that is released before it enters Stage III, 95%-100% as shown in Figure 3.17, at which point it is past its useful life. The strain energy can be determined before fatigue loading and used to predict the number of cycles to failure. This method can be employed as a cumulative model if the energy is summed over each cycle. In this research it is proposed to use this method to calculate the released energy on a per-cycle basis using strain data

obtained from embedded FBGs to predict the remaining life. The complete derivation of this method is presented in [65]. An abbreviated version is presented here along with a modification so it can be applied to FBG acquired strain/cycle data.

The variation of expended energy can be described as:

$$\frac{dU_j}{dN_j} = f(\varepsilon_m, \varepsilon_{sr}, U_j, C_t) \quad (3.5)$$

where U_j is the expended energy, N_j is the load cycle, ε_m is the mean strain, ε_{sr} is the strain range, C_t is the composite type. Equation (3.5) can be written in terms of the number of cycles:

$$N_j = \int_{U_0}^{U_j} \frac{dU}{f(\varepsilon_m, \varepsilon_{sr}, (U_j - U_0), C_t)} \quad (3.6)$$

where U_0 is the initial strain energy prior to fatigue initiation and:

$$U_j = U_0 \cdot g(\varepsilon_m, \varepsilon_{sr}, (U_j - U_0), C_t) \quad (3.7)$$

where the function: $g(\varepsilon_m, \varepsilon_{sr}, (U_j - U_0), C_t)$ must be determined experimentally. Differentiating Equation (3.7) with respect to N_j :

$$\frac{1}{U_0} \frac{dU_j}{dN_j} = g' \{ \varepsilon_m, \varepsilon_{sr}, (U_j - U_0), C_t \} \cdot f \{ \varepsilon_m, \varepsilon_{sr}, (U_j - U_0), C_t \} \quad (3.8)$$

and rearranging (3.8):

$$f \{ \varepsilon_m, \varepsilon_{sr}, (U_j - U_0), C_t \} = \frac{1}{U_0} \left(\frac{dU_j}{dN_j} \right) \left(\frac{1}{g' \{ \varepsilon_m, \varepsilon_{sr}, (U_j - U_0), C_t \}} \right) \quad (3.9)$$

The right hand side of Equation (3.9) must be evaluated for ε_m , ε_{sr} keeping the other parameters constant.

The energy release rate: dU_j/dN_j (the rate of energy expended per load cycle) is linear throughout Stage II, therefore the energy release rate for the material at various strain levels can be determined experimentally. The function: $f(\varepsilon_m, \varepsilon_{sr}, U_j, C_t)$ can then be determined by plotting the variation of the energy release rates with maximum induced strain.

The data obtained during fatigue loading should be load and deflection. This data is then used to calculate the strain energy, U_n at any cycle: $U_n = \frac{P_n \delta_n}{2}$, where P_n is

the load at n cycle and δ_n is the deflection a n cycle.

The amount of energy released at 90% of the life cycle (when the material enters Stage III) compared to the initial amount of energy changes based on the ratio: $r = U_f/U_0$. Failure is assumed to occur at this point as the material is no longer intact and dangerously close to catastrophic failure, therefore: $N_f = N_{90\%} = 0.9N_{ult}$.

The slope of Stage II is the expended energy per cycle or the energy release rate: dU/dN . This can be obtained for each specimen by performing a regression analysis of the expended energy data in Stage II. The energy release rate is found to be constant and is characteristic of the constitutive material under similar loading conditions and increases with an increase in induced strain.

Experimental data of the variation in energy release rates with normalized maximum induced strain is fit to a power law:

$$\frac{dU}{dN} = a \left(\frac{\varepsilon_{max}}{\varepsilon_{ult}} \right)^b \quad (3.10)$$

where ε_{max} is the maximum induced strain of the material, ε_{ult} is the ultimate static strain of the material (assumed to remain constant throughout the lifetime) and a and b are fatigue coefficients.

Since the coefficients a and b are invariant for a particular material under a given load type, the fatigue life can be written as:

$$N_f = \frac{U_0 - U_f}{a(\varepsilon_{max}/\varepsilon_{ult})^b} \quad (3.11)$$

where U_0 is the initial strain energy of the material at ε_{max} before fatigue loading, U_f is the sum of the expended strain energy at the end of Stage II and N_f is the fatigue life just before entering Stage III.

Since the specimen is loaded linearly up to the mean strain level before applying fatigue load, the expended energy of the material before fatigue loading is the energy at the mean level. The initial energy of the material at 0 cycles can be written as:

$$U_0 = \frac{P_{mean}^2 l}{2AE} \quad (3.12)$$

where P_{mean} is the mean level of the cyclic load, E is the modulus of elasticity in the loading direction, l is the span (gage length) and A is the cross sectional area. The fatigue life of a material can be obtained experimentally for a particular loading from Equations (3.6) and (3.10), at N_f and written as:

$$N_f = \frac{U_0 - rU_0}{a(\varepsilon_{max}/\varepsilon_{ult})^b} = \frac{(1-r)U_0}{a(\varepsilon_{max}/\varepsilon_{ult})^b} \quad (3.13)$$

Life prediction can be accomplished by summing the energy released under various load amplitudes for the corresponding number of cycles and finding N_f after inserting the total expended energy into Equation (3.13). In the case of an FBG based SHM system, the magnitude of the strain is sensed on every cycle. With this method it is possible to sum the energy on a cycle-by-cycle basis using data obtained from the FBG.

To calculate the energy released during one cycle, Equation (3.10) is integrated with respect to N over one cycle, ie. from N_j to N_{j+1} and ε_{max} is replaced with $\varepsilon_j^{(FBG)}$, the maximum strain value recorded by the FBG during cycle j . This leads to:

$$\Delta U_j = a \left(\frac{\varepsilon_j^{(FBG)}}{\varepsilon_{ult}} \right)^b \quad (3.14)$$

when $(N_{j+1} - N_j) = 1$.

The energy released during each cycle can then be summed during the life of the composite to get the total expended energy up to that cycle: $U_{expended} = \sum_{j=1}^n \Delta U_j$. The remaining life can be estimated: $U_{remaining} = (1-r)U_0 - U_{expended}$, where $U_{remaining}$ is the remaining energy left in the material before failure. Equation (3.11) can be modified to convert the remaining energy into the number of remaining cycles:

$$N_{n-f} = \frac{U_{remaining}}{a(\varepsilon_{expected}/\varepsilon_{ult})^b} \quad (3.15)$$

where N_{n-f} is the remaining life at cycle n , $\varepsilon_{expected}$ is the expected strain level for the remainder of the life. For example, $\varepsilon_{expected}$ could be the average maximum strain from the previous portion of life or if the component was expected to be under harsher loading, $\varepsilon_{expected}$ would be greater than the average maximum strain. With Equation (3.15) various fatigue cycle scenarios could be predicted for various loading cycles by modifying the value of $\varepsilon_{expected}$. The addition of Equations (3.14) and (3.15) to the fatigue life prediction technique developed by Natarajan, V. et al [65] allow for a stepwise addition of expended energy. This is a novel approach to remaining useful life prediction that allows a prediction to be made at each cycle.

3.3.2 Experimental Verification

Experimental validation is required to explore the potential of this technique. This involves producing fatigue specimens with and without embedded FBG sensors, testing them to characterize the material, then testing and applying the failure model to specimens that contain embedded FBGs.

The laminate selected for this research is $[0/90]_{6S}$ E-glass fiber with epoxy resin. The fiber used is Metyx LT300 E10A 0/90 biaxial E-glass stitched fabric with $161gsm$ in the 0° orientation and $142gsm$ in the 90° orientation, summing to $313gsm$ total. The selected resin is Araldite LY 564 epoxy resin with XB 3403 hardener produced by Huntsman Corporation. The panels undergo an initial cure at $65^\circ C$ for 24 hours with a post cure at $80^\circ C$ for 24 hours. Three panels were produced for this study and processed into specimens. Specimens were named with the convention #-###; with the first number indicating the panel they were cut from and second indicating the order in which they were cut. Panel numbering starts at #2 as panel #1 was used for preliminary investigation. Each panel produces ~ 30 specimens.

A tabbing material composed of $1.5mm$ thick, plain weave E-glass non-crimp fabric/epoxy with a $\sim 20^\circ$ angle on one edge is bonded with West System 105 epoxy and 205 hardener thickened with milled glass fiber with a bond-line thickness of $0.7mm$. The panels are cut on a water-cooled diamond blade saw and the edges polished up to 400 grit sandpaper. The final dimensions of the specimens are $280mm$ x $15mm$ x $3.5mm$ with a $160mm$ gage length. The length of the specimen is aligned with the 0° fiber orientation.

A special fixture is required to grip the specimen such that the fiber optic ingress location is not under load. The fixture consists of three steel plates, a bar and a pin. Two plates are clamped across either side of the specimen with bolts. One plate has a slot that allows the fiber to egress from the composite. The plates are screwed into the third plate that has a cylindrical pin that interfaces with the machine grips. A stiffening bar is located across the slot to reduce deflection when the bolts are tightened.

All tests were performed on an MTS 322 test frame with MTS 647 hydraulic wedge grips using an MTS FlexTest GT digital controller with MTS Station Manager software. Load and displacement data was collected with a built in load cell, model: MTS 661.20F-03 and linear variable differential transformer (LVDT), respectively. Strain was collected with an axial extensometer, model: MTS 634.25F-24. All FBG

data was collected with a Micron Optics SM230 interrogator using Micron Optics Enlight software. Temperature data was collected with a K-type thermocouple using a National Instruments NI SCXI-1314 DAQ card in a NI SCXI-1000 chassis with LabVIEW software. The fiber Bragg gratings used in the experiments were 10mm long with a center wavelength of either 1555 or 1565nm supplied by FiberLogix. All data is acquired at a sampling rate of 100Hz.

First, the material must be characterized by determining the relationship between the stress release rate and strain, i.e. determine the fatigue coefficients (a and b from Equation (3.10)). To do this, static testing must be performed to determine the ultimate tensile strain, ε_{ult} . After ε_{ult} is determined, a number of samples at various strain levels are fatigue tested. From this data the strain energy release rate as a function of strain may be determined and plotted to obtain a and b . Once the values of a and b known, the specimens with embedded FBGs can be tested. For this study, a number of fatigue tests at each of the following strain amplitudes ($\varepsilon_{max}/\varepsilon_{ult}$): 0.8, 0.75, 0.7, 0.6, 0.5 and 0.4 were performed including two fatigue tests with specimens containing embedded FBGs. A static test was also performed to determine the ultimate strain of the embedded FBG.

Autogeneous heating becomes a concern during fatigue testing of glass fiber reinforced composites as the heat is not readily conducted to the environment as it is with metallic materials. The fatigue properties of composites are especially sensitive to heat. Generally, a fatigue loading frequency of 1-4Hz for glass fiber has been used with no adverse effect, therefore tests are performed at a frequency of 4Hz.

All fatigue tests are constant amplitude strain, tension-tension sine wave tests. The maximum and minimum load and displacement is recorded. The minimum stress on the specimens is 27.6MPa while the maximum load is determined as a fraction of the maximum stress of 318.75MPa. The magnitude of the minimum load was selected to be close to that used by Natarajan, V. et al [65]. To determine the displacement amplitude to obtain the desired strain, a simple calibration procedure is performed: the specimen is loaded into the machine and a load that will produce the desired amount of stress is slowly applied and released, then applied and released a second time. When the specimen is unloaded there is a residual displacement sensed by the LVDT. This is due to the wedge grips tightening and the specimen slipping slightly before the full clamping force is realized. This zero offset only occurs during the first loading cycle, after that the displacement returns to zero when the load is returned to zero. To account for this nonlinear phenomenon the zero-offset is subtracted from

the maximum displacement on the second loading cycle. The fatigue tests are then run at this displacement.

Once the fatigue coefficients are determined, the specimens with embedded FBGs can be tested. Prior to fatigue testing their temperature sensitivity must be characterized in order to account for the temperature change due to autogeneous heating. To do this the specimens and a bare FBG are placed in an oven with three thermocouples. The temperature in the oven is ramped up to $30^{\circ}C$, $40^{\circ}C$, $50^{\circ}C$ and $60^{\circ}C$ and allowed to soak at each temperature for one hour before the temperature and wavelength is recorded. A plot of wavelength vs. temperature is constructed for each FBG and linear regression is used to extract an average temperature sensitivity of $0.031nm/^{\circ}C$ for the specimens and $0.010nm/^{\circ}C$ for the bare FBG.

A total of 11 static tests and 33 fatigue tests were performed. The results were processed and a number of test results were rejected due to factors such as their failure mode, outlying results or experimental procedure error. A total of three specimens with embedded FBGs were tested. One specimen was tested statically to determine the ultimate strain of the embedded FBG and two under constant displacement. Prior to fatigue testing, the specimens were calibrated with an extensometer to determine the strain sensitivity of the FBGs. During testing, a thermocouple was fastened to the surface of the specimen to monitor any temperature increase due to autogeneous heating. The FBG embedded specimen tested at a strain level of 0.4 was not tested until failure. The strain energy release rate was still obtained from the test however the number of cycles to failure was not. After the tests were completed and all requisite data was collected it was processed in order to apply the theory to predict the remaining useful life.

Static tests were performed in order to determine the ultimate stress and strain of the material that was later tested under fatigue. The ultimate stress and strain were found to be $318.75MPa$ and $16.31m\varepsilon$, respectively (where $m\varepsilon$ is milli-strain).

Once the static tests were complete, the fatigue tests were performed. Peak strain and load data was converted into expended energy per cycle and plotted to produce an energy curve for each specimen as shown in Figure 3.18 (left). The aforementioned energy release trend is quite apparent in the energy curve plots; an example plot is shown in Figure 3.17.

Linear regression was used to obtain the energy release rate (dU/dN) throughout the linear region. The average energy release rate and ratio of U_f/U_0 for various levels of induced strain are presented in Table 3.1. The ratio U_f/U_0 (energy at failure, U_f

(90% of total cycles) to initial energy U_0) is significant as it is used in the prediction of the remaining cycles in Equation (3.13). The average value of $r = U_f/U_0 = 0.856$ was used for predictions.

$\varepsilon_{max}/\varepsilon_{ult}$:	Energy Release Rate (J/cycle):	$r = U_f/U_0$:
0.4	8.705E-08	0.799
0.5	3.337E-06	0.826
0.6	3.352E-05	0.855
0.7	3.736E-04	0.885
0.75	1.307E-03	0.901
0.8	2.592E-03	0.917

Table 3.1: Fatigue test data

The energy release rate was plotted vs. normalized induced strain, Figure 3.18a. This data was averaged, plotted and fit to a power law curve to obtain the values for fatigue coefficients a and b , of 14.67 and 0.070595, respectively. With a and b determined, the fatigue life could be predicted using Equation (3.13). The experimental and predicted results are plotted as an ε - N curve in Figure 3.18b. The number of experimental and predicted cycles to failure (N_f) and percent difference is shown in Table 3.2.

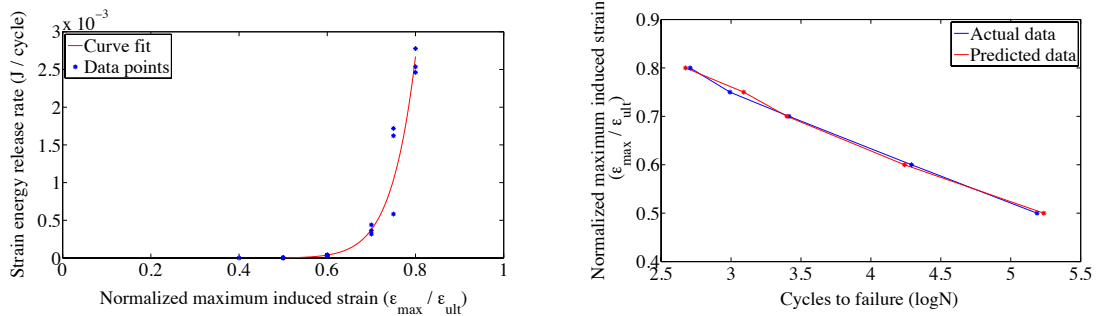


Figure 3.18: a) Variation of energy release rate (left) and b) ε - N plot (right)

One problem that was immediately apparent was that as the FBG was strained, the reflected spectrum broadened, reduced in magnitude and split into multiple peaks making it difficult to accurately track. This is due to the uneven strain field caused by matrix cracking and the fiber reinforcement arrangement as documented by Takeda, N. et al [87, 88, 82], Okabe, Y. et al [69], Yashiro, S. et al [109] and others. The peak splitting resulted in an inaccurate measurement of the strain magnitude, either

greater or less than the actual strain. As the peak split, the tallest peak would move to either side of the Bragg wavelength. The interrogator algorithm would track this peak rather than the center wavelength thus resulting in inaccurate strain values.

$\varepsilon_{max}/\varepsilon_{ult}$:	Experimental N_f :	Predicted N_f :	Difference (%):
0.5	154108	185132	20.13
0.6	19510	17475	-10.43
0.7	2597	2389	-8.00
0.75	1233	982	-20.34
0.8	510	428	-16.17

Table 3.2: Fatigue life prediction results

The reduction in magnitude also presented a problem. One of the settings of the interrogator software is the threshold of the magnitude of the reflected spectrum. The threshold must be set high enough to eliminate noise but not so high that the FBG reflected spectrum is excluded. Under low strain there was not enough of a reduction in magnitude to drop below the threshold, however as the strain increased towards the upper limits the magnitude reduced and in some cases dropped below the threshold causing the interrogator to momentarily lose the signal. This resulted in a number of data points that were recorded as 0. When the peaks were extracted from the full waveform data, missing peaks were given a value that was determined by interpolating between the neighboring peaks. Figure 3.19 shows the acquired signal from Specimen 3-1 for five second intervals of the fatigue test in the beginning a and end b. The blue lines show the acquired data at an acquisition rate of $100Hz$ while the red circles indicate the peaks and troughs of the data that were extracted from the full waveform.

The surface temperature of the specimens that was monitored during the tests was converted into a wavelength value ($\Delta\lambda_B$) using the temperature sensitivity described earlier. The wavelength change due to temperature was subtracted from the FBG data.

The first test performed was a quasi-static tensile test to determine the ultimate strain level of the embedded FBG in Specimen 2-2. This information would provide a range of strain levels to conduct the fatigue tests.

Figure 3.20 shows a plot of strain measured with an extensometer on the left vertical axis and FBG wavelength on the right vertical axis vs. stress. Both strain and wavelength follow a linear increase until roughly $160MPa$ when there is a small

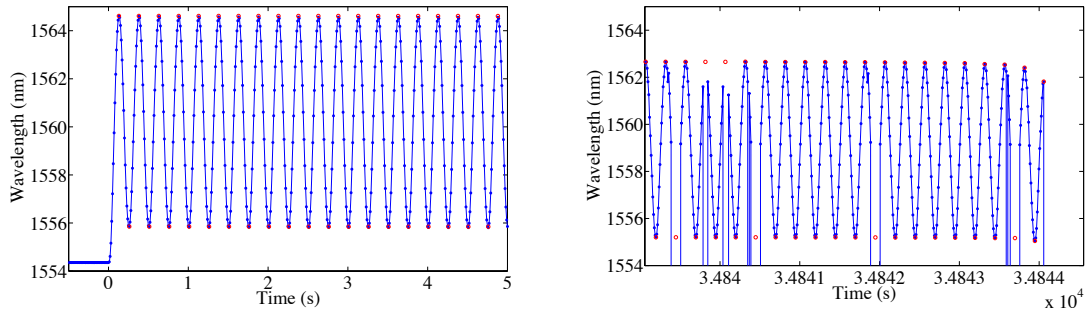


Figure 3.19: a) Wavelength vs. time for five second intervals at the beginning and b) end of the test

jog in the FBG signal. This is likely due to the FBG reflected spectrum splitting and the peak moving to the lower range of the spectrum. After the jog, the increase in the signal remains linear as expected. The strain level measured by the extensometer when the fiber optic broke was $10.323m\varepsilon$ while the FBG read $10.039m\varepsilon$ due to the shift. It is also worth mentioning that a loud 'ping' noise was heard when the fiber optic broke/signal was lost.

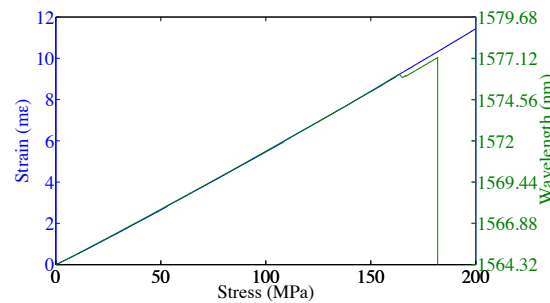


Figure 3.20: Wavelength and strain vs. stress

Before fatigue tests began, a simple strain characterization test was performed to determine the strain sensitivity of each specimen by straining it and monitoring the Bragg wavelength, displacement and strain in the specimen. FBG sensitivities of $1.2596nm/m\varepsilon$ and $1.2691nm/m\varepsilon$ were obtained for Specimen 3-1 and 4-2, respectively. The conversion from LVDT acquired displacement to strain was also obtained.

Specimen 3-1 was tested at a maximum induced strain of $0.5*\varepsilon_{ult}$. Figure 3.21a shows the strain data vs. cycle number throughout the test. The blue line indicates LVDT acquired displacement data and the red line indicates FBG wavelength data. Both data sets are converted to strain for application to the prediction technique.

The data measured with the LVDT shows a steady constant strain throughout the entire test as expected. The FBG data however, initially shows a sharp increase due to autogeneous heating followed by a nonlinear decrease which leads to a linear decrease until roughly 13.5×10^4 cycles when it exhibits a sharp nonlinear decrease until failure. This shows the same trend as the load and is likely due to the break down of the composite resulting in a non-uniform strain field that causes the FBG peak to broaden.

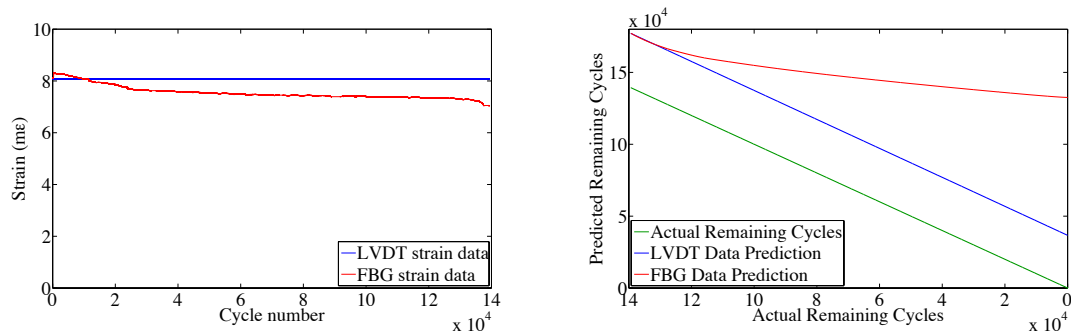


Figure 3.21: a) Results for Specimen 3-1: strain data (left) and b) prediction of remaining cycles (right)

Figure 3.21b shows the prediction results from the data presented on the left along with the actual failure data. The prediction is made at every cycle based on data from the LVDT and FBG in blue and red, respectively. Since the LVDT data is constant, the predicted number of remaining cycles remains linear with a constant offset from the actual data. The error in these results is a function of the accuracy of the prediction method and experimentally determined fatigue coefficients from Equation (3.10). The predicted results are within 27% of the actual results at the beginning of the test. This larger than average difference compared to the average results shown in Table 3.2 can be attributed to the statistical variation in the material properties from specimen to specimen. The predicted results from the FBG data however, are not as accurate due to the reduction in magnitude of the strain signal. Since the prediction formula is based on a power law, a small variation in measured data can result in a large discrepancy between actual and predicted results. For the first 2×10^4 cycles the FBG prediction results are quite close to the LVDT prediction before they drift away to an unreasonable value.

In an attempt to subject the embedded FBG to a lower ε_{max} to obtain a more accurate signal, Specimen 4-2 was tested at a maximum induced strain of $0.4^* \varepsilon_{ult}$. Figure 3.22a shows the strain data vs. cycle number throughout the test. The

blue line indicates LVDT acquired displacement data and the red line indicates FBG wavelength data. Clearly the signal from the FBG is much closer to that measured by the LVDT than for Specimen 3-1. Naturally this results in a more accurate prediction of the remaining cycles as shown in Figure 3.22b.

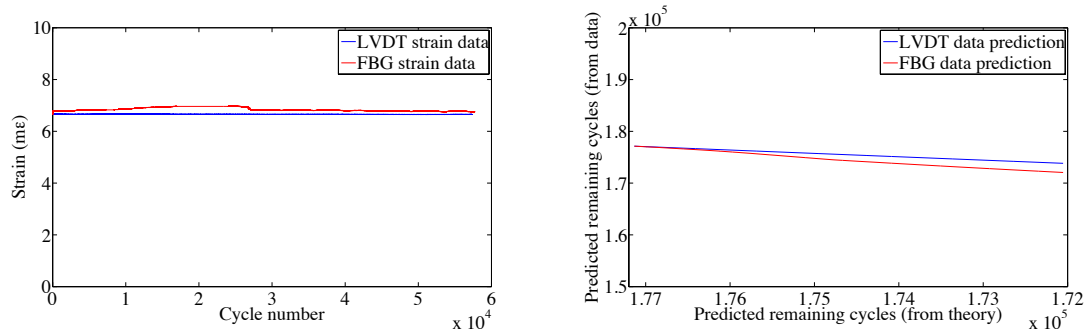


Figure 3.22: a) Results for Specimen 4-2: strain data (left) and b) prediction of remaining cycles (right)

Figure 3.23 shows a plot of the surface temperature of Specimen 3-1 on the left vertical axis and the applied load on the right vertical axis vs. percent of test. They are presented on the same plot in order to compare their similar trends. The temperature data (blue) shows a sharp increase during the first $\sim 5\%$. This is due to the autogeneous heating that occurs. After the initial peak there is a nonlinear decrease until $\sim 18\%$. After that there is some erratic fluctuation from $\sim 18\%$ to 55% that is likely due to external effects such as ambient temperature change. After that, the decrease remains steady and linear until 95% when there is a final change to a greater decrease in temperature until failure. The load follows a very similar pattern aside from the initial sharp increase. From the first cycle to $\sim 15\%$ there is a nonlinear decrease before a constant linear decrease is observed until $\sim 95\%$ when a sharp nonlinear decrease occurs until failure.

Both data sets follow the trend of strain energy outlined in [65]. The temperature change is caused by the work done on the material. When there is a greater load applied more strain energy is put into the material and therefore more autogeneous heating occurs. As the material starts to degrade and requires less load to reach the specified strain, less energy is put into the material and less heating occurs. Naturally there is a lag in the temperature signal due to the poor conductivity of glass fiber/epoxy composite.

This suggests that while susceptible to external environmental effects, monitoring the surface temperature of composites subjected to fatigue may be used to give insight

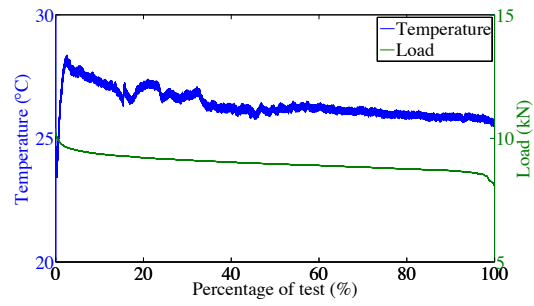


Figure 3.23: Temperature and load vs. percent of test

into the condition of the material.

Chapter 4

Conclusions and Future Work

The overall objective of this work is to research and develop techniques for increasing the manufacturing and operating efficiency and reliability of composite structures by employing integrated sensor/transducer networks. Embedded fiber optic sensors and piezoelectric transducers are used to achieve this objective.

The first sub-objective is to enhance the processing stage. This is done by employing a combination of embedded fiber Bragg grating (FBG) sensors and etched fiber sensors individually and multiplexed on a single optical fiber. The sensors detect the presence of resin during the injection stage of a resin transfer molding process and subsequently monitor the degree of cure. To achieve this objective, an RTM apparatus with glass view-port has been manufactured and successfully tested. A method for embedding fiber optics has also been devised and tested. The apparatus was used to embed an optical fiber with three EFSs and two FBGs into a quasi-2D panel, two EFSs in one semicircular tube and two FBGs in a second tube. The glass window in the mold was used to visually monitor the resin flow while a photo-diode and data logger was used to take readings from the etched sensors. Data was recorded with both FBG and EFS sensors during the curing stage. Acid digestion tests were performed to determine the degree of cure of the neat resin under various cure schedules. Results closely agreed with those from the sensors.

This study successfully demonstrates the potential of multiplexing a number of optical sensors onto a single fiber and embedding them into resin transfer molded composite parts of various shapes and complexities. The EFSs showed a high degree of accuracy at detecting the presence of resin however the readings of various EFSs could not be differentiated without a priori knowledge of the resin flow. Implementing an optical time domain reflectometer (OTDR) would allow the sensors to be differ-

entiated. Both FBGs and EFS have demonstrated the ability to monitor the degree of cure.

Once a composite structure goes through the processing phase, it is put into service. During this time damage may occur, which the operator must have knowledge of in order to safely operate the structure. The second sub-objective is to develop a structural health monitoring system to detect the presence and location of damage in a structure using a network of piezoelectric transducers. Advancements and contributions are made to the current state of the art of these systems through the introduction of an algorithm that makes use of trends from previous damage states and its application it to a modular, sparse network that can be expanded to cover large areas. The network consists of a unit cell of 12 piezoelectric transducers arranged in a hexagonal pattern. The network is easily expanded by adding nine more transducers to the existing 12. The hexagonal arrangement allows for efficient stacking of unit cells that would not be otherwise possible with a circular array.

Damage progression information was implemented in the form of a 10% increase in signal magnitude if the actuator-sensor path showed a consistent decrease in power across each damage state (ie. if the power was consistently less than the previous state). The results presented in Figure 3.15 show that incorporating the damage progression information increases the chance of detection with SDC as a damage metric. When the power of the transmitted wave is used as a damage metric some potential damage locations appear as shown in Figure 3.16a. When the damage progression information is incorporated the accuracy is increased, locating a potential damage site that is within $12mm$ of the actual damage as shown in Figure 3.16b. While the results do not directly pinpoint the damage location they do show that an improvement over the existing RAPID algorithm can be made by incorporating damage progression information with the use of a larger area sparse network on a carbon fiber composite material.

While in service, various levels of loading occur that cause the structural integrity to degrade. Accurate knowledge of these loads and a prediction of the remaining useful life of the structure is highly useful for the operator in terms of safety and efficiency. The third sub-objective is to develop a technique to predict the remaining useful life of a composite structure under fatigue loading based on information gathered from embedded fiber Bragg grating sensors. The technique uses the previous loading history of the structure to calculate the remaining useful life on a cycle-by-cycle basis to give an estimate of the number of remaining cycles to failure. A life prediction

theory developed by Natarajan, V. et al [65] based on the magnitude of strain rather than stress was selected because the FBGs detect strain and the stiffness of the composite changes during cyclic loading making a conversion from strain to stress with Hooke's law not possible. The theory was extended to account for information gathered by the sensors on a cycle by cycle basis and a number of experiments were performed to verify the concept.

After testing a total of 44 specimens, the fatigue coefficients required to apply the strain energy release rate prediction model to a $[0/90]_{6S}$ glass fiber/epoxy laminate were obtained. In order to explore the concept of using FBGs to predict the remaining cycles throughout the fatigue life, three specimens with embedded FBGs were tested. The results of the non-FBG embedded fatigue tests closely agreed with previous work by Natarajan, V. [65] showing the same material degradation pattern.

A quasi-static test was performed to determine the ultimate strain of the FBG and therefore the testing range of the specimens. The result showed that the ε_{max} of the embedded fiber optic is $\sim 10m\varepsilon$. The data also demonstrated the peak splitting phenomenon that results in an inaccurate strain level as shown in Figure 3.20.

During the fatigue test of Specimen 3-1, the recorded data from the FBG sensors did not closely match that of the LVDT displacement data, rather its magnitude declined throughout the test. This is due to the degradation of the composite resulting in an uneven strain field in the region of the FBG causing the reflected spectrum to broaden and eventually split into multiple peaks. The algorithm used by the interrogation equipment records the peak with the largest magnitude, which is not always in the middle of the spectrum and therefore not an accurate measure of the strain. The results of peak splitting is apparent when comparing the FBG data from tests conducted at $\varepsilon_{max}/\varepsilon_{ult} = 0.5$ and 0.4 . When the peak split during the first test, the tallest peak shifted to a lower wavelength and therefore the strain measured is less than the that of the actual strain while the opposite situation occurred with the latter test. Due to the discrepancy in the FBG measured strain value and actual strain value, the predicted remaining life results are not highly accurate. For the fatigue test performed on Specimen 3-1 ($\varepsilon_{max}/\varepsilon_{ult} = 0.5$) the FBG based prediction is close to the theoretical prediction for the first 20×10^3 cycles. The fact that the fatigue life equation is based on a power law results in a small discrepancy in strain producing a large discrepancy in predicted remaining cycles. The fatigue test performed on Specimen 4-2 ($\varepsilon_{max}/\varepsilon_{ult} = 0.4$) produced more accurate FBG strain data. Naturally, the FBG based prediction is much closer to the theoretical prediction for the latter

test. A strain amplitude of $\varepsilon_{max}/\varepsilon_{ult} = 0.5$ was selected for the first test to decrease testing time however, in real life a strain of this magnitude would not be seen as the safety factor of composites is generally above two, therefore a more reliable signal would likely be obtainable in real situations.

The introduction of Equations (3.14) and (3.15) to the fatigue life prediction technique developed by Natarajan [65] are novel, as is their approach to remaining useful life estimation that allows a prediction to be made at each cycle.

The conclusions drawn from these tests suggest that a more accurate and reliable signal from the embedded FBGs is required for accurate results. Three avenues to pursue in order to achieve this are: operate at lower strain level, investigate the use of shorter FBGs (1-3mm in length) and develop a more robust FBG interrogation algorithm. The ε_{ult} of carbon fiber is much lower than that of glass fiber meaning a structure composed of carbon fiber would see less strain and therefore an embedded FBG would not degrade as rapidly. To investigate this, the same study could be repeated with carbon fiber rather than glass fiber composites.

The results outlined in this dissertation show that both the sub-objectives and overall objective stated in Chapter 1 were successfully met. This research is highly multidisciplinary, covering areas such as mechanical design, composite material processing, sensors and transducers (fiber optic and piezoelectric), fatigue theory, material testing and signal processing. A number of new concepts and techniques were introduced. Future work involves further refinement of these techniques and their application to other situations.

Bibliography

- [1] M.A. Fromowitz. Fiber optic polymer cure sensor. *Journal of Lightwave Technology*, 6(10):1591–1594, 1988.
- [2] S.H. Ahn, W.I. Lee, and G.S. Springer. Measurement of the three-dimensional permeability of fiber preforms using embedded fiber optic sensors. *Journal of Composite Materials*, 29(6):714–733, April 1995.
- [3] V. Antonucci, M. Giordano, L. Nicolais, A. Calabro, A. Cusana, A. Cutolo, and S. Inssera. Resin flow monitoring in resin film infusion process. *Journal of Materials Processing Technology*, pages 687–692, 2003.
- [4] J. Bao. Lamb wave generation and detection with piezoelectric wafer active sensors. *PhD Dissertation, Beijing University*, 2003.
- [5] J.R. Bernstein and J.W. Wagner. Fiber optic sensors for use in monitoring flow front in vacuum resin transfer molding processes. *Review of Scientific Instruments*, 68(5):2156–2157, 1997.
- [6] G.S. Bottai, P.J. Pollock, T.A. Behling, and V. Giurgitu. Damage detection in cryogenic composites for space applications using piezoelectric wafer active sensors. *South Carolina University, Columbia department of mechanical engineering*, 2008.
- [7] A.J. Bur, F.W. Wang, and C.L. Thomas. In-line optical monitoring of polymer injection molding. *Polymer Engineering and Science*, 1994.
- [8] K. Chakrabarty, S.S. Iyengar, H.R. Qi, and E.C. Cho. Grid coverage for surveillance and target location in distributed sensor networks. *IEEE Transactions on Computers*, 51(12):1448–1453, 2002.

- [9] J.T. Chambers, B.L. Wardle, and S.S. Kessler. Durability assessment of lamb wave-based structural health monitoring nodes. *AIAA*, 2006.
- [10] P.A. Crosby, G.R. Powell, G.F. Fernando, C.M. France, R.C. Spooncer, and D.N. Waters. In situ cure monitoring of epoxy resins using optical fibre sensors. *Smart Materials and Structures*, 5(4):415–428, 1996.
- [11] A. Cusano, G Breglio, M. Giordano, A. Calabro, A. Cutolo, and L. Nicolais. An optoelectronic sensor for cure monitoring in thermoset-based composites. *Sensors and Actuators A-Physical*, 84(3):270–275, 2000.
- [12] W. Dang and N.H. Sung. In-situ cure monitoring of diamine cured epoxy by fiberoptic fluorimetry using extrinsic reactive fluorophore. *Polymer Engineering and Science*, 34(9):707–715, 1994.
- [13] A. Davis. Study of an opto-ultrasonic technique for cure monitoring. In *Fiber Optic Smart Structures and Skins IV*, pages 264–274. SPIE, 1991.
- [14] J. Degrieck and W. Van Paepegem. Fatigue damage modeling of fibre-reinforced composite materials: Review. *Applied Mechanics Reviews*, 54(4):279, 2001.
- [15] V. Dewynter-Marty, P. Ferdinand, E. Bocherens, R. Carbone, H. Beranger, S. Bourasseau, M. Dupont, and D. Balageas. Embedded fiber Bragg grating sensors for industrial composite cure monitoring. *Journal of Intelligent Material Systems and Structures*, 9(10):785–787, 1998.
- [16] C.K.H. Dharan and T.F. Tan. A hysteresis-based damage parameter for notched composite laminates subjected to cyclic loading. *Journal of materials science*, 42(6):2204–2207, 2007.
- [17] C. Doyle, A. Martin, T. Liu, and M. Wu. In-situ process and condition monitoring of advanced fibre-reinforced composite materials using optical fibre sensors. *Smart Materials and Structures*, 1998.
- [18] J.P. Dunkers, J.L. Lenhart, and S.R. Kueh. Fiber optic flow and cure sensing for liquid composite molding. *Optics and Lasers in Engineering*, 2001.
- [19] J.R. Dunphy. Multifunction, distributed optical fiber sensor for composite cure and response monitoring. In *Fiber Optic Smart Structures and Skins III*, pages 116–118. SPIE, December 1990.

- [20] J.A. Epaarachchi, J. Canning, and M. Stevenson. The Response of Embedded NIR (830 nm) Fiber Bragg Grating Sensors in Glass Fiber Composites under Fatigue Loading. *Journal of Composite Materials*, 44(7):809–819, 2010.
- [21] S. Eum, K. Kageyama, H. Murayama, I. Ohsawa, K. Uzawa, M. Kanai, and H. Igawa. Resin flow monitoring in vacuum-assisted resin transfer molding using optical fiber distributed sensor. In *Proceedings of SPIE*. SPIE, April 2007.
- [22] S. Eum, K. Kageyama, H. Murayama, I. Ohsawa, K. Uzawa, M. Kanai, and H. Igawa. Process/health monitoring of turbine blades with FBG sensors with multiplexing techniques. *Proceedings of SPIE*, 7004, June 2008.
- [23] G.F. Fernando, T. Liu, P. Crosby, C. Doyle, A. Martin, D. Brooks, B. Ralph, and R. Badcock. A multi-purpose optical fibre sensor design for fibre reinforced composite materials. *Measurement Science and Technology*, 8(10):1065–1079, 1997.
- [24] P.A. Fomitchov, Y.K. Kim, and A.K. Kromine. Distributed photoacoustic system for cure monitoring of composites. In *Proceedings of SPIE*, 2001.
- [25] C.L. Frederick and D.C. Worlont. Ultrasonic thickness measurements with Lamb waves. *Journal of Nondestructive Testing*, 20:51–55, January 1962.
- [26] H. Gao. Guided wave tomography on an aircraft wing with leave in place sensors. In *Review of Progress in Quantitative Nondestructive Evaluation*, pages 1788–1794. AIP, 2005.
- [27] V. Giurgiutiu. Embedded Non-destructive Evaluation for Structural Health Monitoring, Damage Detection, and Failure Prevention. *The Shock and Vibration Digest*, 37(2):83–105, March 2005.
- [28] V. Giurgiutiu and J. Bao. Embedded Ultrasonic Structural Radar with Piezoelectric Wafer Active Sensors for the NDE of Thin-Wall Structures. In *ASME 2002 International Mechanical Engineering Congress and Exposition*, pages 31–38. ASME, 2002.
- [29] V. Giurgiutiu, J. Bao, and W. Zhao. Piezoelectric wafer active sensor embedded ultrasonics in beams and plates. *Experimental Mechanics*, 43(4):428–449, 2003.

- [30] A.K. Green and S. Darvish. Practical terminations for optical fibres embedded in composite materials. In *Proceedings of SPIE*, 1996.
- [31] H.Y. Guo, L. Zhang, L.L. Zhang, and J.X. Zhou. Optimal placement of sensors for structural health monitoring using improved genetic algorithms. *Smart Materials and Structures*, 13(3):528–534, April 2004.
- [32] N. Gupta and R. Sundaram. Fiber optic sensors for monitoring flow in vacuum enhanced resin infusion technology (VERITY) process. *Composites Part A: Applied Science and Manufacturing*, 40(8):1065–1070, 2009.
- [33] B. Harris. Fatigue in composites. Woodhead Publishing Limited, Cambridge, 2003.
- [34] T.R. Hay, R.L. Royer, H. Gao, X. Zhao, and J.L. Rose. A comparison of embedded sensor Lamb wave ultrasonic tomography approaches for material loss detection. *Smart Materials and Structures*, 15(4):946–951, June 2006.
- [35] D.A. Hutchins, D.P. Jansen, and C. Edwards. Lamb-wave tomography using non-contact transduction. *Ultrasonics*, 31(2):97–103, January 1993.
- [36] W. Hwang and K.S. Han. Cumulative Damage Models and Multi-Stress Fatigue Life Prediction. *Journal of Composite Materials*, 20(2):125–153, 1986.
- [37] W. Hwang and K.S. Han. Fatigue of composites–fatigue modulus concept and life prediction. *Journal of Composite Materials*, 1986.
- [38] J.B. Ihn and F.K. Chang. Pitch-catch active sensing methods in structural health monitoring for aircraft structures. *Structural Health Monitoring*, 2008.
- [39] The Freedonia Group Inc. High Performance Composites to 2016. *Self Published*, June 2012.
- [40] D.P. Jansen and D.A. Hutchins. Lamb wave tomography. In *IEEE Symposium on Ultrasonics*, pages 1017–1020. IEEE.
- [41] D.P. Jansen, D.A. Hutchins, and J.T. Mottram. Lamb wave tomography of advanced composite laminates containing damage. *Ultrasonics*, 32(2):83–90, March 1994.

- [42] K. Jung and T.J. Kang. Cure monitoring and internal strain measurement of 3-D hybrid braided composites using fiber Bragg grating sensor. *Journal of Composite Materials*, 41(12):1499–1519, June 2007.
- [43] A.L. Kalamkarov and S.B. Fitzgerald. The use of Fabry Perot fiber optic sensors to monitor residual strains during pultrusion of FRP composites. *Composites Part B: Engineering*, 1999.
- [44] H.K. Kang, D.H. Kang, and C.S. Hong. Monitoring of fabrication strain and temperature during composite cure using fiber optic sensor. In *Proceedings of SPIE*, 2001.
- [45] H.K. Kang, J.W. Park, and C.Y. Ryu. Development of fibre optic ingress/egress methods for smart composite structures. *Smart Materials and Structures*, 9:149–156, 2000.
- [46] S.S. Kessler and S.M. Spearing. Damage detection in composite materials using Lamb wave methods. *Smart Materials and Structures*, 2002.
- [47] C.J. Keulen, M. Yildiz, and A. Suleman. Multiplexed FBG and Etched Fiber Sensors for Process and Health Monitoring of 2-&3-D RTM Components. *Journal of Reinforced Plastics and Composites*, 30(12):1055–1064, 2011.
- [48] T. Kosaka, K. Osaka, and S. Nakakita. Fiber optic strain monitoring of textile GFRP during RTM molding and fatigue tests by using embedded FBG sensors. In *Proceedings of SPIE*, 2003.
- [49] K.S.C. Kuang. Use of conventional optical fibers and fiber Bragg gratings for damage detection in advanced composite structures: a review. *Applied Mechanics Reviews*, 2003.
- [50] B.C. Lee and W.J. Staszewski. Sensor location studies for damage detection with Lamb waves. *Smart Materials and Structures*, 16(2):399–408, 2007.
- [51] L.J. Lee, K.E. Fu, and J.N. Yang. Prediction of fatigue damage and life for composite laminates under service loading spectra. *Composites Science and Technology*, 56(6):635–648, 1996.

- [52] C. Lekakou, S. Cook, Y. Deng, T.W. Ang, and G.T. Reed. Optical fibre sensor for monitoring flow and resin curing in composites manufacturing. *Composites Part A: Applied Science and Manufacturing*, 37(6):934–938, June 2006.
- [53] R.L. Levy and S.D. Schwab. Monitoring the composite curing process with a fluorescence based fiber optic sensor. *Polymer composites*, 12(2):96–101, 1991.
- [54] R.E. Lyon, K.E. Chike, and S.M. Angel. In situ cure monitoring of epoxy resins using fiber-optic Raman spectroscopy. *Journal of Applied Polymer Science*, 53(13):1805–1812, September 1994.
- [55] J.F. Maguire and P.L. Talley. Remote Raman-Spectroscopy as a Sensor Technology in Composite-Materials Processing. *Journal of Advanced Materials*, 26(2):27–40, 1995.
- [56] F.L. Mathews. Finite element modelling of composite materials and structures. CRC Press LLC, Boca Raton, FL, 2000.
- [57] J.E. Michaels. Effectiveness of in situ damage localization methods using sparse ultrasonic sensor arrays. In *Proceedings of the SPIE*, 2008.
- [58] J.E. Michaels, A.J. Croxford, and P.D. Wilcox. Imaging algorithms for locating damage via in situ ultrasonic sensors. *Sensors Applications Symposium, 2008. SAS 2008. IEEE*, pages 63–67, 2008.
- [59] J.E. Michaels and T.E. Michaels. Damage localization in inhomogeneous plates using a sparse array of ultrasonic transducers. In *Review of Progress Quantitative Nondestructive Evaluation*, volume 26. Review of Quantitative Nondestructive Evaluation, 2007.
- [60] J.E. Michaels and T.E. Michaels. Guided wave signal processing and image fusion for in situ damage localization in plates. *Wave Motion*, 44(6):482–492, 2007.
- [61] A. Moustafa and S. Salamone. Fractal dimension–based Lamb wave tomography algorithm for damage detection in plate-like structures. *Journal of Intelligent Material Systems and Structures*, 2012.

- [62] V.M. Murukeshan, P.Y. Chan, and L.S. Ong. Cure monitoring of smart composites using fiber Bragg grating based embedded sensors. *Sensors and Actuators A-Physical*, 79:153–161, 2000.
- [63] M.L. Myrick, S.M. Angel, R.E. Lyon, and T.M. Vess. Epoxy cure monitoring using fiber-optic Raman spectroscopy. *SAMPE Journal*, 28:37–42, August 1992.
- [64] Y. Nagata, J. Huang, J.D. Achenback, and S. Krishnaswamy. Lamb wave tomography using laser-based ultrasonics. In *Review of Progress in Quantitative Nondestructive Evaluation*, volume 14, pages 561–568, 1995.
- [65] V. Natarajan and H.V.S. Gangarao. Fatigue response of fabric-reinforced polymeric composites. *Journal of Composite Materials*, 2005.
- [66] R.A. Neff and D.L. Woerdeman. Use of a charged coupled device (CCD) camera for evanescent wave optical fiber cure monitoring of liquid composite molding resins. *Polymer composites*, 1997.
- [67] J.H Nienwenhuis, J.J. Jr Neumann, D.W. Greve, and I.J. Oppenheim. Generation and detection of guided waves using PZT wafer transducers. *IEEE Transactions on ultrasonics, ferroelectrics and frequency control*, 52(11):2103–2111, 2005.
- [68] C. Novo, O. Frazão, A.N. Costa, A. Vieira, N. Correia, I. Dias, F.M. Araujo, and A.T. Marques. Progression monitoring of the flow front in RTM process using fibre Bragg grating sensors. *Society of Photo-Optical Instrumentation Engineers (SPIE) Conference Series*, 4185:808–811, 2000.
- [69] Y. Okabe, T. Mizutani, S. Yashiro, and N. Takeda. Detection of microscopic damages in composite laminates with embedded small-diameter fiber Bragg grating sensors. *Composites Science and Technology*, 2002.
- [70] C.A. Paget, S. Grondel, K. Levin, and C. Delebarre. Damage assessment in composites by Lamb waves and wavelet coefficients. *Smart Materials and Structures*, 12(3):393–402, 2003.
- [71] H.J. Paik and N.H. Sung. Fiberoptic intrinsic fluorescence for in-situ cure monitoring of amine cured epoxy and composites. *Polymer Engineering and Science*, 1994.

- [72] G. Park, H. Sohn, and C.R. Farrar. Overview of piezoelectric impedance-based health monitoring and path forward. *Shock and Vibration Digest*, 2003.
- [73] C. Prada, E. Kerbrat, D. Cassereau, and M. Fink. Time reversal techniques in ultrasonic nondestructive testing of scattering media. *Inverse Problems*, 18(6):1761–1773, 2002.
- [74] S.M. Prasad, K. Balasubramaniam, and C.V. Krishnamurthy. Structural health monitoring of composite structures using Lamb wave tomography. *Smart Materials and Structures*, 13(5):N73–N79, July 2004.
- [75] A. Raghavan and C.E.S. Cesnik. Review of Guided-wave Structural Health Monitoring. *Shock and Vibration Digest*, 2007.
- [76] A. Raghavan and C.E.S. Cesnik. Effects of Elevated Temperature on Guided-wave Structural Health Monitoring. *Journal of Intelligent Material Systems and Structures*, 19(12):1383–1398, 2008.
- [77] S.S.J. Roberts. Cure and fabrication monitoring of composite materials with fibre-optic sensors. *Composites Science and Technology*, 1993.
- [78] B. Rocha, C. Silva, and A. Suleman. Structural health monitoring system using piezoelectric networks with tuned lamb waves. In *Shock and Vibration*, pages 677–695, 2010.
- [79] J.L. Rose, A. Pilarski, and J.J. Ditri. An Approach to Guided-Wave Mode Selection for Inspection of Laminated Plate. *Journal of Reinforced Plastics and Composites*, pages 536–544, 1993.
- [80] A. Rotem. A Fatigue Failure Criterion for Fiber Reinforced Materials. *Journal of Composite Materials*, 1973.
- [81] M.M. Schwartz. *Composite Materials, Volume 2: Processing, fabrication, and applications*. Prentice Hall, Upper Saddle River, New Jersey, December 1997.
- [82] C.S. Shin. Fatigue damage monitoring in polymeric composites using multiple fiber Bragg gratings. *International Journal of Fatigue*, 2006.
- [83] H. Sohn, H.W. Park, K.H. Law, and C.R. Farrar. Combination of a time reversal process and a consecutive outlier analysis for baseline-free damage diagnosis. *Journal of Intelligent Material Systems and Structures*, 2007.

- [84] W.J. Staszewski. An overview of optimal sensor location methods for damage detection. In *Proceedings of SPIE*, 2001.
- [85] Z. Su and L. Ye. Selective generation of Lamb wave modes and their propagation characteristics in defective composite laminates. *Proceedings of the Institution of Mechanical Engineers Part L-Journal of Materials-Design and Applications*, 218:95–110, 2004.
- [86] Z. Su, L. Ye, and Y. Lu. Guided Lamb waves for identification of damage in composite structures: A review. *Journal of Sound and Vibration*, 295(3-5):753–780, August 2006.
- [87] N. Takeda. Characterization of microscopic damage in composite laminates and real-time monitoring by embedded optical fiber sensors. *International Journal of Fatigue*, 2002.
- [88] N. Takeda, S. Yashiro, and T. Okabe. Estimation of the damage patterns in notched laminates with embedded FBG sensors. *Composites Science and Technology*, 66(5):684–693, May 2006.
- [89] P. Tongpadungrod and T.D.L. Rhys. An approach to optimise the critical sensor locations in one-dimensional novel distributive tactile surface to maximise performance. *Sensors and Actuators A: Physical*, 2003.
- [90] S.W. Tsai, S. Ha, T.E. Tay, Y. Miyano, and S. Sihn. *Strength & Life of Composites*. Aero & Astro, Stanford U, 2008.
- [91] E. Udd. *Fiber optic smart structures*. John Wiley & Sons, Inc., New York, 1995.
- [92] E. Udd, J.P. Theriault, A. Markus, and Y. Bar-Cohen. Microbending fiber optic sensors for smart structures. *Society of Photo-Optical Instrumentation Engineers (SPIE) Conference Series*, 1170:478–482, February 1990.
- [93] W. Van Paepegem, I. de Baere, E. Lamkanfi, and J. Degrieck. Monitoring quasi-static and cyclic fatigue damage in fibre-reinforced plastics by Poisson’s ratio evolution. *International Journal of Fatigue*, 32(1):184–196, January 2010.

- [94] J.K. Van Velsor, H. Gao, and J.L. Rose. Guided-wave tomographic imaging of defects in pipe using a probabilistic reconstruction algorithm. *Insight - Non-Destructive Testing and Condition Monitoring*, 49(9):532–537, September 2007.
- [95] C.H. Wang, J.T. Rose, and F.K. Chang. A synthetic time-reversal imaging method for structural health monitoring. *Smart Materials and Structures*, 13(2):415–423, 2004.
- [96] F.W. Wang and B.M. Fanconi. In-Situ Characterization of the Interface of Glass Reinforced Composites. *National Bureau of Standards*, June 1987.
- [97] L. Wang and F.G. Yuan. Group velocity and characteristic wave curves of Lamb waves in composites: Modeling and experiments. *Composites Science and Technology*, 67:1370–1384, January 2007.
- [98] H.A. Whitworth. Modeling Stiffness Reduction of Graphite/Epoxy Composite Laminates. *Journal of Composite Materials*, 21(4):362–372, January 1987.
- [99] H.A. Whitworth. Cumulative Damage in Composites. *Journal of Engineering Materials and Technology*, 112(3):358, 1990.
- [100] H.A. Whitworth. A stiffness degradation model for composite laminates under fatigue loading. *Composite structures*, 1997.
- [101] P.D. Wilcox, M.J.S. Lowe, and P. Cawley. Mode and Transducer Selection for Long Range Lamb Wave Inspection. *Structural Health Monitoring*, 12(8):553–565, August 2001.
- [102] D.L. Woerdeman, J.K. Spoerre, and K.M. Flynn. Cure monitoring of the liquid composite molding process using fiber optic sensors. *Polymer Composites*, 1997.
- [103] K. Worden and J.M. Dulieu-Barton. An overview of intelligent fault detection in systems and structures. *Structural Health Monitoring*, 3(1):85–98, 2004.
- [104] D.C. Worlton. Experimental confirmation of Lamb waves at megacycle frequencies. *Journal of Applied Physics*, 32(6):967, 1961.
- [105] B. Xu and V. Giurgiutiu. Single mode tuning effects on Lamb wave time reversal with piezoelectric wafer active sensors for structural health monitoring. *Journal of Nondestructive Evaluation*, 26(2-4):123–134, October 2007.

- [106] F. Yan, R.L. Royer, and J.L. Rose. Ultrasonic Guided Wave Imaging Techniques in Structural Health Monitoring. *Journal of Intelligent Material Systems and Structures*, 21(3):377–384, February 2010.
- [107] J.N. Yang, D.L. Jones, and S.H. Yang. A stiffness degradation model for graphite/epoxy laminates. *Journal of Composite Materials*, 1990.
- [108] W.X. Yao. A new cumulative fatigue damage model for fibre-reinforced plastics. *Composites Science and Technology*, 2000.
- [109] S. Yashiro and T. Okabe. Estimation of fatigue damage in holed composite laminates using an embedded FBG sensor. *Composites Part A: Applied Science and Manufacturing*, 2011.
- [110] S. Yashiro, N. Takeda, T. Okabe, and H. Sekine. A new approach to predicting multiple damage states in composite laminates with embedded FBG sensors. *Composites Science and Technology*, 65:659–667, 2005.
- [111] G. Zhou. Damage detection and assessment in fibre-reinforced composite structures with embedded fibre optic sensors-review. *Smart Materials and Structures*, 2002.

Appendix A

**Multiplexed FBG and Etched Fiber Sensors for Process and Health
Monitoring of 2-&3-D RTM Components**



Multiplexed FBG and etched fiber sensors for process and health monitoring of 2- & 3-D RTM components

Casey J. Keulen¹, Mehmet Yildiz^{1,2} and Afzal Suleman¹

Abstract

This paper presents research being conducted on the use of a combination of fiber optic sensors for process and health monitoring of resin transfer molded (RTM) composite structures. A laboratory scale RTM apparatus has been designed and built with the capability of visually monitoring the resin filling process and embedding fiber optic sensors into the composite. Fiber Bragg gratings (FBG) and etched fiber sensors (EFS) have been multiplexed and embedded in quasi-2-D panels and 3-D hollow semicircular structures using a novel ingress/egress technique for the purpose of both process and structural health monitoring. The objective of this work is to demonstrate the simultaneous usage of FBGs and etched fiber sensors on a single optical fiber for resin flow monitoring and strain monitoring throughout the life of the composite. Three specimens are presented: one quasi-2D panel with two FBGs and three etched fiber sensors, one semicircular tube with two etched fiber sensors and one semicircular tube with two FBGs. Etched fiber sensors have been correlated with visual inspection to detect the presence of resin. Specimens with embedded FBG sensors have been tested in a tensile test machine to characterize the FBGs for strain monitoring.

Keywords

process monitoring, structural health monitoring, FBG, RTM, fiber optic sensors, smart materials, mechanical testing

Introduction

Composite materials are becoming increasingly more valuable in the transportation industry as they offer lighter weight options to traditional metallic structures. More than 20% of the Airbus A380 is made of composite¹ and over 50% of the Boeing 787 is made of composites.² Two major drawbacks of composites compared to metallic materials are the relatively difficult processing characteristics and damage assessment.

A number of processing methods exist for composite materials. One method that is particularly suitable to produce primary composite parts satisfying stringent specifications of the aircraft industry is the Resin Transfer Molding (RTM) technique. RTM will enhance the cost effectiveness of composites leading to affordable composites for primary structural components.³ RTM can produce high quality near net-shape parts with high fiber volume fractions, two high quality surfaces and little post processing in a fully contained system that eliminates human operator

exposure to chemicals and reduces the chance of human error.

A major drawback of RTM occurs during the resin injection stage. Due to a high resistance to resin (a relatively viscous material) flow through the preform (a material with low permeability) and geometry changes throughout the mold, it is not always possible to achieve a uniform flow pattern through the mold.⁴ This can lead to areas of the mold that do not become fully saturated with resin known as 'dry

¹University of Victoria, Department of Mechanical Engineering Victoria, Canada.

²Sabancı University, Faculty of Engineering and Natural Sciences, Advanced Composites and Polymer Processing Laboratory, Turkey.

Corresponding author:

Afzal Suleman, University of Victoria, Department of Mechanical Engineering, Victoria, B.C. V8W 3P6, Canada

Email: suleman@uvic.ca

spots'. These regions have a profound effect on the performance of the composite part since they are essentially a defect in the material.

Another drawback to composites is the difficulty in assessing damage. For example internal flaws in a composite component such as a dry spot, crack or delamination may be present that are not visible. This defect may subsequently grow leading to catastrophic failure with little warning. With traditional inspection methods it is difficult, time consuming and expensive to detect and assess damage in composites. Fiber optic sensors that are embedded in critical regions of composite components can be used to monitor the condition or health of the material in real time and accurately characterize stress and strain and detect damage in a component.⁵ This is known as Structural Health Monitoring (SHM).⁶ Fiber optic sensors also have the ability of detecting the presence of resin and can be used during the injection process to ensure that the mold is fully saturated. The small diameter and flexibility of optical fiber allows it to be embedded into composite materials with negligible impact to the structural integrity of the host material.⁵

Fiber Bragg Gratings (FBGs) are becoming increasingly more popular for such applications due to their advantages such as their size, immunity to electro magnetic interference, multiplexing potential and absolute reading. FBGs can be used to measure strain and temperature among other properties. Another useful sensor is an etched fiber sensor (EFS). This type of sensor is quite simple; a small section of optical fiber is etched to expose the core. When this etched region is surrounded by resin (fluid) flowing through the mold, the light power that is transmitted through the optical fiber changes hence enabling the sensor to detect fluid.⁷ Since both EFS and FBG sensors allow light to pass there is potential for them to be multiplexed on one single fiber.

Many researchers have studied the use of a single type of embedded fiber optic sensor, however, there is less exploration into the use of a combination of sensor types on a single optical fiber. Most of the work that has been done involves the combination of FBG and extrinsic Fabry-Perot interferometer (EFPI) sensors.⁸ EFPI sensors cannot be multiplexed on a single fiber; this severely limits their use when multiple sensors are required. Since ingress/egress issues of fiber optics are not trivial it is highly desirable to minimize the number of instances by placing the largest practical number of sensors on one single fiber. If optical fiber is embedded for the use of sensors in one particular stage of a composite material's life (such as in service) then it is only logical to optimize the use of the fiber and combine sensors that could be used during other stages such as manufacturing.

In the first part of this study, two FBG sensors and three EFS sensors multiplexed on a single fiber are embedded in a fiberglass panel with a purpose built RTM mold that has a glass viewing window that allows for visual monitoring of the resin injection process. The sensors are monitored during injection to detect the presence of resin and indicate possible dry spots. The viewing window in the mold is used to confirm the sensor readings. Two EFS sensors are also embedded in a semicircular tube to demonstrate their applicability to 3D surfaces such as those found in aerospace applications.

The second part of this study involves the use of embedded FBG sensors to detect strain in the composite. Specimens are prepared and tested in a material test machine to determine the strain sensitivity of the FBGs.

Resin transfer molding

The RTM process involves loading a two sided, fully enclosed mold with a fiber perform, closing the mold, injecting resin into the mold until fully saturated, allowing the resin to cure and removing the molded part.⁴

To produce RTM composite components with embedded fiber optics a sophisticated laboratory-scale apparatus has been designed and built. The apparatus has the flexibility of accommodating different mold designs and thicknesses, with the feature of a glass viewport to allow for visual monitoring of resin flow during the injection process. It has been tested by producing composite parts with different geometries such as flat panels, hollow and foam cored square, and semicircular tubes made from various types of reinforcements.

Experimental apparatus

The general layout of the experimental apparatus is shown in Figure 1. The apparatus can be separated into seven separate components: the injection system, injection valve, mold, manipulating/clamping fixture, catchpot, vacuum pump, and temperature controller. It can be described as a clamshell system with the mold mounted on it. For a mold to be used with this apparatus it must be 533 mm × 850 mm. Any thickness is possible with minor modifications to the clamping system.

Embedded optical fiber

Fiber optic ingress/egress is one of the most important issues for the application of embedded fiber optic sensors in real composite components⁹ and has been addressed by various researchers,^{5,8,9} however, little information on ingress/egress with RTM is available

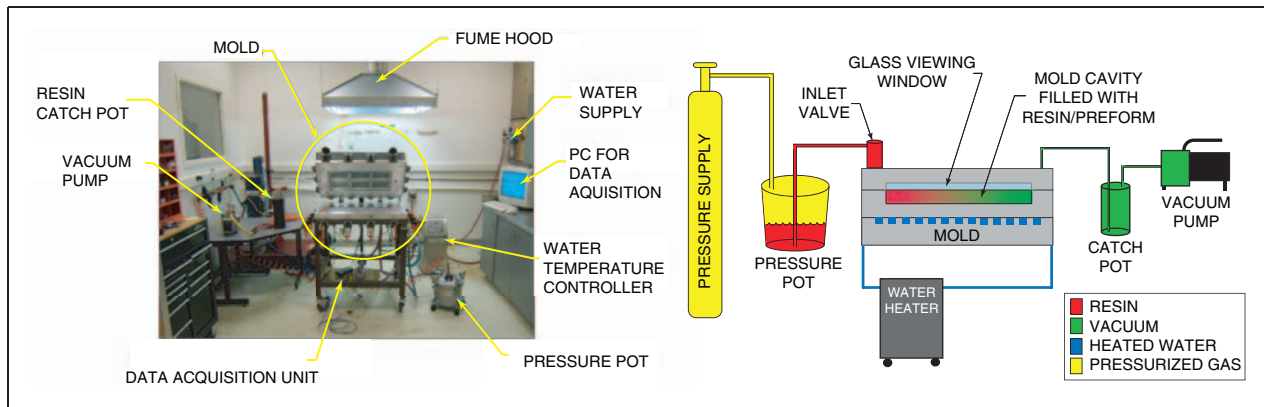


Figure 1. Layout (left) and schematic of RTM apparatus (right).

in the literature. The closed nature of the RTM process as well as the extremely fragile nature of optical fiber makes the ingress/egress of FBG sensors into the mold challenging. Sealing issues also arise due to the extremely small diameter of the optical fiber.

When optical fiber is embedded with the in-plane method, the ingress/egress point of the optical fiber is located at the edge of the composite. This eliminates the possibility of trimming the outer edges of the composite to size, a very common practice in the industry. To remove a composite part from a mold it must be removed normal to the mold, therefore, the embedded fibers must enter and exit through the mold so that upon removal, the fibers are not severed. A novel through thickness ingress/egress method has been developed, which can overcome the limitations of the in-plane method and be applicable to closed mold processes such as RTM.

Ingress/egress technique

A novel method to achieve a through thickness ingress/egress that is applicable to pressurized injection molding such as RTM has been developed. Two major obstacles were overcome when developing this technique, sealing the optical fiber and protecting the fiber as it entered the mold.

Optical fiber is quite delicate and must maintain a minimum bend radius before it fractures. When a through thickness fiber ingress technique is used the fiber sees an abrupt 90° bend as it travels through the mold and into the thin composite part as shown in Figure 2 (left). This is inherent to any through thickness ingress/egress technique.

To protect the fiber with minimal disturbance to the composite material a thin hypodermic tube is placed around the fiber. This protects the fiber through the radius of the bend as well as reinforces the fiber at the ingress/egress point once the part is removed from

the mold. As one would imagine it is difficult to seal around something as small as an optical fiber that has an outer diameter of 250 μm without permanently caulking or bonding the fiber into the mold. A tapered silicone stopper was used to seal around the hypodermic tube as shown in Figure 2 (right). A custom fitting is used to keep the stopper and fiber in place. Figure 3 shows the panel and semicircular tube with embedded optical fiber.

The novelty of this technique lies in the use of the tapered silicon stopper and custom fitting. One technique briefly reported by Kosaka T, et al.¹⁰ involves the use of a plastic plug that seals the fiber into the mold and remains bonded to the surface of the composite once it is demolded. The detractor of this technique is that the plastic can become debonded from the composite while in service thereby severing the fiber and rendering the system useless. Also, the fiber must be sealed to the plastic, likely with a caulking that requires time to cure and cannot be removed or adjusted if required. The technique developed and described here overcomes these detractors by using a tapered silicon stopper that applies pressure to the hypodermic tube thereby sealing it instantly without any caulking. This allows the fiber to be adjusted at any point prior to injection. Since the stopper is silicon it is easily removed after molding. This technique can be applied to a mold of any thickness over 10 mm by simply adjusting the length of the fitting. This modularity comes in useful due to the wide variation of RTM molds. The fitting also allows the injection pressure to be quite high since it is threaded into the mold making this technique applicable to higher-pressure injection techniques such as SRIM and thermoplastic injections.

Fiber Bragg gratings

Fiber Bragg gratings (FBGs) are becoming increasingly more popular for many applications due to their

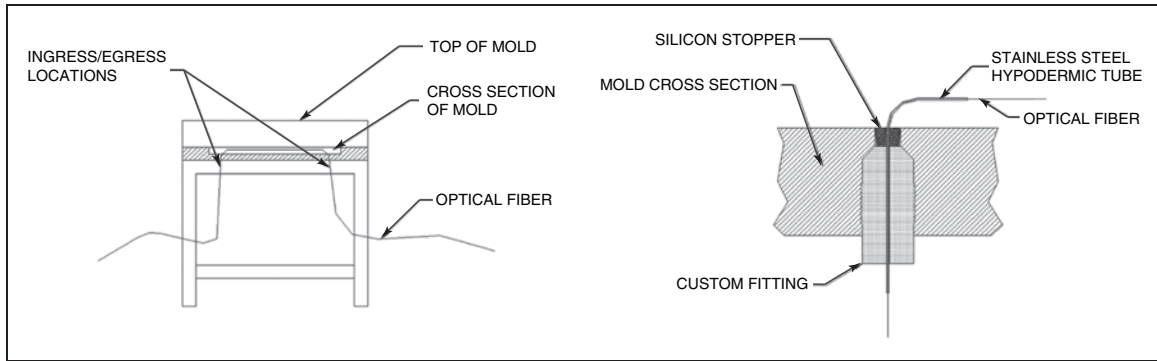


Figure 2. Path of fiber for through thickness ingress/egress (left), and the schematic of fiber sealing (right).

previously stated advantages. They have been used to measure properties such as displacement, strain, temperature, pressure, humidity, and radiation dose among others.¹¹ FBGs were first demonstrated by Hill in 1978.¹² Embedded FBGs can be used for three distinct purposes during the life of a resin transfer molded part. An array of FBGs in a mold can monitor the mold filling process and can ensure that the mold is completely filled with resin as demonstrated by Novo et al.¹³ Once injected the resin must go through a specific time-temperature cure cycle. In complicated 3-D parts with varying thicknesses and surface areas, different regions of resin cure at different rates and to varying degrees across the part. FBGs have been used to monitor the cure throughout the part.^{8,14-16} Once in service the embedded FBGs can be used in a variety of ways to monitor the health of the part thereby reducing maintenance cost and service time while increasing safety.¹⁷⁻¹⁹

A fiber Bragg grating is a segment of a single mode optical fiber core with a periodically varying refractive index in the axial (longitudinal) direction and commonly created using a high intensity UV laser.²⁰ It allows a broad band of light to pass through while reflecting back a narrow band based on a wavelength known as the Bragg wavelength. The reflected wavelength depends on the grating pitch (spacing between the refractive index variations) and the variation in refractive index. The periodic modulation of the refractive index at the grating location will scatter the light traveling inside the fiber core. Out of phase scattered waves will form destructive interference thereby canceling each other and in phase light waves will add up constructively forming a reflected spectrum with a center wavelength known as the Bragg wavelength. Figure 4 describes an FBG.

The Bragg wavelength satisfies the Bragg condition as Equation (1):²⁰

$$\lambda_B = 2n\Lambda \quad (1)$$

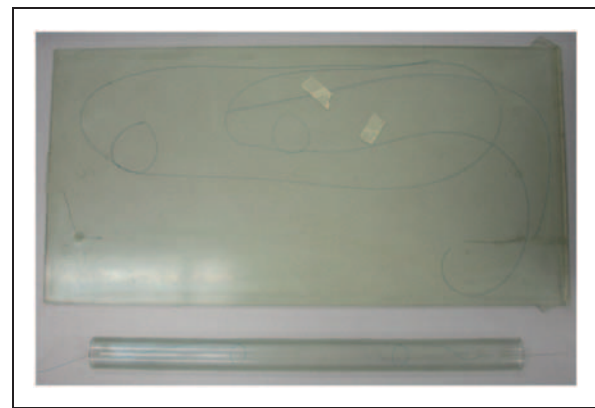


Figure 3. A panel and semicircular tube with embedded optical fiber.

where λ_B is the back-reflected Bragg wavelength, n is the average refractive index of the fiber core and Λ is the spacing between gratings. The change in spacing of the periodic refractive index modulation is a function of strain and temperature. If an FBG sensor is under a mechanical or thermal load (temperature variation), the spacing and average refractive index will change due to the strain, and thermal expansion, respectively. Since the Bragg wavelength, $\lambda_B(n, \Lambda)$ is a function of the average refractive index and grating pitch, any change in these variables will cause the Bragg wavelength to shift.

Since the center wavelength of Bragg gratings are sensitive to both temperature and strain variations, in sensing applications where only temperature or strain measurement is of interest, the effect of temperature or strain on the grating must be compensated to measure only one of these effects. The literature reveals that Bragg gratings offer a very good linearity between the measured strain and applied stress. Multiple Fiber Bragg gratings sensors can be easily multiplexed onto a single strand of fiber, thereby forming an array of FBG sensors for distributed strain measurements over a large distance. An array of FBG sensors minimizes

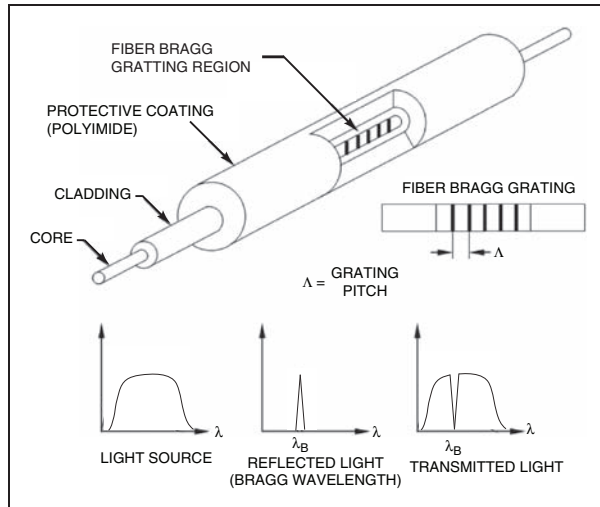


Figure 4. Schematic describing an FBG sensor.

the number of ingress/egress locations during the embedding process in the smart structure.

In the case of embedded FBGs, the load on the host is directly transferred onto the grating region through shear action, resulting in the change in the length of the grating region. As a result, the grating spacing and the refractive index of the grating change, allowing the determination of mechanical properties. The presence of the damage or defect formation in a composite structure alters the local strain distribution under a structural load. Damage can be detected when the measured strain deviates appreciably from the value expected of a healthy structure at the sensor location. This allows for monitoring the structural health of composite components under service conditions.

Etched fiber sensors

Etched fiber sensors are an excellent low cost method of detecting the presence of resin. Operation of etched fiber sensors is quite simple requiring only standard equipment found in most optics lab. Essentially, a light source launches light into one end of the fiber optic and an optical power meter measures the light intensity at the other end. When resin makes contact with the sensor there is a sudden, sustained drop in the transmitted light intensity.²¹ The amount of light lost through the etching is a function of the refractive index of the medium it is in.²² This type of sensor has been used to measure the permeability of fiber perform materials by Ahn et al.⁹ and Lim et al.²³ among others.

The theory behind the etched fiber sensor is very basic; it pertains to the fundamental principles of light transmission through optical fiber. The sensor consists of a small section of optical fiber roughly 3–5 mm long with the cladding removed leaving the

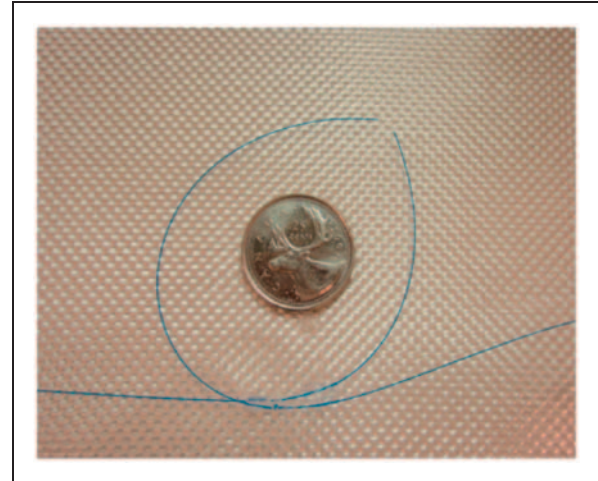


Figure 5. Looped etched fiber sensor.

fiber core exposed. Light is contained in the core of an optical fiber by the cladding. As light travels through the core of a fiber it is continuously bouncing off the cladding. When the light reaches the section of fiber where the cladding is removed a small portion of it escapes while most is transmitted.²⁴ When resin contacts the core its refractive index being higher than that of the glass causes more light to escape. Therefore, the amount of light transmitted through the fiber is less.

A novel variation of the basic sensor is used in this study. This variation involves looping the etched sensor to create a bend in the etched portion of the fiber. This is done to allow more light to escape from the sensor while leaving some of the cladding on the core to physically protect it. The looped variation is a more robust version of the sensor that is easier to handle and implement. Another benefit of looping the fiber is that the sensitivity can be tuned by adjusting the radius of the loop. As the radius of the loop increases the amount of transmitted light increases. This option is desirable when multiple sensors are used on a single strand of fiber and minimum light loss is desired so that all sensors can make readings. Figure 5 shows the sensor with a Canadian quarter for reference (23.81 mm diameter); note the etched section in the upper right portion of the loop.

Sensor characterization

To demonstrate the capabilities and multiplexing potential of FBGs and etched fiber sensors, experiments were performed in the aforementioned RTM apparatus using the described ingress/egress technique. The experiments validated the ability of the EFS sensors to detect the presence of resin during the RTM process and the FBG sensors to be used to detect strain all while

multiplexed on a single fiber. To explore the versatility and potential for different applications of these sensors three different specimens were produced; a quasi 2-D flat panel and two 3-D hollow tubes with a semicircular cross-section.

The flat panel was composed of 18 plies of 200 gsm plain weave glass fiber cloth and Huntsman Renfusion 8601 epoxy resin, with dimensions of 610 mm × 305 mm × 3 mm. An optical fiber containing three EFS sensors and two FBG sensors was embedded on the upper ply of the panel.

Two semicircular tube specimens were produced; one composed of five layers and the other composed of six layers of 200 gsm plain weave glass fiber cloth and Huntsman Renfusion 8601 epoxy resin fully enclosing a steel mandrel that is removed after molding. The tube has an outer radius of 38 mm, length of 500 mm, and wall thickness of 1.5 mm. In the specimen composed of five layers, an optical fiber containing two EFS sensors is embedded between the fourth and fifth ply on the curved surface of the specimen. The specimen composed of six layers contains two FBGs embedded between the fourth and fifth ply on the curved surface of the specimen. The inner layer is considered the first layer in these specimens increasing towards the outside of the tube.

Flow monitoring

Flow monitoring experiments were performed during the resin transfer molding process. The general procedure was similar for both specimens and involved embedding the optical fiber in the mold, closing it, and injecting the resin. The optical fiber was connected to a photodetector and measurements were logged throughout the injection process.

Flow monitoring of panel specimen An optical fiber containing three EFS sensors (EFS#1,2,3) and two FBG sensors (FBG#1,2,3) was embedded into the mold on the upper ply of the laminate, the mold was closed and the resin was injected. Etched fiber sensor readings were recorded with a photodetector and data logger while the FBGs were manually observed with an OSA. A simple circuit was used to interrogate the sensors as shown in Figure 6. A BBS light source is connected to one end of the optical fiber, the fiber runs through the mold, a 50/50 coupler is connected to the other end of the fiber with one branch of the coupler going to the photodiode and the other to an OSA.

Figure 7 shows the sensors through the glass viewing window prior to injection. Figure 8(a) shows the resin approaching EFS #1 while Figure 8(b) shows the resin just after the sensor is saturated and the transmitted light intensity is reduced. This occurs roughly 2.4 min

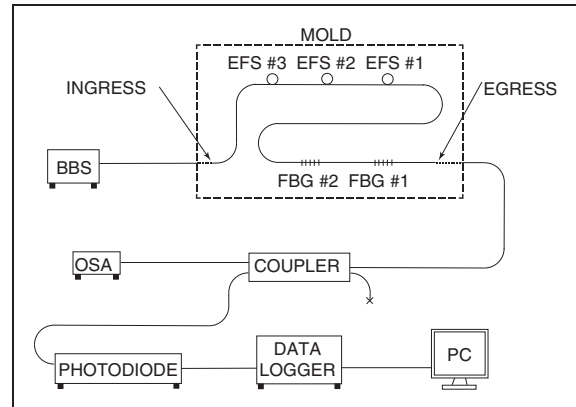


Figure 6. Interrogation system.

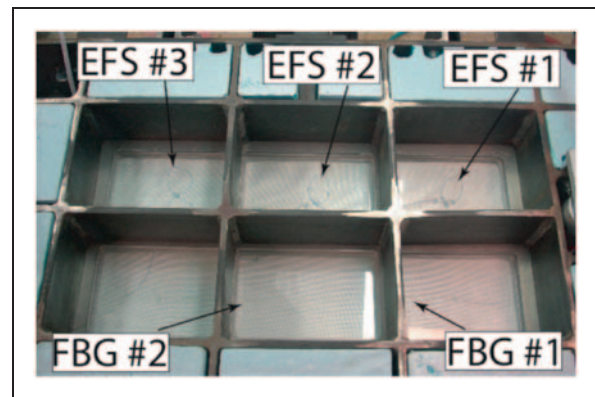


Figure 7. Sensors positioned in RTM prior to injection (mold closed).

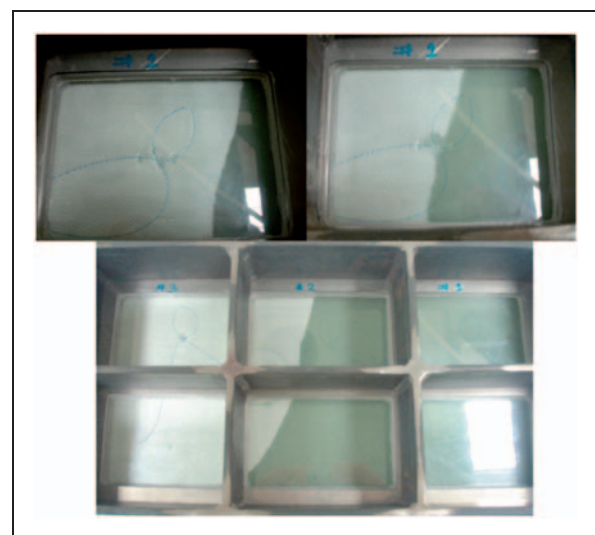


Figure 8. CW from top left: (a) resin approaching sensor, (b) resin just after contacting sensor, and (c) mold midway through injection.

into the injection. Figure 8(c) shows the mold midway through the injection.

Figure 9 shows a plot of the photodiode voltage output vs. injection time. It can clearly be seen that as the resin reaches the first sensor at roughly 2.4 min there is a sharp and sustained drop in the transmitted light. Another drop occurs at roughly 7.7 min when the resin reaches the second sensor and again at 12.2 min when the resin reaches the third sensor. Once the mold was saturated and the injection was complete, the light source was turned off to ensure that the readings could be differentiated from a change in minimal transmitted light and no transmitted light. When the light source was off the photodiode output was zero. The light source was turned back on and the transmitted light intensity was the same as before it was turned off, therefore, indicating that light was indeed being transmitted. During this time the FBG sensors were manually observed with the OSA to ensure that they were still functional. Due to the arrangement of the sensors on the fiber (FBG before EFS) no change in power was noticed when resin contacted the EFS sensors, therefore, demonstrating that the EFS do not effect the FBG sensors as long as they are situated after the FBGs on the fiber. The FBG output is not included here, however this technique has been thoroughly researched by others such as Novo et al.²³ and Eum et al.^{24,25}

Flow monitoring of 3-D semicircle specimen To demonstrate the versatility and applicability of these sensors to more realistic structures, an optical fiber containing two EFS sensors was embedded in a hollow tube with a 3-D semicircle cross-section using the aforementioned RTM apparatus. The sensors were embedded between the fourth and fifth layers on the curved surface of the semicircle. The flat side of the semicircle is visible through the viewing window, however the curved surface is not. Due to the relatively

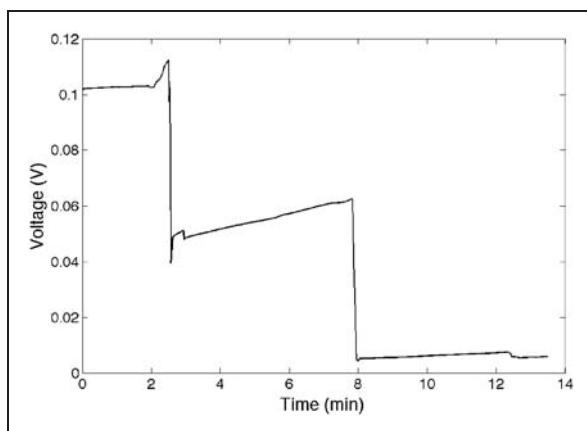


Figure 9. Plot of photodiode output vs. injection time for panel.

small radius of the tube and uniform resin flow it can be estimated with a high level of confidence that the resin is in contact with the sensors and their output can be verified. This is a more realistic experiment for these sensors since the majority of industrial molds are not translucent.

The sensors were interrogated in a manner similar to that shown in Figure 6. Figure 10 shows the specimen with the sensors visible. Data was recorded during the injection and is shown in Figure 11 showing resin arrival at the first and second EFS at roughly 2.9 and 4.0 min, respectively.

Strain sensitivity characterization

For FBGs to be used as strain sensors after they are embedded in a composite material the relationship between the shift in the Bragg wavelength and the axial strain in the sensor must be known. This relationship is known as the sensitivity or the strain gage factor, S . Embedded FBG strain gages experience additional radial strain field in application, therefore once integrated into a structure, every gage must be recalibrated.²⁶

The strain gage factor for an electrical foil strain gage can be described as the relationship between the resistance of the wire, R , axial strain ϵ_a and the change in resistivity of the wire.²⁷ The expression for the strain gage factor is given in Equation (2):

$$S = \frac{dR/R}{\epsilon_a} \quad (2)$$

For an FBG, the gage factor would be the relationship between the change in the Bragg wavelength and axial strain. The expression for this is shown in Equation (3):

$$S = \frac{\delta\lambda_B}{\epsilon_a} \quad (3)$$

To determine the gage factor for both 2- and 3-D specimens they were tested in an MTS 810 material test machine. A 6 mm grid, 120 ohm strain gage from Omega Engineering Inc. was bonded to the surface directly beside the FBG. The strain gage was connected to a Measurements Group Instrument Division P-3500 strain indicator and the FBG was hooked up to an Ando AQ6331 OSA, JDS Uniphase broadband light source and a 50:50 optical coupler. Figure 12 shows the 2-D specimen in the MTS machine with the instrumentation equipment (left) and a close up of the 3-D specimen (right).

Strain sensitivity of panel specimen To determine the gage factor for the panel a tensile specimen was cut out



Figure 10. Semicircular tube with embedded fiber optic sensors.

of the RTM'd panel. The specimen has dimensions of 38.1 mm × 300 mm × 3 mm. The embedded FBG is located directly in the middle of the specimen along the length and width. Small pieces of sand paper were bonded to the ends of the specimen to help the test machine grip without slipping.

The specimen was loaded into the test machine and a tensile load was applied at a rate of 0.051 mm/min up to a maximum of roughly 2.88 mm. Readings were taken at roughly 0.254 mm intervals starting at zero strain. The test was repeated four times to ensure the repeatability of the results. Figure 13 shows a plot of the collected data, namely, Bragg wavelength vs. measured strain.

A linear line was fit to the data with an equation of $y = 0.001141x + 1541.04$ with an R^2 value of 0.999 obtained from four test runs. From this equation we can ascertain that $S = 1.141e-3$ or every 1.141 pm shift in the Bragg wavelength is equal to one micro strain.

Strain sensitivity of semicircular specimen To determine the gage factor for the semicircular tube a special fixture was designed to restrain the specimen in the aforementioned MTS machine for compression testing. Semicircular blocks, 38 mm long with the same cross-sectional dimensions as the mandrel were fastened to adapter plates that interface with the test machine. The tube was cut at its mid-length to produce two specimens and simplify the testing process. Each specimen has one FBG at the midspan.

The specimen was slid onto the fixture and a compression load was applied then released. This was repeated twice to ensure repeatability. The strain gage output (in microstrain) and Bragg wavelength (in nm) was recorded as the load was applied and released. The recorded data is plotted and shown in Figure 14.

A linear line was fit to the data and an equation of $y = 0.001288x + 1541.28$ with an R^2 value of 0.999 was obtained from four test runs (two loading, two unloading). From this equation we can ascertain that

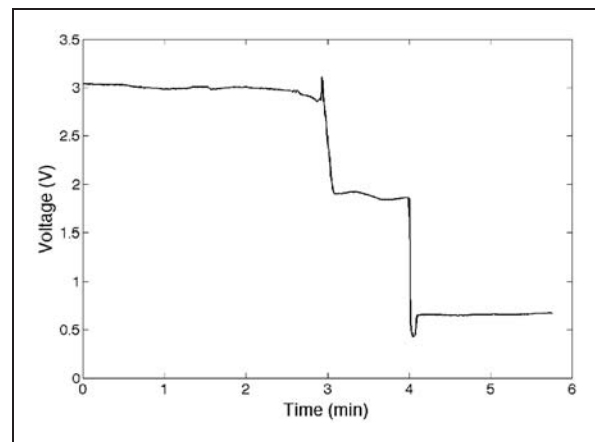


Figure 11. Plot of photodiode output vs. injection time for tube.

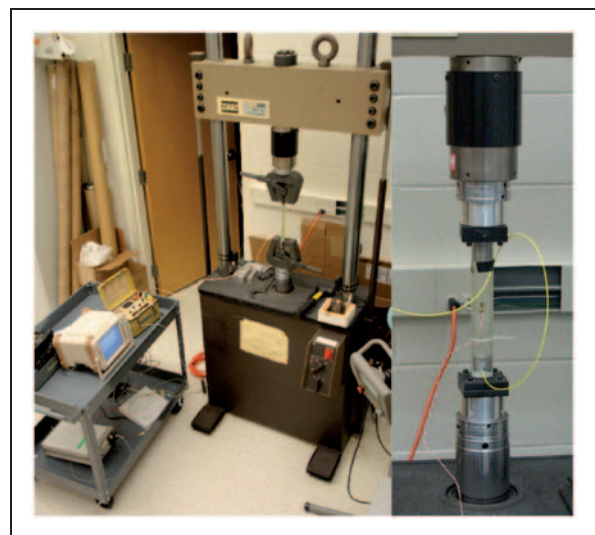


Figure 12. 2-D specimen in MTS machine with instrumentation equipment (left) and 3-D specimen loaded in MTS machine (right).

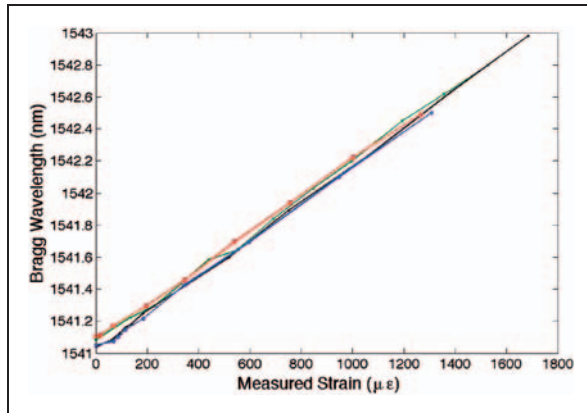


Figure 13. Bragg wavelength vs. strain gage measured strain for 2-D panel.

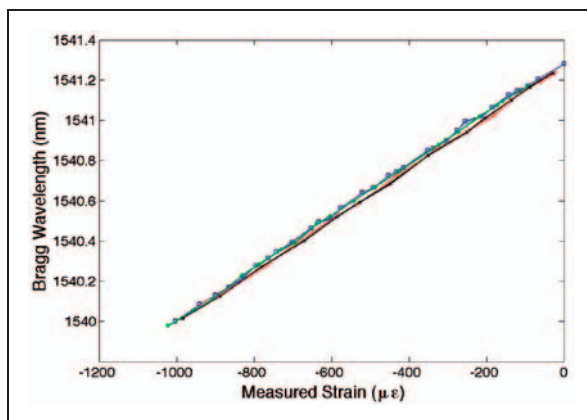


Figure 14. Bragg wavelength vs. strain gage measured strain for 3-D structure.

$S = 1.288e-3$ or every 1.288pm shift in the Bragg wavelength is equal to one micro strain.

Strain sensitivity discussion As mentioned earlier the strain sensitivity of the embedded FBG is $1.141\text{ pm}/\mu\epsilon$ for the flat panel specimen and $1.288\text{ pm}/\mu\epsilon$ for the semicircular specimen. These sensitivities deviate from the commonly referenced value of $1.2\text{ pm}/\mu\epsilon$ for a bare FBG with typical material properties²⁰ by -4.9% and 7.3% for flat panel and semicircular specimens, respectively. These values fall within the range of deviation reported by Fan et al.²⁶ Factors such as variations in the material and manufacture of each individual FBG and experimental error in the processing and testing phase such as misalignment of FBG or strain gage with the axis of the specimen may contribute to this deviation. Another factor which may contribute to the variation in sensitivity between the two geometries is the mismatch of mechanical properties between the

FBG fiber and host structure, particularly their Poisson ratio in the lateral direction as embedded sensors experience an additional radial strain field when load is applied along the sensor direction.²⁶

Conclusion

The motivation behind this study is to advance the knowledge base of embedded optical fiber sensors by: (i) designing and fabricating an RTM apparatus capable of embedding optical fibers that allows visual monitoring of the injection process, (ii) embed EFS and FBG sensors on a single optical fiber into a composite panel with this apparatus, (iii) detect the presence of resin during the injection with the EFSs, and (iv) measure the strain in test specimens with the FBGs. The RTM apparatus has been manufactured and successfully tested. A method of embedding fiber optics has also been devised and tested. The apparatus was used to embed an optical fiber with three EFSs and two FBGs into a quasi-2-D panel, two EFSs in one semicircular tube and two FBGs in a second. The glass window in the mold was used to visually monitor the resin flow while a photodiode and data logger was used to take readings from the etched sensors. Both panel and tube specimens with a foil strain gage bonded to the surface were tested in a material test machine to determine the strain gage factor of the FBG.

This study successfully demonstrates the ability of multiplexing a number of optical sensors onto a single fiber and embedding them into resin transfer molded composite parts of various shapes and complexities. The FBGs were not used during the manufacturing process, however in the future they could be used to monitor the degree of cure of the resin as has been researched by.¹⁴⁻¹⁶ The EFSs showed a high degree of accuracy at detecting the presence of resin however the readings of various EFSs could not be differentiated without a priori knowledge of the resin flow. Implementing OTDR would potentially allow the sensors to be differentiated.

With the implementations of the demonstrated techniques RTM parts could be manufactured more efficiently with a higher degree of quality at a lower cost.

Acknowledgements

The authors gratefully acknowledge the funding provided by the Canadian NSERC RTI equipment grant, project number: EQPEQ 390418-2010. Also, the second author gratefully acknowledges the funding provided by The Scientific and Technological Research Council of Turkey (TUBITAK) under the support program of scientific and technological research projects (1001) for project number 108M229.

References

1. Marks P. Aviation – the shape of wings to come. *New Scientist*, June 2005. <http://www.newscientist.com/article/dn7552> (accessed 7 December 2009).
2. Hawk J. The Boeing 787 dreamliner: more than an airplane. In: *Presentation to AIAA/AAAF Aircraft Noise and Emissions Reduction Symposium*, American Institute of Aeronautics and Astronautics and Association Aéronautique et Astronautique de France, May 2005.
3. Graf NA. Evaluation of automated RTM process and materials for naval aircraft. International SAMPE technical conference, Vol. 33, 2001, pp. 1133–1147.
4. Schwartz MM. Composite materials, volume II: Processing, fabrication and applications. *Upper Saddle River*. New Jersey: Prentice Hall PTR, 1997.
5. Udd E. *Fiber optic smart structures*. New York: John Wiley & Sons, Inc., 1995.
6. Worden K, et al. The fundamental axioms of structural health monitoring. *Proc Math Phys Eng Sci* 2007; 463: 1639–1664.
7. Ahn SH, Lee WI and Springer GS. Measurement of the three-dimensional permeability of fiber preforms using embedded fiber optic sensors. *J Compos Mater* 1995; 29(6).
8. Kang HK, Park JW, Ryu CY, Hong CS and Kim CG. Development of fibre optic ingress/egress methods for smart composite structures. *Smart Mater Struct* 2000; 9: 149–156.
9. Green AK, Darvish S and Shafir E. Practical terminations for optical fibers embedded in composite materials. *Proc Soc Photo Opt Instrum Eng* 1996; V: 2779.
10. Kosaka T, Osaka K, Nakakita S and Fukuda T. Fiber optic strain monitoring of textile GFRP during RTM molding and fatigue tests by using embedded FBG sensors. *Proc SPIE* 2003; V: 5056.
11. Dennison CR and Wild PM. Enhanced Sensitivity of an in-fiber Bragg grating pressure sensor achieved through fiber diameter reduction. *Meas Sci Technol* 2008; 19.
12. Hill KO. Photosensitivity in optical fiber waveguides: Application to reflection fiber fabrication. *Appl Phys Lett* 1978; 32: 647.
13. Novo C, et al. Progression monitoring of the flow front in RTM process using fibre Bragg grating sensors. *Proc Soc Photo Opt Instrum Eng* 2000; V: 4185.
14. Dweynter-Marty V, et al. Embedded fiber bragg grating sensors for industrial composite cure monitoring. *J Intell Mater Syst Struct* 1998; 9.
15. Murukeshan VM, Chan PY, Ong LS and Seah LK. Cure monitoring of smart composites using fiber Bragg grating based embedded sensors. *Sens Actuators A Phys* 2000; 79: 153–161.
16. Jung K and Kang TJ. Cure monitoring and internal strain measurement of 3-D hybrid braided composites using fiber Bragg grating sensor. *J Compos Mater* 2007; 41(12).
17. Leng J and Asundi A. Structural health monitoring of smart composite materials by using EFPI and FBG sensors. *Sens Actuators A Phys* 2003; 103: 330–340.
18. Sundaram R, Kamath GM, Gupta N and Rao MS. Structural health monitoring of co-cured composite structures using FBG sensors. *Proc Soc Photo Opt Instrum Eng* 2005; 5764.
19. Guo ZS. Strain and temperature monitoring of asymmetric composite laminate using FBG sensors. *Struct Health Monitor* 2007; 6(3).
20. Othonos A and Kalli K. *Fiber Bragg gratings, fundamental and applications in telecommunications and sensing*. Boston, Massachusetts: Artech House Inc., 1999.
21. Lim ST and Lee WI. An analysis of the three-dimensional resin transfer mold filling process. *Compos Sci Technol* 2000; 60: 961–975.
22. Hect J. *Understanding fiber optics*. Upper Saddle River. New Jersey: Pearson Education, Inc., 2006.
23. Novo C, Frazao O, Costa AN, Vieira A, Correia N, Dias I, et al. Progression monitoring of the flow front in RTM process using fibre Bragg grating sensors. *Proc SPIE* 2000; 4185.
24. Eum S, Kageyama K, Murayama H, Ohsawa I, Uzawa K, Kanai M, et al. Resin flow monitoring in vacuum-assisted resin transfer molding using optical fiber distributed sensor. *Proc SPIE* 2007; 6526.
25. Eum S, Kageyama K, Murayama H, Uzawa K, Ohsawa I, Kanai M, et al. Process/health monitoring for wind turbine blade by using FBG sensors with multiplexing techniques. *Proc SPIE* 2008; 7004.
26. Fan Y and Kahrizi M. Characterization of a FBG strain gage array embedded in composite structure. *Sensors Actuat A* 2005; 121: 297–305.
27. Wheeler AJ and Ganji AR. *Introduction to engineering experimentation*, 2nd ed. Upper Saddle River: Pearson Education, Inc., 2004.

Appendix B

An Experimental Study on the Process Monitoring of Resin Transfer Molded Composite Structures Using Fiber Optic Sensors

An Experimental Study on the Process Monitoring of Resin Transfer Molded Composite Structures Using Fiber Optic Sensors

Mehmet Yildiz

e-mail: meyildiz@sabanciuniv.edu

Nazli G. Ozdemir

e-mail: gulsine@sabanciuniv.edu

Gokhan Bektas

e-mail: bektas@sabanciuniv.edu

Advanced Composites and Polymer

Processing Laboratory,

Faculty of Engineering and Natural Sciences,

Sabanci University,

Orhanli-Tuzla,

34956 Istanbul, Turkey

Casey J. Keulen

Mechanical Engineering Department,

University of Victoria,

Victoria, BC, Canada

e-mail: ckeulen@uvic.ca

Talha Boz

e-mail: talhaboz@sabanciuniv.edu

Ege F. Sengun

e-mail: egesengun@sabanciuniv.edu

Cem Ozturk

e-mail: cemozturk@sabanciuniv.edu

Yusuf Z. Menceloglu

e-mail: yusufm@sabanciuniv.edu

Advanced Composites and Polymer

Processing Laboratory,

Faculty of Engineering and Natural Sciences,

Sabanci University,

Orhanli-Tuzla,

34956 Istanbul, Turkey

Afzal Suleman

Mechanical Engineering Department,

University of Victoria,

Victoria, BC, Canada

e-mail: suleman@uvic.ca

Research conducted on in situ process monitoring of resin transfer molded composites with fiber optic sensors is presented. A laboratory scale resin transfer molding (RTM) apparatus was designed and built with the capability of embedding fiber optic sensors and visually observing the resin filling process. Both fiber Bragg grating (FBG) and etched fiber (EF) sensors are embedded into glass fiber reinforcements in the RTM mold and used to monitor the resin flow front and cure. The cure cycle of the resin system utilized in this work is also studied using a Fresnel reflection refractometer (FRR) sensor. The results of this study show that both the FBG and EF sensors can be used efficiently for flow and cure monitoring of the RTM process. The experimental results of the EF and FRR sensors agree with those of the FBG sensors for cure monitoring. [DOI: 10.1115/1.4006770]

Keywords: resin transfer molding, process monitoring, composite materials, fiber optic sensors

1 Introduction

Composite materials offer many advantages over conventional metallic materials. They are utilized in a variety of load bearing structures such as aircraft fuselages, rib chords, trailing edges, cargo doors, rotor blades, and pressure vessels [1]. Processing parameters such as resin viscosity, injection pressure, inlet/outlet location, reinforcement permeability, cure time, and cure temperature all have a great effect on the composite. For the reliability and safety of these components, it is vital to understand and control the manufacturing process thoroughly.

A number of processing techniques exist for composite materials. RTM is a particularly attractive technique due to its repeatability, chemical containment, and ability to achieve high fiber volume fraction in an automated manner. With RTM, a fiber preform is placed in a closed mold before the resin is injected and allowed to cure. The two most critical processing steps are the resin injection and cure stages. During the resin injection stage, regions of reinforcement that are not saturated with resin (known as dry spots) may form. These dry spots severely reduce the mechanical properties of the composite and may be present in locations that are not visible to the human eye and may be unnoticed. The temperature and time the composite is cured for also has a significant influence. If the part is removed from the mold before adequately cured, it may get distorted. On the other hand, leaving the part in the mold too long results in loss of mold usage as well. The time the composite is held at a specific temperature affects the polymerization rate of the resin and in turn its mechanical properties. Therefore, the optimum temperature and duration of cure are important processing parameters. The term cure refers to the chemical reactions that take place after the resin and hardener are combined, resulting in the formation of a polymerized and cross-linked structure. The cure cycle of a resin system consists of two main stages: gelation and vitrification. Gelation refers to the transition from a viscous liquid to an elastic gel. Vitrification refers to the change from a rubbery state to a solid state. Cure monitoring consists of monitoring changes in various physical or chemical properties of the resin during these stages. There has been a substantial amount of work devoted to the development of techniques for characterizing the cure [2].

Various forms of cure sensors have been developed based on conductometric [3–7], dielectrometric [8–11], and ultrasonic [12,13] techniques. A brief summary of the current sensor technologies for flow and cure monitoring in composite manufacturing processes is provided in Ref. [2]. These approaches have not received significant acceptance as cure sensors for integration in manufacturing processes. Researchers have looked toward fiber optic sensors to find alternatives. These sensors are based on the absorption, reflection, refraction, or emission of light. A wide variety of fiber optic sensor based methodologies have been investigated for monitoring the cure cycle of resins such as those based on transmission spectroscopy [14], evanescent wave spectroscopy

Contributed by the Manufacturing Engineering Division of ASME for publication in the JOURNAL OF MANUFACTURING SCIENCE AND ENGINEERING. Manuscript received March 29, 2011; final manuscript received March 20, 2012; published online xx xx, xxxx. Assoc. Editor: Robert Gao.

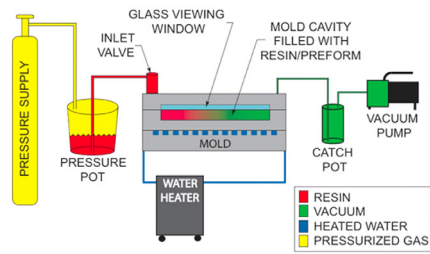


Fig. 1 Schematic of RTM process (left) and the lab apparatus including optical equipment (right)

[15,16], refractive index monitoring [17–19], long period gratings and tilted fiber Bragg gratings [20], and Fresnel based refractometry [21–23]. Fiber optic sensors are less intrusive and can be embedded within composite structures. They have the ability to be multiplexed, which enables sensing of spatially distributed quantities on a single optical fiber. A summary of fiber optic sensors for monitoring the cure of polymers is provided in Ref. [24].

FBGs have attracted attention within the last decade due to their lightweight, small size (they are contained within the core of the optical fiber), and self-referencing nature [1,25,26]. Embedded FBGs can be used for three distinct purposes during the life of a resin transfer molded part. An array of multiplexed FBGs in a mold can monitor the injection process and ensure that the mold is completely saturated with resin [27]. It can be used to monitor the cure throughout the part [28–30] and once in service can be used to monitor the structural integrity of the part.

Another type of sensor used for process monitoring is an EF sensor. These sensors consist of a small section of optical fiber that is etched to remove some of the cladding. When this etched region is immersed in resin, the optical power transmitted through the fiber changes allowing the sensor to detect fluid. Etched sensors can also be used for cure monitoring. The refractive index of resin changes during curing affecting the amount of light that is transmitted through the sensor. During the service of a composite structure, etched sensors may also be used for structural health monitoring. If there is a disruption or weakening in the transmitted light signal when the composite is under loading, one can conclude that the sensor location is either excessively loaded or cracked.

FRR sensors are similar to EF sensors as they are based on a change in refractive index of the surrounding medium. These sensors consist of an optical fiber with a cleaved end. Light is launched toward this end and the reflected light, which is a function of the refractive index of the medium it is immersed in, is monitored. They are well suited for cure monitoring.

2 Background

Resin transfer molding is a subcategory of liquid composite molding. The RTM process involves loading a two sided, closed mold with a fiber perform (commonly carbon or glass fiber), closing and clamping the mold, injecting resin, and allowing it to cure. The RTM apparatus built within the scope of this research has a glass viewing window to visually monitor resin flow during injection. Figure 1 shows a schematic of the RTM process and the RTM system. It has one inlet port, two outlet ports, and produces a 305 mm × 610 mm × 3 mm panel. In all experiments presented, 800 g/m² biaxial glass fiber reinforcement (X 800 E05) manufactured by Metyx and ARALDITE LY 564 resin with XB 3403 hardener are used.

The ingress/egress of fiber optics is one of the important issues for embedding fiber optic sensors into composite structures in a

repeatable and consistent manner because the optical fiber is fragile at the ingress/egress location and does not tolerate a sharp bending radius. Toward this end, in our early works [31], a novel through thickness ingress/egress method has been developed, which can overcome the limitations of the in-plane ingress/egress method and be applicable to closed mold processes such as RTM. To protect the fiber with minimal disturbance to the composite material, a thin hypodermic tube is placed around the fiber. This protects the fiber through the radius of the bend as well as reinforces the fiber at the ingress/egress point once the part is removed from the mold. A tapered silicone stopper was used to seal around the hypodermic tube.

An FBG is a segment of a single mode optical fiber core with a periodically modulated refractive index along the axis of the fiber. It acts as an optical filter by reflecting a narrow wavelength spectrum back while transmitting others as described in Fig. 2.

The periodic modulation of the refractive index at the grating location scatters light; out of phase scattered waves form destructive interference that cancels out while in phase waves add up constructively forming a reflected spectrum. The center wavelength of this spectrum is referred to as the Bragg wavelength. The Bragg wavelength satisfies the Bragg condition as

$$\lambda_B = 2n_{eff}\Lambda \quad (1)$$

where λ_B is the Bragg wavelength, n_{eff} is the effective refractive index of the fiber, and Λ is the pitch of the gratings. The spacing of the refractive index modulation and refractive index are a function of strain and temperature, and any change in these will cause the Bragg wavelength to shift.

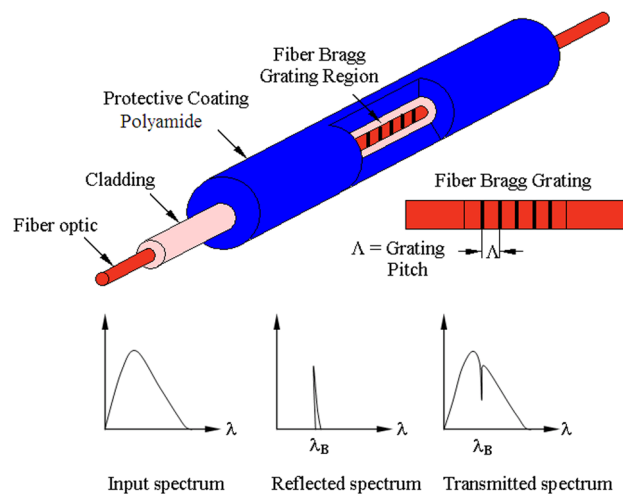


Fig. 2 Schematic of an FBG sensor

189 In this study, FBGs have been used for both cure and flow monitoring.
 190 Injecting room temperature resin into a heated RTM mold
 191 allows for resin flow front monitoring based on the temperature
 192 differential between FBG and resin. Since the curing process is
 193 exothermic and residual stresses accumulate during cure, monitoring
 194 the shift of the Bragg wavelength allows for detection of the
 195 gelation and vitrification behavior of the composites.

196 The second type of optical sensor used in this work is an EF
 197 sensor, which can also monitor the resin flow and cure. This sensor
 198 operates in the transmission mode such that a light source
 199 launches light into one end of the fiber and an optical spectrum
 200 analyzer (OSA) measures the light intensity at the other end. An EF
 201 sensor is a section of the optical fiber roughly 3–4 mm long that is
 202 etched to reduce the cladding thickness. The details of the preparation
 203 of an EF sensor can be found in Ref. [31]. In this etched
 204 area, the external medium essentially becomes a part of the fiber
 205 waveguide. If the refractive index of the external medium is
 206 smaller than the core of the fiber, there will only be a small perturbation
 207 to the fiber mode, and a low loss single mode will still be supported.
 208 On the other hand, if the refractive index of the external medium is
 209 larger than that of the fiber, the propagating mode will be a leaky mode.
 210 This leaky mode can be viewed as a decaying mode due to optical leakage
 211 into the higher refractive index medium. Since the refractive index of the
 212 resin is higher than the fiber core, there will be a loss when the resin
 213 reaches the etched area. The etched fiber can be modeled using the
 214 technique described in Ref. [32]. Since the refractive index of resin
 215 changes during cure, EF sensors can be used to monitor the cure.

216 FRR sensors can also monitor cure based on the change in refractive
 217 index of the resin [33]. The FRR sensor consists of a single mode
 218 optical fiber that is cleaved at its free end. The FRR optic circuit
 219 consists of a light source, optical circulator, and OSA. The uncleft
 220 end of the probe is coupled to the second port of an optical circulator
 221 with the first and third ports connected to a light source and OSA,
 222 respectively. Assuming that the free end of the fiber is cleaved such
 223 that the light is at a near-normal incidence to the interface, the
 224 reflection coefficient R is given by the Fresnel equation as
 225
 226

$$R = \frac{P_r^s}{P_i} = \frac{(n_s - n_f)^2}{(n_s + n_f)^2} \quad (2)$$

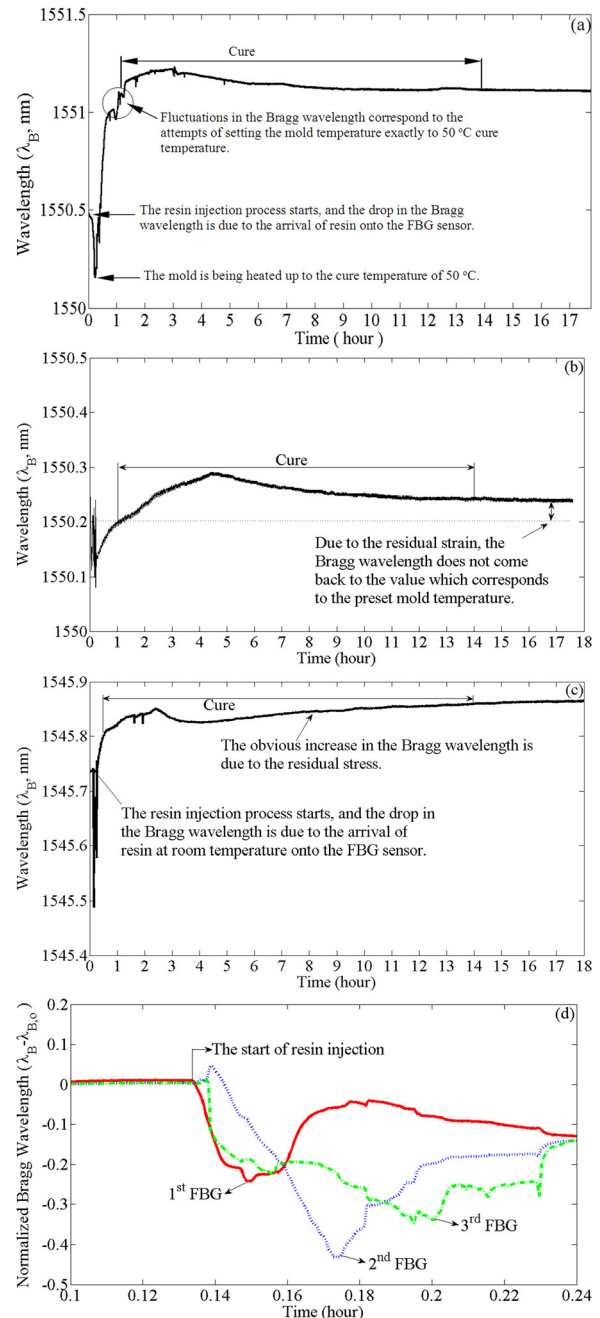
227 where P_r^s and P_i are powers of the reflected light from the sample
 228 ($s = a$ for air, $s = l$ for resin) and the incident light, respectively,
 229 and n_s and n_f are the refractive index of the sample and the fiber,
 230 respectively. The refractive index of resin can be determined by
 231 measuring reflected powers P_r^a and P_r^l when the FRR sensor is in
 232 air and resin. Dividing the Fresnel relation for air and resin results
 233 in

$$\frac{P_r^l}{P_r^a} = \frac{(n_l - n_f)^2 (n_a + n_f)^2}{(n_l + n_f)^2 (n_a - n_f)^2} \quad (3)$$

234 Taking the refractive index of air and fiber as 1 and 1.45, respectively,
 235 the refractive index of the sample can be determined. Experiments
 236 show that at room temperature, the refractive index of resin and
 237 hardener alone are 1.54 and 1.48 respectively, while the refractive
 238 index of the resin and hardener mixture is 1.52 before cure. It is
 239 to be noted that since we are interested in the tendency of refractive
 240 index change due to the temperature variation and cross-linking
 241 polymerization, in Sec. 3.3, measurements are given in terms of
 242 reflected power not in terms of real values of the refractive index
 243 of the curing resin system.

244 3 Experimental Implementations and Results

245 **3.1 Flow and Cure Monitoring With FBG Sensors.** Several
 246 experiments for cure monitoring of RTM'd composite plates with
 247 FBG sensors were performed. During the experiments, the FBG
 248 sensors were monitored by a Micron Optics interrogator,



249 **Fig. 3 Bragg wavelength versus time for cure and flow monitoring with FBGs: (a) Experiment-1, (b) experiment-2, (c) experiment-3 for cure monitoring, and (d) experiment-3 for flow monitoring with three FBG sensors**

250 model sm230. The results of these experiments are summarized in
 251 Fig. 3.

252 In all experiments, nine layers of biaxial glass fiber reinforcement
 253 were used. FBG sensors were positioned between the fourth and fifth
 254 ply for the first two experiments and between the seventh and eighth
 255 ply for the third experiment. The first two experiments utilized a
 256 single FBG while the third one employed three FBGs multiplexed on
 257 a single fiber.

258 In the first experiment, room temperature resin was injected into
 259 the mold at 30 °C. The first sudden drop in the Bragg wavelength in
 260 Fig. 3(a) is due to the arrival of resin at the FBG sensor. Subsequently,
 261 the mold was heated to cure temperature of 50 °C resulting in a shift
 262 of the Bragg wavelength. The fluctuations in Fig. 3(a) correspond to a
 263 region where the temperature of the

263 mold was set to the cure temperature. Since the cure process is
 264 exothermic, the released heat further shifts the Bragg wavelength.
 265 As the strength of the exothermic process diminishes, the water-
 266 cooling system in the RTM mold attempts to bring the tempera-
 267 ture of the mold to the preset cure temperature, which is observed
 268 in all relevant subfigures of Fig. 3. Given the presence of residual
 269 stress buildup in the composite (due to various effects such as
 270 thermal gradients, shrinkage, and differentials in thermal expan-
 271 sion coefficients), the Bragg wavelength does not return to its
 272 original value. This case is much more obvious in Fig. 3(c)
 273 because the FBG sensor was positioned on the seventh ply. The
 274 closer the sensor is to the neutral axis, the less strain effect it expe-
 275 riences. As the polymerization reaction nears completion, the shift
 276 in Bragg wavelength ceases. The region marked with two vertical
 277 lines corresponds to the curing of the epoxy system.

278 In the second and third experiments, the resin is injected into a
 279 mold heated to 50 °C. A drop in the wavelength is observed upon
 280 the arrival of the resin to the FBG sensor. As the resin gradually
 281 reaches the cure temperature, the Bragg wavelength of the FBG
 282 sensors increases. The horizontal line in Fig. 3(b) indicates the
 283 preset mold temperature. Regardless of experimental conditions,
 284 the tendency of wavelength versus processing time is identical,
 285 implying the effectiveness of FBG sensors for cure monitoring for
 286 RTM composites.

287 Flow monitoring is achieved with three FBG sensors multi-
 288 plexed on a fiber optic cable. The first FBG was positioned near
 289 the inlet, the second near the middle of the mold, and the last
 290 near the outlet. Figure 3(d) indicates the flow front monitoring
 291 with FBG sensors. To be able to present shifts in the Bragg
 292 wavelengths of three FBG sensors on the same graph, Bragg
 293 wavelength λ_B values recorded during the resin injection process
 294 are subtracted from those values $\lambda_{B,0}$ recorded before the injec-
 295 tion. The sudden decreases in the normalized Bragg wavelength
 296 values ($\lambda_B - \lambda_{B,0}$) indicate the time that the epoxy reaches the
 297 sensor.

298 **3.2 Flow and Cure Monitoring With EF Sensors.** To
 299 investigate the ability and effectiveness of EF sensors for resin
 300 flow and cure monitoring in an RTM system, experiments were
 301 conducted with three etched sensors multiplexed on a length of
 302 bare optical fiber located between the fifth and sixth plies in the
 303 RTM mold. The sensors were monitored during the resin injection
 304 process to detect the presence of resin. The first etched sensor is
 305 located near the mold inlet, the second in the middle of the mold,
 306 and the last near the outlet. In the same experiment, an FBG sensor
 307 was placed between the same fiber layers in the middle of the
 308 mold (see Fig. 3(a)).

309 Figures 4(b) and 4(c) indicate the segments of the entire RTM
 310 process monitored with etched fiber sensors as shown in Fig. 4(a).
 311 Recall that the RTM mold in the experimental setup has a glass
 312 window for visual flow monitoring, which is situated on the bot-
 313 tom surface of the top lid of the mold and fixed by means of a
 314 room temperature vulcanizing aerospace grade silicone. Due to
 315 the flexibility of the silicone, when the mold is under vacuum the
 316 glass window is drawn toward the mold cavity exerting more
 317 force on the ingress and egress points of the EF sensors causing a
 318 significant drop in the intensity of light passing through. This situ-
 319 ation corresponds to the first drop in transmitted light as shown
 320 in Fig. 4(b). At this point, the vacuum was released to reduce the
 321 stress on the sensors. As a result, the transmitted light intensity
 322 has returned back to its initial level. It should be noted that when
 323 the mold is closed, the intensity of the transmitted light drops due
 324 to the clamping force at the ingress and egress points. Upon resin
 325 injection, the clamping force that causes a drop in transmitted
 326 light intensity is counterbalanced by the positive pressure of the
 327 resin resulting in a slight increase in transmitted light intensity.

328 Once the resin reaches the first EF sensor, the transmitted light
 329 intensity drops. As the injection proceeds, the clamping force is
 330 further balanced by the pressure of the resin, and the curvature of

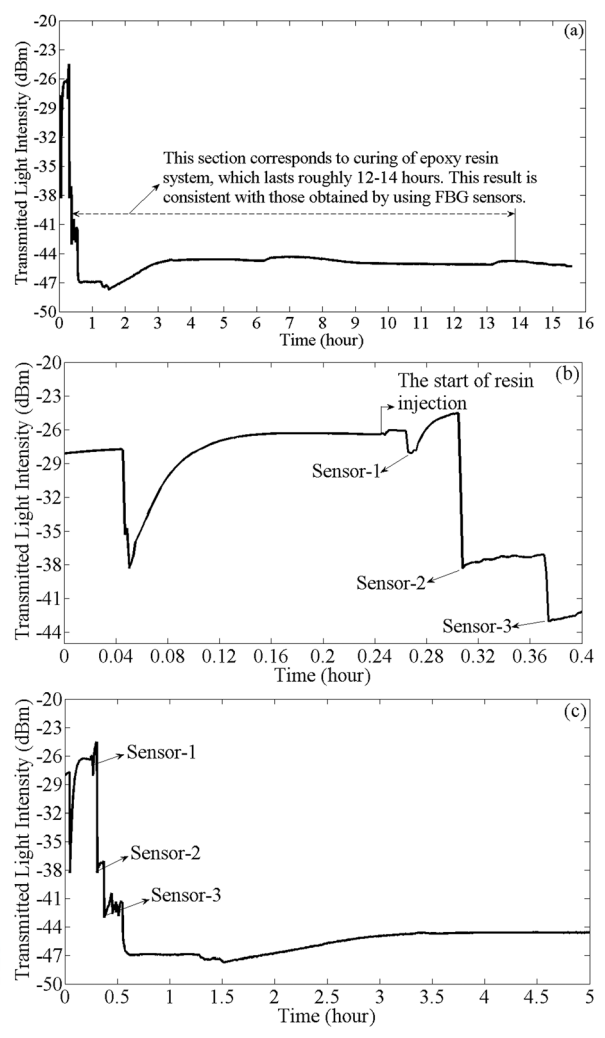


Fig. 4 (a) Complete history of the RTM process; (b) and (c) close-up view for a segment of a light intensity drop versus processing time curve

the optical fibers at the ingress and egress points reduces. This
 appears as a gradual increase in the transmitted light intensity.
 When the resin reaches the second and third sensors, the transmit-
 ted light intensity drops, then starts increasing due to the counter-
 acting pressure effect of the resin. Figure 4(b) clearly shows that it
 is possible to record the flow process entirely in terms of resin ar-
 rival. After completing the injection process at room temperature,
 the cure cycle is induced by bringing the mold to cure tempera-
 ture. As concluded from Fig. 4(a), the manufacturing process was
 successfully monitored until completion.

3.3 Cure Monitoring With FRR Sensors. To show the
 ability of FRR sensors for cure monitoring and also demonstrate
 that it is a repeatable and reliable process, several hot plate experi-
 ments were conducted. The results of two experiments are sum-
 marized in Fig. 5 as reflected power versus process time. After
 immersing an FRR sensor into a resin-hardener mixture in an
 aluminum container, the mixture was heated to roughly 50 °C on a
 hot plate. Temperature data were collected concurrently with a
 pyrometer in the experiment shown in Fig. 5(b). In accordance
 with the Fresnel relation, when the FRR sensor is dipped into the
 resin-hardener mixture at room temperature, the reflected power
 drops significantly from that measured when in air to the
 value shown in Figs. 5(a) and 5(b) at time zero since $n_1 \gg n_a$.
 The reflected power gradually decreases when heating the

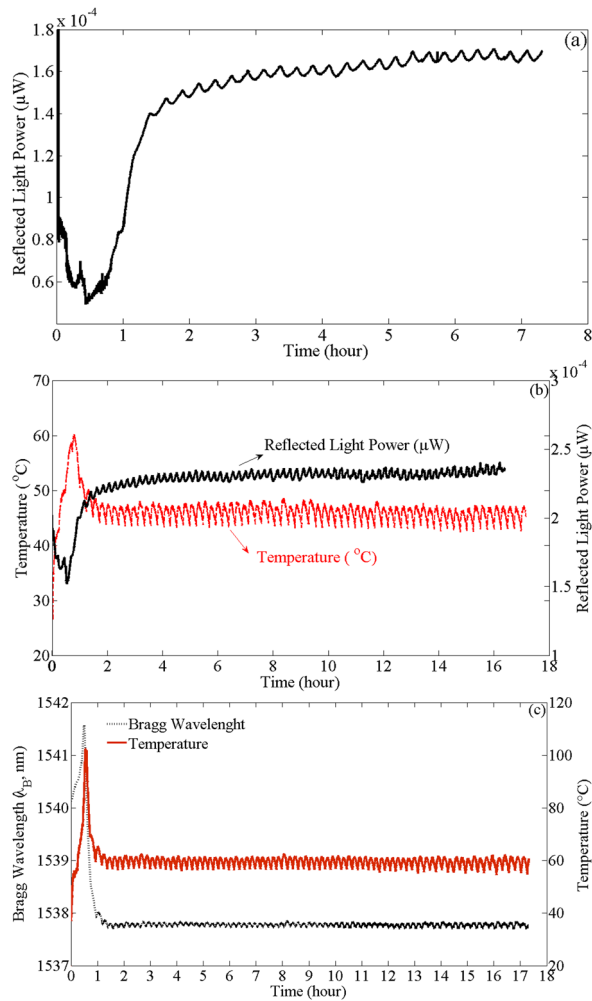


Fig. 5 (a) and (b) Reflected light power and temperature versus time; (c) temperature and Bragg wavelength variations as a function of time

355 mixture. This drop is due to the temperature dependent decrease
356 in refractive index of the resin system. The temperature of the
357 resin system continues to increase due to the exothermic heating
358 causing a further drop in reflected power.

359 Subsequent to the decrease in the reflected power, there is a
360 rapid increase in the reflected power when the resin system begins
361 to gel. The sudden increase of the reflected power corresponds to
362 the initiation of the exothermic cure reaction. As the exothermic
363 reaction loses its strength, the temperature of the resin system
364 drops down to the preset temperature. The point when undulations
365 begin is considered the time the mixture has nearly reached the
366 preset temperature. The undulations are due to the on-off nature
367 of the temperature controller of the hot plate. As the cure process
368 continues, the cross-link density increases causing an increase in
369 the refractive index resulting in an increase in the reflected power.

370 The point where the plot reaches steady state is considered to
371 be a nearly complete cure. One can see that the steady state has
372 been reached after roughly 12–14 h, which is in agreement with
373 the cure time obtained with both FBG and EF sensors. In one of
374 the experiments, the temperature variation during cure was moni-
375 tored with a pyrometer and an FBG sensor to validate the occur-
376 rence of the sudden rise in temperature of the resin system due to
377 the exothermic curing reaction as shown in Fig. 5(c).

378 **3.4 Cure Sensor Validation.** To validate the cure monitor-
379 ing abilities of the sensors investigated, polymer extraction
380 experiments were performed to determine the degree of cure as a

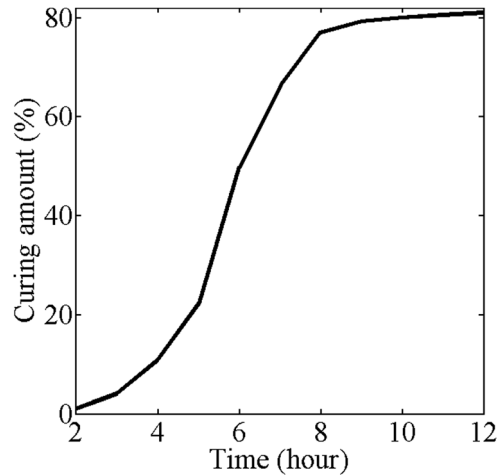


Fig. 6 The degree of cure as a function of time

function of time. Several samples of the epoxy system were pre- 381
pared and cast in a Teflon mold. The samples were cured at 50 °C 382
for various durations between 2 and 12 h. After the sample was 383
removed from the mold, its mass was measured and placed in a 384
solution of tetrahydrofuran solvent. The solvent removes the 385
uncured epoxy resin over a period of 24 h leaving the fully cured 386
part. After removing the remaining sample from the solution, it 387
was dried inside an oven and the final mass was measured to 388
determine the percentage of cure. The results of the extraction 389
experiments are summarized in Fig. 6. It can be concluded that 390
this specific epoxy resin system nearly completes its cure period 391
in approximately 12 h which is consistent with the data obtained 392
with the optical sensors. 393

4 Conclusion 394

Fiber optic sensors possess several advantages such as flow, 395
cure, and structural health monitoring sensors in composite struc- 396
tures because of their small size, light weight, immunity to elec- 397
tromagnetic field interference, multiplexing capability, and long 398
service life. They can be embedded in a structure and act as a part 399
of the system without changing the mechanical characteristics. 400
Both FBG and etched fiber sensors provide data about the resin 401
flow front ensuring that the mold is fully saturated. With the help 402
of a network of sensors embedded throughout the mold, the opera- 403
tor can determine where the resin has reached. Both types of sen- 404
sors can subsequently be used for determining the degree of cure. 405

In this research, systematic experimental studies for process 406
monitoring (cure and flow monitoring) of RTM'd composite 407
materials are presented. The ability of FBG and etched fiber sen- 408
sors for resin flow front monitoring and cure monitoring in an 409
operational RTM process has been demonstrated along with the 410
cure monitoring ability of a Fresnel probe. Cure monitoring 411
results were compared with polymer extraction experiments 412
showing good agreement. EFS and FRR sensors can be used as a 413
simple, cost-effective alternative to FBG sensors for process moni- 414
toring in composite materials manufacturing. Additionally, these 415
sensors are not sensitive to any residual stress in the curing 416
composites unlike FBG sensors. The experimental results show the 417
potential for three types of optical sensors to provide real time in- 418
formation during the processing of RTM composite manufactur- 419
ing systems. 420

Acknowledgment 421

The funding provided by the Scientific and Technological 422
Research Council of Turkey (TUBITAK) for the project 423
108M229 is gratefully acknowledged. 424

References

[1] Measures, R. M., 2001, *Structural Monitoring With Fiber Optic Technology*, Academic Press, New York. 425

[2] Yenilmez, B., and Sozer, E. M., 2009, "A Grid of Dielectric Sensors to Monitor Mold Filling and Resin Cure in Resin Transfer Molding," *Composites, Part A*, **40**, pp. 476–489. 426 427

[3] Lawrence, J. M., Hsiao, K. T., Don, R. C., Simacek, P., Estrada, G., Sozer, E. M., Stadtfeld, H. C., and Advani, S. G., 2002, "An Approach to Couple Mold Design and On-Line Control to Manufacture Complex Composite Parts by Resin Transfer Molding," *Compos. A Appl. Sci. Manuf.*, **33**(7), pp. 981–990. 428 429 430

[4] Danisman, M., Tuncol, G., Kaynar, A., and Sozer, E. M., 2007, "Monitoring of Resin Flow in the Resin Transfer Molding (RTM) Process Using Point-Voltage Sensors," *Compos. Sci. Technol.*, **67**(3–4), pp. 367–379. 431 432

[5] Barooah, P., Berker, B., and Sun, J. Q., 1999, "Linear Sensors for Liquid Injection Molding of Advanced Composite Materials," *J. Mater. Process. Manuf. Sci.*, **6**(3), pp. 169–184. 433 434

[6] Fink, B. K., Walsh, S. M., DeSchepper, D. C., Gillespie, J. W., Jr., McCullough, R. L., Don, R. C., and Waibel, B. J., 1995, "Advances in Resin Transfer Molding Flow Monitoring using SMART Weave Sensors," *Proceedings of ASME, International Mechanical Engineering Congress and Exposition*, San Francisco, CA, **69**(II), pp. 999–1015. 435 436 437 438

[7] Bradley, J. E., Diaz-Perez, J., Gillespie, J. W., Jr., and Fink, B. K., 1998, "On-Line Process Monitoring and Analysis of Thick-Section Composite Parts Utilizing SMARTweave In Situ Sensing Technology," *Proceedings of International SAMPE Symposium and Exhibition*, pp. 254–267. 439 440 441

[8] McIlhagger, A., Brown, D., and Hill, B., 2000, "The Development of a Dielectric System for the On-Line Cure Monitoring of the Resin Transfer Molding Process," *Compos. A, Appl. Sci. Manuf.*, **31**(12), pp. 1373–1381. 442 443

[9] Hegg, M. C., Ogale, A., Mescher, A., Mamishev, A. V., and Minaie, B., 2005, "Remote Monitoring of Resin Transfer Molding Processes by Distributed Dielectric Sensors," *J. Compos. Mater.*, **39**(17). 444 445

[10] Kim, H. G., and Lee, D. G., 2002, "Dielectric Cure Monitoring for Glass/Polyester Prepreg Composites," *Compos. Struct.*, **57**(1–4), pp. 91–99. 446

[11] Bang, K. G., Kwon, J. W., Lee, D. G., and Lee, J. W., 2001, "Measurement of the Degree of Cure of Glass Fiber Epoxy Composites Using Dielectrometry," *J. Mater. Process. Technol.*, **113**(1–3), pp. 209–214. 447 448

[12] Rath, M., Doring, J., Stark, W., and Hinrichsen, G., 2000, "Process Monitoring of Moulding Compounds by Ultrasonic Measurements in a Compression Mould," *NDT E Int.*, **33**(2), pp. 123–130. 449 450

[13] Schmachtenberg, E., zur Heide Schulte, J., and Topker, J., 2005, "Application of Ultrasonics for the Process Control of Resin Transfer Moulding (RTM)," *Polym. Test.*, **24**(3), pp. 330–308. 451 452

[14] Powell, G. R., Crosby, P. A., Waters, D. N., France, C. M., Spooncer, R. C., and Fernandok, G. F., 1998, "In-Situ Cure Monitoring Using Optical Fibre Sensors—A Comparative Study," *Smart Mater. Struct.*, **7**, pp. 557–568. 453 454

[15] Woerdeman, D. L., and Parnas, R. S., 2001, "Model of a Fiber-Optic Evanescent Wave Fluorescence Sensor," *Appl. Spectrosc.*, **55**, pp. 331–317. 455

[16] Woerdeman, D. L., Spoerre, J. K., Flynn, K. M., and Parnas, R. S., 1997, "Cure Monitoring of the Liquid Composite Molding Process Using Fibre Optics Sensors," *Polym. Compos.*, **18**, pp. 133–150. 456 457

[17] Afromowitz, M. A., 1988, "Fiber Optic Polymer Cure Sensor," *J. Lightwave Technol.*, **8**, pp. 1591–1594. 458

[18] Lam, K. Y., and Afromowitz, M. A., 1995, "Fiber Optic Epoxy Composite Cure Sensor: I. Dependence of Refractive-Index of an Autocatalytic Reaction Epoxy System at 850 nm on Temperature and Extent of Cure," *Appl. Opt.*, **34**, pp. 5635–5638. 459 460 461

[19] Lam, K. Y., and Afromowitz, M. A., 1995, "Fiber Optic Epoxy Composite Cure Sensor: II. Performance-Characteristics," *Appl. Opt.*, **34**, pp. 5638–5644. 462

[20] Buggy, S. J., Chehura, E., James, S. W., and Tatam, R. P., 2007, "Optical Fibre Grating Refractometers for Resin Cure Monitoring," *J. Opt. A Pure Appl. Opt.*, **9**(6), p. S60. 463 464

[21] Liu, Y. M., Ganesh, C., Steele, J. P. H., and Jones, J. E., 1997, "Fiber Optic Sensor Development for Real-Time In-Situ Epoxy Cure Monitoring," *J. Compos. Mater.*, **31**, pp. 87–102. 465 466

[22] Chailleux, E., Salvia, M., Jaffrezic-Renault, N., Matejee, V., and Kasik, I., 2001, "In Situ Study of the Epoxy Cure Process Using a Fibre-Optic Sensor," *Smart Mater. Struct.*, **10**, pp. 194–202. 467 468

[23] Cusano, A., Breglio, G., Giordano, M., Calabro, A., Cutolo, A., and Nicolais, L., 2001, "Optoelectronic Characterization of the Curing Process of Thermoset-Based Composites," *J. Opt. A: Pure Appl. Opt.*, **3**, pp. 126–130. 469 470

[24] Li, C., Cao, M., Wang, R., Wang, Z., Qiao, Y., Wan, L., Tian, Q., Liu, H., Zhang, D., Liang, T., and Tang, C., 2003, "Fiber-Optic Composite Cure Sensor: Monitoring the Curing Process of Composite Material Based on Intensity Modulation," *Compos. Sci. Technol.*, **63**, pp. 1749–1758. 471 472 473

[25] Kashyap, R., 2010, "Principles of Optical Fiber Grating Sensors," *Fiber Bragg Gratings*, 2nd ed., Academic Press, San Diego, pp. 441–502. 474

[26] Guemes, J. A., and Menéndez, J. M., 2002, "Response of Bragg Grating Fiber-Optic Sensors When Embedded in Composite Laminates," *Compos. Sci. Technol.*, **62**, pp. 959–966. 475 476

[27] Dunkers, J. P., Lenhart, J. L., Kueh, S. R., Van Zanten, J. H., Advani, S. G., and Parnas, R. S., 2001, "Fiber Optic Flow and Cure Sensing for Liquid Composite Molding," *Opt. Lasers Eng.*, **35**(2), pp. 91–104. 477 478

[28] Dweynter-Marty, V., Ferdinand, P., Bocherens, E., Carbone, R., Beranger, H., Bourasseau, S., Dupont, M., and Balageas, D., 1998, "Embedded Fiber Bragg Grating Sensors for Industrial Composite Cure Monitoring," *J. Intell. Mater. Syst. Struct.*, **9**, pp. 785–787. 479 480 481

[29] Murukeshan, V. M., Chan, P. Y., Ong, L. S., and Seah, L. K., 2000, "Cure Monitoring of Smart Composites Using Fiber Bragg Grating Based Embedded Sensors," *Sens. Actuators. A Phys.*, **79**, pp. 153–161. 482 483

[30] Jung, K., and Kang, T. J., 2007, "Cure Monitoring and Internal Strain Measurement of 3-D Hybrid Braided Composites Using Fiber Bragg Grating Sensor," *J. Compos. Mater.*, **41**(12), pp. 1499–1519. 484 485

[31] Keulen, C., Yildiz, M., and Suleman, A., 2011, "Multiplexed FBG and Etched Fiber Sensors for Process and Health Monitoring of 2- & 3-D RTM Components," *J. Reinf. Plast. Compos.*, **30**(12), pp. 1055–1064. 486 487

[32] Sharma, A., Kompella, J., and Mishra, P. K., 1990, "Analysis of Fiber Directional Couplers and Coupler Half-Blocks Using a New Simple Model For Single-Mode Fibers," *J. Lightwave Technol.*, **8**(2), pp. 143–151. 488 489

[33] Kim, C. B., and Su, C. B., 2004, "Measurement of the Refractive Index of Liquids at 1.3 and 1.5 Micron Using a Fibre Optic Fresnel Ratio Meter," *Meas. Sci. Technol.*, **15**, pp. 1683–1686. 490 491

AQ5

AQ2

AQ3

AQ4

Appendix C

**Damage Detection of Composite Plates by Lamb Wave Ultrasonic Tomography
with a Sparse Hexagonal Network Using Damage Progression Trends**

Damage detection of composite plates by Lamb wave ultrasonic tomography with a sparse hexagonal network using damage progression trends

C.J.Keulen^a, M.Yildiz^b, A.Suleman^{a,*}

^a*University of Victoria, Department of Mechanical Engineering,
Victoria, B.C., V8W 3P6, Canada*

^b*Sabanci University, Faculty of Engineering and Natural Sciences,
Orhanli-Tuzla, 34956 Istanbul, Turkey*

Abstract

Lamb wave based structural health monitoring shows a lot of potential for damage detection of composite structures however, currently there is not agreed upon optimal network arrangement or detection algorithm. The objective of this research is to develop a sparse network that can be expanded to detect damage over a large area. To achieve this, a novel technique based on damage progression history has been developed. This technique gives an amplification factor to data along actuator-sensor paths that show a steady reduction in transmitted power as induced damage progresses and is implemented with the reconstruction algorithm for probabilistic inspection of damage (RAPID) technique. Two damage metrics are used with the algorithm and a comparison is made to the more commonly used signal difference coefficient (SDC) metric. Best case results show that damage is detected within 12mm. The algorithm is also run on a more sparse network with no damage detection therefore indicating that the selected arrangement is the most sparse arrangement with this configuration.

Keywords: SHM, damage detection, Lamb wave, tomography, composite material

*Corresponding author

Email addresses: ckeulen@uvic.ca (C.J.Keulen), meyildiz@sabanciuniv.com (M.Yildiz), suleman@uvic.ca (A.Suleman)

1. Introduction

To achieve lighter aerospace structures, damage is allowed to exist during operation as long as it is within safe, predetermined specifications; aircraft structures are designed according to a damage tolerant philosophy. In more recent years composite materials are being used to build aerospace structures because they are lightweight, stiff and have excellent fatigue and corrosion resistance. The down side to composites however, lies in their damage mechanisms. Composites may fail or become damaged in a number of ways that are very different from traditional metallic materials. Defects may arise during manufacture due to voids/porosity, ply misalignment or inclusion of foreign objects that show no evidence to the naked eye. Composites suffer from low velocity impacts that can damage the internal structure of a laminate while leaving no visible evidence on the surface.

Maintenance and inspection of aircraft is of the utmost importance for safe and efficient operation. Aircraft structures operate in harsh conditions sustaining high loads, fatigue cycles and extreme temperature differentials. Failure of these structures is not acceptable due to the possibility of loss of life and assets. To ensure aircraft structures are in safe operational condition, costly inspection involving aircraft down time and often disassembly of major components is routinely performed. The cost of inspection is about 30% of the total cost of acquiring and operating composite structures [1]. Currently, damage detection is performed with techniques referred to as non-destructive testing (NDT) or non-destructive inspection (NDI) to locate and quantify damage.

To reduce operational cost and improve reliability and performance, a common goal of researchers, designers and manufacturers is to develop a real time inspection system that is permanently installed or embedded within the structure. This technique is commonly referred to as structural health monitoring (SMH) [2, 3]. Such systems typically consist of a network of transducers that are used to sense physical parameters that indicate the presence of damage with an interrogation technique or algorithm.

In 1917, Horace Lamb published his classic analysis and description of acoustic waves, which included the first consideration of Lamb waves [4]. In 1961, Worlton, D.C. [5] proposed the use of Lamb waves for damage detection and a new NDE potential emerged. In 1962, Frederik, C.L. et al [6] conducted the first experimental study. Beginning in the 1990s Hutchins, D.A. et al [7, 8, 9] and Nagata, Y. et al [10] applied Lamb waves to NDE

using medical imaging and seismic tomography techniques to both metallic and composite materials. Their systems utilized pairs of transducers that were positioned across the material at various locations in order to obtain a dense collection of pitch-catch signals in order to reconstruct a tomogram. While the techniques produced reasonable results the methods were time consuming, requiring a lot of repositioning of the transducers and in some cases requiring the specimen to be placed in a water bath. Prasad, S.M. et al [11] implemented an SHM system for composites using surface bonded piezoelectric transducers. Since the transducers were permanently bonded in place the system could be operated in real time without any repositioning. Gao, H. et al [12] introduced the reconstruction algorithm for probabilistic inspection of damage (RAPID). Michaels, J.E. [13] later investigated the application of tomography algorithms to sparse networks.

Other research efforts were made to use the Lamb wave mode propagation characteristics in order to detect damage; specifically the attenuation and arrival time of the first two wave modes. In 1993 Guo, N. et al [14] studied the interaction of Lamb waves with delaminations in composite materials both numerically and experimentally. Keilers, C.H. et al [15] later proposed a built-in damage detection system using an array of piezoelectric transducers. Giurgiutiu, V. et al [16] discussed the pulse-echo analysis technique and subtracting baseline data from damaged data to detect damage.

This paper presents the details and results of a study on the implementation of a sparse piezoelectric transducer network for damage detection in composite materials. The objective of this research is to develop a sparse network that can be expanded to detect damage over a large area. To achieve this, a novel technique based on damage progression history has been developed.

2. Theory and Implementation

Lamb waves are elastic, guided waves that propagate parallel to the surface in thin structures with free boundaries. Plates are the best example however, Lamb waves can also propagate in structures with a shallow curvature. The most advantageous characteristics of these waves are their susceptibility to interferences caused by damages or boundaries (the features of interest) and low amplitude loss. To implement a Lamb wave based damage detection technique some important properties must be determined. When Lamb waves propagate they travel in one of two possible ways with respect to

the plate's mid plane. If the motion is symmetric about the mid-plane (the peaks and troughs of the waves are in phase) then it is a symmetric mode and if the motion is not symmetric (the peaks and troughs are 180° out of phase) it is an anti-symmetric mode. An infinite number of modes exist, each mode is referred to as an A mode or S mode if it is anti-symmetric or symmetric respectively, with a subscript indicating its order. For example the lowest order/frequency symmetric mode is referred to as an S_0 mode while the second lowest order/frequency symmetric mode is referred to as an A_1 mode. Each mode exists at a different frequency depending on the properties of the material. At lower frequency-thickness values less modes exist. It is advantageous to operate in a frequency-thickness range where only the S_0 and A_0 modes exist. This is generally below $1.5MHz\text{-}mm$.

2.1. Implementation

To employ Lamb waves for damage detection, a system to send and receive Lamb waves must be developed and a number of parameters must be selected to tune the system such as the transducer type, size and arrangement, actuation signal and data acquisition.

Piezoelectric transducers are commonly used in SHM systems. They are inherently simple devices consisting of simply a piezoelectric material with two conductive surfaces. When a voltage is applied across the surfaces the material expands or contracts (depending on polarity) proportional to the magnitude of voltage applied. Conversely, when the material is deformed a voltage difference is seen between the surfaces. This property leads to the greatest benefit of piezoelectric transducers: their ability to both send and receive signals. Piezoelectric transducers are small and light and can be bonded to or embedded within a structure with little effect. Signals are voltage based and therefore easy to generate and acquire with common hardware. Lead zirconate titanate (PZT) is the most commonly used material in piezoelectric transducers. They offer excellent performance for both generation and acquisition, have excellent mechanical strength, wide frequency responses, low power consumption and can be obtained at a low cost [17].

When actuating Lamb waves it is desirable to actuate the least number of modes possible (preferably only the S_0 and A_0) so that signal interpretation is simplified. As mentioned earlier, this usually occurs below $1.5MHz\text{-}mm$. This range is also beneficial because there is low dispersion, which means that if the frequency changes as the wave propagates through the material,

its velocity will remain relatively constant, therefore simplifying signal interpretation. It is desirable to send out a single pulse so that the propagation of the wave groups can be analyzed. The challenge then lies in producing an instantaneous pulse that can be controlled and actuated at a desired frequency. There is no control over a frequency generated by a simple impulse, therefore a short burst must be emitted. If a simple sine wave composed of a few cycles is emitted then the desired frequency can be actuated however, the frequency domain of such a signal shows small secondary peaks in the frequency domain that are present at other at other frequencies. To eliminate these peaks the signal can be modulated with a window function to slowly increase and decrease the magnitude of the signal [18]. A commonly used signal that provides a good compromise between number of cycles and ramp up rate consists of five sine peaks modulated by a Hann window. A signal with an odd number of peaks is used so that there is a clear maximum peak that can be used for signal processing (if an even number of peaks were used then there would be two peaks with the same maximum amplitude).

2.2. Proposed Network Technique

The technique developed in this research aims to provide a practical, modular network that is sparse and can be expanded to cover a large area. Generally, tomography requires a dense network of transducers that cannot be easily expanded to cover a larger inspection area. The proposed technique makes use of a hexagonal arrangement, which is modular in the sense that it uses a 'unit cell' that can be repeated to expand the network to cover a large inspection area. The unit cell consists of 12 transducers in a hexagonal arrangement as shown in Figure 1a. The network can be expanded by simply increasing the number of unit cells as shown in Figure 1b. A further benefit is that two unit cells can share three transducers, which means that another unit cell only requires nine new transducers.

Each transducer can act as both an actuator and a sensor. Inspection begins by actuating one transducer to send Lamb waves through the material and recording the signals with the remaining transducers. This is then repeated 11 times such that each transducer acts as an actuator once. Since there is one actuator and 11 sensors, there are 11 actuator-sensor pairs per transducer with direct paths between them as shown in Figure 1a.

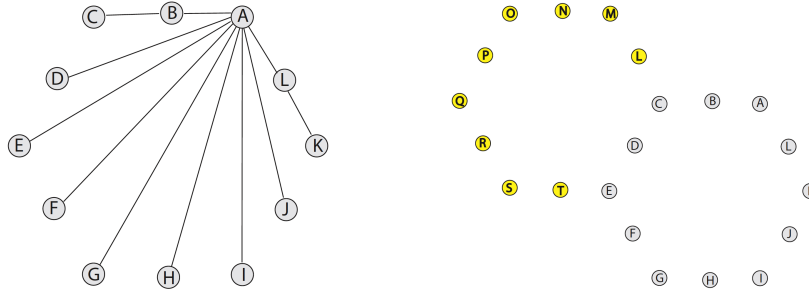


Figure 1: a) Hexagonal network showing actuator-sensor paths from transducer A (left) and b) expansion of a single unit cell (right)

2.3. Damage Location Algorithm

Once data is collected in undamaged and various damaged states, a technique must be implemented to locate the damage. Various techniques have been developed; each relies on a difference between the damaged and undamaged state. Such techniques include: delay-and-sum beam-forming [19], the time-difference-of-arrival method [20], the energy arrival method [21] and the filtered back-projection method [22]. To implement the proposed sparse hex network an algorithm was developed that incorporates damage progression information. This algorithm can be incorporated with existing algorithms to increase their accuracy.

The algorithm selected for this research was the reconstruction algorithm for probabilistic inspection of damage (RAPID) [12]. It was developed for networks based on 8-16 transducers and has inherently good signal-to-mean-noise ratios [13], it can accept various input parameters and produces reasonably accurate results [22]. Changes in the transmitted Lamb wave signal are related to a change in the material properties (ie. damage) between two sensors. The probability of defect presence at a certain point can be reconstructed from the severity of the signal change and its relative position to the actuator/sensor pair [12]. The RAPID algorithm is based on two assumptions: *i*) all effects from every possible actuator/sensor pair can be expressed as a linear summation across the entire inspection region, *ii*) information from a specific actuator/sensor pair contributes to the defect distribution estimation of a sub-region in the vicinity of the path between the pair.

Equation (1) describes the RAPID algorithm:

$$P(x, y) = \sum_{k=1}^N p_k(x, y) = \sum_{k=1}^N A_k \left(\frac{\beta - R}{\beta - 1} \right) \quad (1)$$

where $P(x, y)$ is the probability of the existence of a defect at position (x, y) , the Cartesian coordinate of a point in the inspection area, A_k is the damage metric as described below, β is a scaling factor that defines the sub-region that the actuator/sensor pair has an effect on (essentially an ellipse with the actuator and sensor at its foci) and $R(x, y)$ is described in Equation 2 as:

$$R(x, y, x_{1k}, y_{1k}, x_{2k}, y_{2k}) = \frac{\sqrt{(x - x_{1k})^2 + (y - y_{1k})^2} + \sqrt{(x - x_{2k})^2 + (y - y_{2k})^2}}{\sqrt{(x_{1k} - x_{2k})^2 + (y_{1k} - y_{2k})^2}} \quad (2)$$

where (x_{1k}, y_{1k}) is the Cartesian coordinate of the actuator and (x_{2k}, y_{2k}) is the Cartesian coordinate of the sensor. In this work a value of 1.05 was selected for β as it is the commonly used value [22, 23, 24].

A_k is a damage metric that is extracted from the Lamb wave signals. It can be based on various phenomenon such as a reduction in transmitted power, reduction in magnitude of waves or delay in arrival time. More recently Moustafa, A. et al [25] used the fractal dimension with a modified box-counting algorithm. The fractal dimension is a metric used to compare two curves and is calculated as the Hausdorff dimension. The most commonly used metric is the signal difference coefficient (SDC) used by various researchers [22, 23, 24]. This metric will be used as a baseline to compare results with the proposed algorithm. The signal difference coefficient between two data sets is defined as:

$$SDC = 1 - |\rho_{ab}| \quad (3)$$

where:

$$\rho_{ab} = \frac{1}{S} \frac{\sum_{i=1}^S (a_i - \mu_a)(b_i - \mu_b)}{\sqrt{\left\{ \sum_{i=1}^S (a_i - \mu_a)^2 \right\} \left\{ \sum_{i=1}^S (b_i - \mu_b)^2 \right\}}} \quad (4)$$

and S is the total number of samples, a_i and b_i are the initial data and damaged data, respectively at sample i and μ_a and μ_b are the arithmetic mean value of the initial data set and damaged data set, respectively.

Most damage detection systems rely solely on detecting damage as it occurs, ie. by comparing the change in the damaged state with the undamaged state. In reality however, damage often begins as a small flaw that slowly increases in size while in service. As the damage grows, information can be collected that can be used to locate the damage before it is large enough to be detected by algorithms without this information. In this work, a novel technique is developed that incorporates information from the damage progression into the RAPID algorithm to increase the effectiveness and enable its use in sparse networks where it may otherwise not be applicable.

To incorporate damage progression information, the magnitude of power from the transmitted Lamb waves is compared with that from the previous state (the previous hole size in the case of this study). If the power is less then there is the possibility that either damage is progressing in that path or external noise has caused a decrease in the signal. A history of the progression is recorded and if the power consistently drops across a particular path the probability of damage in that location is multiplied by an amplification factor. This is done in order to differentiate between noise and damage progression. Naturally, the initial damage states will not accurately show a damage progression however, as the trend continues across more damage states the accuracy increases and the results become more reliable. In this study an amplification factor of 1.10 (a 10% increase) was selected.

3. Experimental Investigation

To investigate the potential of the proposed network, experiments were conducted on a composite panel with a single unit cell of 12 transducers arranged in a hexagonal pattern as in Figure 1a. Reference data was collected while the material was in pristine condition and again with incrementally greater induced damage in the form of a through hole. The data was processed using the RAPID algorithm in order to determine the location of the damage.

3.1. Experimental Setup

A 420mm x 420mm panel, composed of eight plies of 139gsm, unidirectional T700 carbon fiber with West System 105/206 epoxy was laminated in a $[0/90/\pm 45]_S$ orientation to produce a 1.23mm thick quasi-isotropic composite. A jig was machined to locate and bond 12, 1mm thick, 7.56mm diameter PZT transducers to the panel in a 75mm circumradius hexagonal

array. The panel and network are shown in Figure 2a, while a close up of the network showing the damage location is shown in Figure 2b. Each transducer was assigned a letter for reference as seen in Figures 1 and 2. The coordinates of the transducers are: A : (247.50, 274.95), B : (210.00, 274.95), C : (172.50, 274.95), D : (153.75, 242.48), E : (135.00, 210.00), F : (153.75, 177.53), G : (172.50, 145.05), H : (210.00, 145.05), I : (247.50, 145.05), J : (266.25, 177.53), K : (285.00, 210.00) and L : (266.25, 242.48) in mm from the lower left corner of the panel. Damage was induced at: (228.75, 241.85).

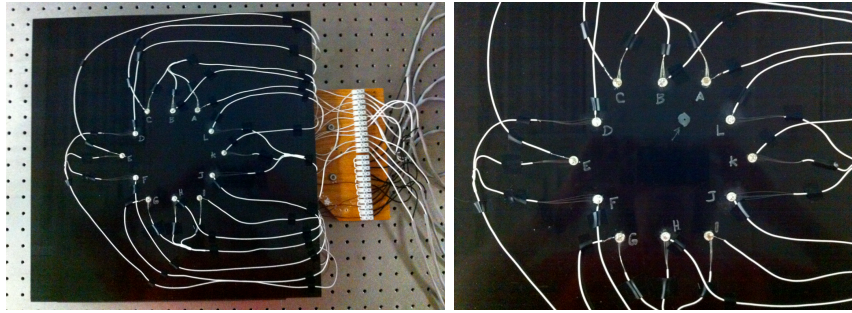


Figure 2: a) Composite panel with hex network (left), b) hex network with induced damage (right)

A National Instruments NI PXI-5421 arbitrary waveform generator was used to generate a signal while a NI PXI-5105 digitizer/oscilloscope was used to acquire the signal. Both units were installed in a NI PXI-1033 chassis and controlled with a custom National Instruments LabView program. A model A-303 amplifier from A.A. Labs Ltd. was used to amplify the generated signal.

3.2. Signal Generation and Acquisition

An actuation signal consisting of a sine wave with five peaks modulated by a Hann window was employed. An amplitude of $\pm 8V$ was produced by the waveform generator and amplified by a factor of 20 before it was sent to the actuator resulting in a maximum amplitude of $\pm 160V$. The actuation frequency was selected based on a number of criteria. In order to only actuate the S_0 and A_0 modes the frequency-thickness product was kept below $1.5MHz\text{-}mm$. A frequency scan from $100kHz$ to $400kHz$ was performed to determine the frequency that transmitted the greatest amplitude. It was found that the frequency range of $260\text{-}270kHz$ transmitted the greatest amplitude, therefore $265kHz$ was used for the experiments.

With these properties selected, the waveform generator was programmed to output the actuation signal at $100MHz$. Data was acquired at $60MHz$ for 30×10^3 samples ($500\mu s$). An ASCII text file was written after each run and saved for data processing.

3.3. Experimental Procedure

Once the experimental apparatus was setup as described above, a number of experiments were performed under various damage conditions. Each experiment consists of actuating one transducer and sensing the other eleven, then actuating the adjacent transducer and sensing with the remaining eleven. This process is repeated until all 12 transducers have actuated the system once. At this point the damage is increased and the process is repeated.

Initially the experiment was conducted on the panel in pristine condition before damage was inflicted in the form of a hole drilled through the panel at a location such that it intersected the paths between PZT pairs $A-G$ and $C-K$ as shown in Figure 2b. The initial diameter of the hole was $1.59mm$, which was increased to $2.38mm$, $3.18mm$, $4.00mm$, $4.76mm$ and finally $6.35mm$.

4. Discussion

The main objective of this work is to develop a modular sparse network. To achieve this an algorithm that uses damage progression information is introduced. With this algorithm, two damage metrics were implemented. The first is based on the SDC in order to compare the proposed algorithm to a conventional metric (SDC). The second damage metric is based on the transmitted power of the signal from an FFT analysis. For both metrics, a comparison between the results with and without the damage progression algorithm is made to assess the effectiveness. A third case was also considered that neglected information from every second sensor, essentially creating a more sparse network of six transducers however, this did not produce any reasonable results therefore implying that minimum of 12 transducers are required in this situation.

Figure 3a presents an example of the received S_0 and A_0 waveforms actuated by transducer A and received by transducer G . All damage states are plotted together on the same chart with their peaks marked with an asterisk (*). Figure 3b shows a close up of the A_0 peak; a consistent decrease in amplitude due to damage is clearly seen. Signals like these from all paths are processed to determine if a decreasing trend exists.

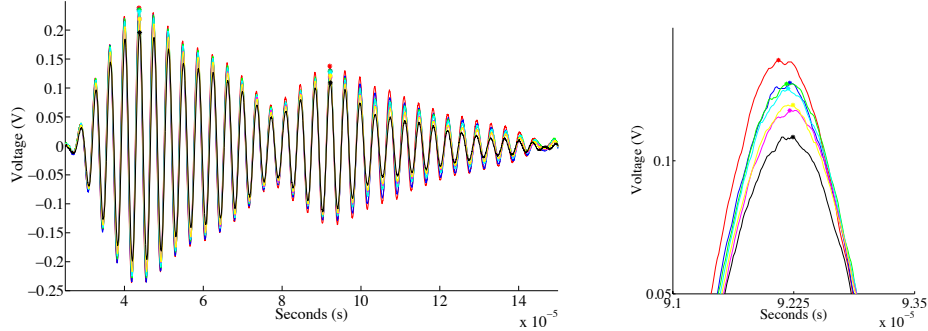


Figure 3: a) Received Lamb wave signals at all seven damage states along path *A-G* (left) and b) close up of A_0 wave (right)

To bench mark the results, the SDC was calculated for each actuator-sensor path and implemented in the RAPID algorithm. A contour plot indicating the probability of damage is presented in Figure 4a. The damage location is indicated with the yellow cross and circle. With this information no damage could be detected. This is reasonable according to Michaels, J.E. [13] who reported that the technique was not highly effective on large, sparse arrays. The aforementioned damage progression information was also implemented with the SDC metric. The results are shown in Figure 4b. While the algorithm was not able to detect the exact location of the damage it did locate a region close to the general area of the damage therefore showing a marked increase in accuracy by using damage progression information.

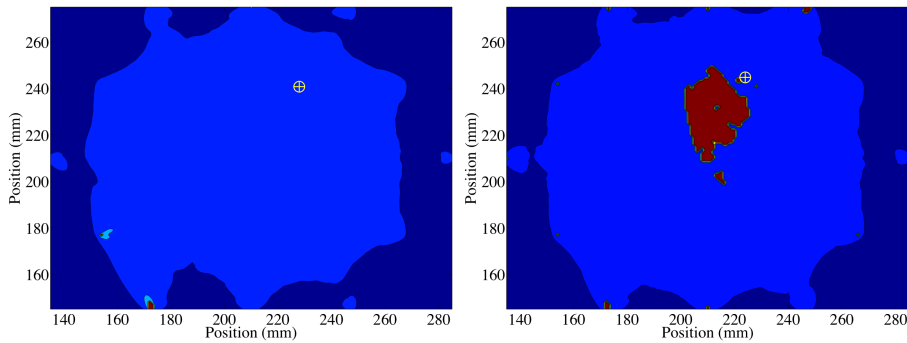


Figure 4: a) SDC results with no damage progression factor (left), b) SDC results with damage progression factor of 1.10 (right) *Damage location indicated by yellow cross

In the second implementation the transmitted power was used as the

damage metric. An FFT analysis was performed on data from every actuator-sensor path to extract the magnitude of transmitted power. The RAPID algorithm was implemented and the results are shown in Figure 5a. At this point the algorithm has located three possible damage locations compared to zero locations with the SDC metric. The algorithm was implemented with the damage progression information as shown in Figure 5b. With this information the algorithm has located a small region of damage roughly the same size within a $12mm$ radius. While these results are not highly accurate they do demonstrate that the use of information from the damage progression does increase the probability of damage detection and allows a large, sparse network to be used.

Many similar research efforts focus on aluminum rather than composite making it difficult to compare results. The results from the experiments performed here are an improvement over the work on an aluminum panel by Hay, T.R. et al [22] as a larger spaced array is implemented with fewer transducer with results comparable to Liu, Y. et al [26] who were able to detect a $30mm \times 30mm$ delamination to within $10.2mm$ using an array of four transducer pairs arranged in a square with sides of $225mm$ in length. In general, this technique allows for a larger spaced array with a lower density of transducers.

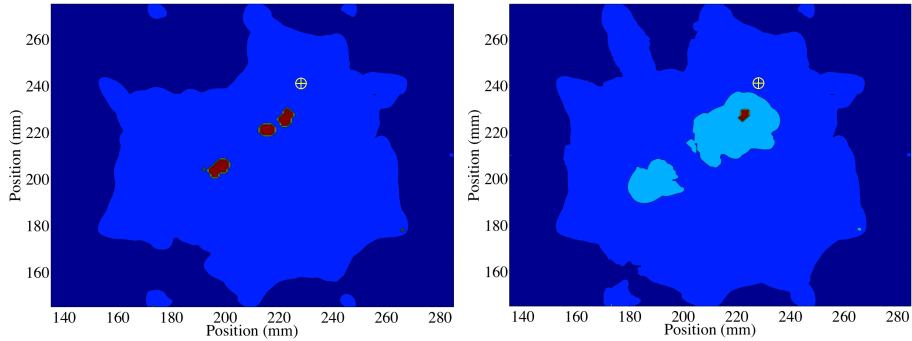


Figure 5: a) Power amplitude results with no damage progression factor (left), b) Power amplitude results with damage progression factor of 1.10 (right) *Damage location indicated by yellow cross

5. Conclusion

A novel sparse network that can be expanded to cover any size area has been proposed along with a novel technique for incorporating information on

the progression of damage to improve the accuracy of existing algorithms.

The network consists of a unit cell of 12 piezoelectric transducers arranged in a hexagonal pattern as shown in in Figure 1a. The network is easily expanded by adding nine more transducers to the existing 12 as shown in in Figure 1b (two unit cells). The hexagonal arrangement allows for efficient stacking of unit cells that would not be otherwise possible with a circular array.

Damage progression information was implemented in the form of a 10% increase in signal magnitude if the actuator-sensor path showed a consistent decrease in power across each damage state (ie. if the power was consistently less than the previous state). The results presented in Figure 4 show that incorporating the damage progression information increases the chance of detection with SDC as a damage metric. When the power of the transmitted wave is used as a damage metric some potential damage locations appear as shown in Figure 5a. When the damage progression information is incorporated the accuracy is increased, locating a potential damage site that is within $12mm$ of the actual damage as shown in Figure 5b. While the results do not directly pinpoint the damage location they do show that an improvement over the existing RAPID algorithm can be made by incorporating damage progression information with the use of a larger area sparse network on a carbon fiber composite material.

References

- [1] Y. Bar-Cohen, A. Mal, S. S. Lih, Z. Chang, Composite materials stiffness determination and defects characterization using enhanced leaky Lamb wave dispersion data acquisition method, in: SPIE Annual International Symposium on NDE of Aging Aircraft, Airports, and Aerospace Hardware.
- [2] K. Worden, C. R. Farrar, G. Manson, G. Park, The fundamental axioms of structural health monitoring, Proceedings of the Royal Society A: Mathematical, Physical and Engineering Sciences 463 (2007) 1639–1664.
- [3] K. Worden, An introduction to structural health monitoring, The Philosophical Transactions of the Royal Society A (2007).
- [4] H. Lamb, On Waves in an elastic plate, Proceedings of the Royal Society A: Mathematical, Physical and Engineering Sciences 93 (1917) 114–128.

- [5] D. Worlton, Experimental confirmation of Lamb waves at megacycle frequencies, *Journal of Applied Physics* 32 (1961) 967.
- [6] C. Frederick, D. Worlont, Ultrasonic thickness measurements with Lamb waves, *Journal of Nondestructive Testing* 20 (1962) 51–55.
- [7] D. Jansen, D. Hutchins, Lamb wave tomography, in: *IEEE Symposium on Ultrasonics*, IEEE, ????, pp. 1017–1020.
- [8] D. Hutchins, D. Jansen, C. Edwards, Lamb-wave tomography using non-contact transduction, *Ultrasonics* 31 (1993) 97–103.
- [9] D. Jansen, D. Hutchins, J. Mottram, Lamb wave tomography of advanced composite laminates containing damage, *Ultrasonics* 32 (1994) 83–90.
- [10] Y. Nagata, J. Huang, J. Achenback, S. Krishnaswamy, Lamb wave tomography using laser-based ultrasonics, in: *Review of Progress in Quantitative Nondestructive Evaluation*, volume 14, pp. 561–568.
- [11] S. Prasad, K. Balasubramaniam, C. Krishnamurthy, Structural health monitoring of composite structures using Lamb wave tomography, *Smart Materials and Structures* 13 (2004) N73–N79.
- [12] H. Gao, Guided wave tomography on an aircraft wing with leave in place sensors, in: *Review of Progress in Quantitative Nondestructive Evaluation*, AIP, 2005, pp. 1788–1794.
- [13] J. Michaels, Effectiveness of in situ damage localization methods using sparse ultrasonic sensor arrays, in: *Proceedings of the SPIE*.
- [14] N. Guo, P. Cawley, The Interaction of Lamb waves with delaminations in composite laminates, *The Journal of the Acoustical Society of America* 94 (1993) 2240–2246.
- [15] C. H. Keilers, F. K. Chang, Identifying delamination in composite beams using built-in piezoelectrics: Part I-experiments and analysis, *Journal of Intelligent Material Systems and Structures* 6 (1995) 649–663.
- [16] V. Giurgiutiu, A. Zagrai, J. Bao, Piezoelectric wafer embedded active sensors for aging aircraft structural health monitoring, *Structural Health Monitoring* 1 (2002) 41–61.

- [17] Z. Su, L. Ye, Y. Lu, Guided Lamb waves for identification of damage in composite structures: A review, *Journal of Sound and Vibration* 295 (2006) 753–780.
- [18] B. Rocha, C. Silva, A. Suleman, Structural health monitoring system using piezoelectric networks with tuned lamb waves, *Shock and Vibration* (2010) 677–695.
- [19] C. Wang, J. Rose, F. Chang, A synthetic time-reversal imaging method for structural health monitoring, *Smart Materials and Structures* 13 (2004) 415–423.
- [20] J. Michaels, A. Croxford, P. Wilcox, Imaging algorithms for locating damage via in situ ultrasonic sensors, *Sensors Applications Symposium*, 2008. SAS 2008. IEEE (2008) 63–67.
- [21] J. Michaels, T. Michaels, Damage localization in inhomogeneous plates using a sparse array of ultrasonic transducers, in: *Review of Progress Quantitative Nondestructive Evaluation*, volume 26, *Review of Quantitative Nondestructive Evaluation*, 2007.
- [22] T. Hay, R. Royer, H. Gao, X. Zhao, J. Rose, A comparison of embedded sensor Lamb wave ultrasonic tomography approaches for material loss detection, *Smart Materials and Structures* 15 (2006) 946–951.
- [23] J. V. Velsor, H. Gao, J. Rose, Guided-wave tomographic imaging of defects in pipe using a probabilistic reconstruction algorithm, *Insight - Non-Destructive Testing and Condition Monitoring* 49 (2007) 532–537.
- [24] F. Yan, R. Royer, J. Rose, Ultrasonic Guided Wave Imaging Techniques in Structural Health Monitoring, *Journal of Intelligent Material Systems and Structures* 21 (2010) 377–384.
- [25] A. Moustafa, S. Salamone, Fractal dimension-based Lamb wave tomography algorithm for damage detection in plate-like structures, *Journal of Intelligent Material Systems and Structures* (2012).
- [26] Y. Liu, M. Fard, A. Chattopadhyay, D. Doyle, Damage assessment of cfrp composites using a time-frequency approach, *Journal of Intelligent Material Systems and Structures* 23 (2011) 397–413.

Appendix D

Prediction of Fatigue Response of Composite Structures by Monitoring the Strain Energy Release Rate with Embedded fiber Bragg Gratings

Prediction of fatigue response of composite structures by monitoring the strain energy release rate with embedded fiber Bragg gratings

C.J.Keulen^a, F.F.Melemes^b, T.Boz^b, P.Chelliah^b, H. S.Turkmen^c,
M.Yildiz^{b,*}, A.Suleman^{a,*}

^a*University of Victoria, Department of Mechanical Engineering,
Victoria, B.C., V8W 3P6, Canada*

^b*Sabanci University, Faculty of Engineering and Natural Sciences,
Orhanli-Tuzla, 34956 Istanbul, Turkey*

^c*Istanbul Technical University, Faculty of Aeronautics and Astronautics,
Maslak, 34469 Istanbul, Turkey*

Abstract

Composite materials are becoming increasingly more valuable due to their high specific strength and stiffness. Currently, most components are operated for a number of service cycles then replaced regardless of their actual condition. Embedded fiber Bragg gratings (FBG) are under investigation for monitoring these components in real time and estimating their remaining life. This paper presents research conducted on a novel technique for prediction of the remaining life of composites under fatigue loading using embedded FBG sensors. A prediction is made of the remaining life at every cycle based on data collected from the sensors and the previous loading history.

Keywords: Fiber optics, Structural health monitoring, Sensor, Fiber Bragg gratings (FBG)

*Corresponding authors

Email addresses: ckeulen@uvic.ca (C.J.Keulen), fatihmelemes@sabanciuniv.edu (F.F.Melemes), talhaboz@sabanciuniv.edu (T.Boz), pandian@sabanciuniv.edu (P.Chelliah), halit@itu.edu.tr (H. S.Turkmen), meyildiz@sabanciuniv.com (M.Yildiz), suleman@uvic.ca (A.Suleman)

1. Introduction

Due to their high specific strength and stiffness, composite materials are becoming increasingly more valuable in fields such as aerospace, automotive, wind energy and civil infrastructure. In all of these applications the components are under cyclic fatigue loading.

Maintenance and inspection of components is a costly procedure. In most situations the cost is incurred two fold: i) inspection cost and ii) lost revenue. The challenge to the engineer lies in developing a structural health monitoring (SHM) system that is installed in the component in question and works in real time to monitor the structural integrity or 'health' of the component to reduce these drawbacks. It would be highly beneficial if the system estimates the remaining useful life (RUL) in real time before service is required.

One method currently under research is based on fiber optic sensors embedded within the composite material during manufacturing. Fiber optic sensors are an excellent choice for these applications as they are lightweight and flexible allowing them to be embedded within the host structure with little detrimental effect. Fiber Bragg grating (FBG) sensors show great promise for SHM applications [1]. They are intrinsic, reliable, inexpensive to produce, easily multiplexed and impervious to electromagnetic interference. The same embedded fiber optic sensors can also be used during the processing stage for resin flow monitoring and cure monitoring thereby assuring the initial quality of the component [2].

Some research has been done on determining the extent, location and type of damage, however no work has been done on the use of FBGs to monitor the cycle-by-cycle degradation of the structure and correlate this to the RUL in real time. This involves an investigation of current fatigue life estimation models and techniques to employ them with data acquired in real time by FBG sensors.

2. Fatigue Monitoring and Remaining Useful Life Prediction of Composite Material with Embedded FBGs

The main objective of this study is to determine the remaining useful life of a composite material using data obtained from embedded FBG sensors during the life of a structure. This involves selecting an appropriate fatigue life prediction model that is compatible with the data obtained from FBGs and implementing this model to accurately predict the remaining useful life.

Research into the detection of damage using embedded fiber optic sensors has been performed by various researchers [3]. It appears that Doyle et al were among the first to monitor the reduction in stiffness of composites during fatigue with an FBG [4].

Many researchers attempt to characterize the change in the reflection spectrum of an FBG to detect and measure the density of cracks based on the fact that a non-uniform strain distribution along an FBG causes broadening of the reflected spectrum [5, 6, 7]. Takeda et al attempted to correlate crack density with spectrum broadening using a theoretical model for crack density [5]. Yashiro et al, proposed a numerical approach to correlate the reflection spectrum of the embedded FBG sensor to damage [6]. Takeda et al proposed a method of addressing multiple damages near a stress concentration by a technique based on a layer-wise finite element analysis with cohesive elements [7]. Other techniques based on ultrasonic Lamb waves have shown promise [8]. These generally involve the use of piezoelectric transducers that send surface waves through the material while FBG sensors are used to detect the waves.

To our knowledge, no work has been done that incorporates embedded fiber optic sensors for remaining useful life prediction on a cycle by cycle basis.

2.1. Theory

An FBG is a segment of a single mode optical fiber core with a periodically varying refractive index in the axial (longitudinal) direction [9]. It allows a broad band of light to pass while reflecting a narrow band centered around a wavelength known as the Bragg wavelength, λ_B . The periodic modulation of the refractive index at the grating location will scatter the light traveling inside the fiber core. Out of phase, scattered waves will form destructive interference thereby canceling each other while in phase light waves will add up constructively forming a reflected spectrum. The reflected wavelength depends on the grating pitch (spacing between the refractive index variations), Λ and the variation in refractive index, n . An FBG satisfies the Bragg condition as $\lambda_B = 2n\Lambda$. The change in spacing of the periodic refractive index modulation is a function of both strain and temperature. If an FBG sensor is under a mechanical load or temperature variation, the spacing and average refractive index will change, therefore causing a shift in the Bragg wavelength $\lambda_B(n, \Lambda)$. The sensitivity of strain and temperature of a bare FBG is $\sim 1.2pm/\mu\varepsilon$ and $\sim 13.7pm/^\circ C$ [9] however it is prudent to

measure the strain and temperature sensitivity of every embedded FBG as factors such as variation in material properties and manufacturing tolerance will effect the sensitivity.

Fatigue of composites has been an area of interest for over forty years. The fatigue behavior of composites is a complex phenomenon due to various types of damage that can occur (fiber fracture, matrix cracking, fiber buckling, fiber-matrix interface failure, delamination, etc.) and interact with each other [10]. Research has shown that the damage process in fiber reinforced composites under fatigue loading is progressive and is a combination of various damage modes. The field of fatigue life modeling of composite materials is extensive, however there is still no widely accepted model that most engineers agree upon. Many excellent references that cover a variety of available models exist such as [10, 11, 12] among others.

As observed by various researchers, the effect of fatigue on the stiffness of fiber reinforced polymer matrix composites follows a trend. This trend can be characterized by three stages as shown in the plot of our test results in Figure 1. Stage I is characterized by a sharp, non-linear decrease in stiffness. This is attributed to a rapid interconnection of matrix cracking initiated by shrinkage stresses, degree of resin cure, voids and fiber discontinuities. This stage is generally limited to the first 15-25% of fatigue life. Stage II is characterized by a gradual, linear decrease in stiffness that occurs between 15-20% to 90% of the fatigue life. This decrease is attributed to matrix cracking leading to crack propagation, fiber debonding and delamination. The final stage shows a sharp non-linear decrease eventually resulting in a sudden fiber failure [13]. Interestingly, the very initial stages of fatigue testing results in an increase in stiffness that is generally attributed to viscoelastic deformation of the matrix allowing for fiber alignment along the axis of loading [14].

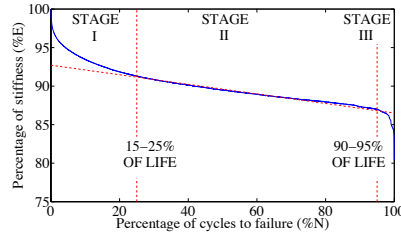


Figure 1: Stiffness degradation vs. fatigue cycle

Researchers have shown that $S - N$ curves of unidirectional composites

have virtually no clear threshold stress level as established in metals, however it is recognized that a certain threshold level of strain in resin does exist for indefinite fatigue life although it is very low, around 5-10% of the ultimate strain [13]. Hence, life prediction models based on $S - N$ curves may not be applicable for fiber reinforced plastic (FRP) composite materials.

A small number of models will be described here in an attempt to demonstrate why the strain energy release rate model was selected as well as to give the reader an idea of the variables involved in such models and how they are applied. This is by no means a comprehensive coverage of the subject.

One of the first fatigue life models was proposed by Hashin and Rotem [15] as: $\sigma_A = \sigma_A^u$ and $\left(\frac{\sigma_T}{\sigma_T^u}\right)^2 + \left(\frac{\tau}{\tau^u}\right)^2 = 1$, where σ_A and σ_T are the stresses along the fibers and transverse to the fibers, τ is the shear stress and σ_A^u , σ_T^u and τ^u are the ultimate tensile, transverse tensile and shear stress, respectively. Because the ultimate strengths are functions of the fatigue stress level, stress ratio and number of cycles the criterion is expressed in terms of three $S - N$ curves that are determined experimentally. The criteria are only valid for laminates with unidirectional plies.

Much research was done on phenomenological models to predict the stiffness degradation of composites by Whitworth [16, 17], and Yang [18]. Hwang and Han introduced the fatigue modulus concept [19]. The fatigue modulus concept is described as the slope of applied stress and resultant strain at a specific cycle. The degradation rate of the modulus is assumed to follow a power function: $\frac{dF}{dn} = -Acn^{c-1}$, where F is the fatigue modulus, n is the number of cycles and A and c are material constants. They assume that the applied stress σ_a varies linearly with the resultant strain such that: $\sigma_a = F(n_i)\varepsilon(n_i)$, where $F(n_i)$ and $\varepsilon(n_i)$ are the fatigue modulus and strain at loading cycle n_i , respectively. The strain life, N can be calculated by integrating from $n_1 = 0$ to $n_2 = N$ and introducing the strain failure criteria, which states that failure occurs when the fatigue strain reaches the ultimate static strain to obtain: $N = [B(1 - r)]^{1/c}$, where $B = F_0/A$, F_0 is the fatigue modulus at the 0th cycle, A is area, $r = \sigma_a/\sigma_u$ is the ratio of applied cyclic stress to ultimate static stress and c is a material constant. Hwang and Han also proposed three cumulative damage models based on the fatigue modulus [20]. Lee used a stiffness degradation model to predict failure [21].

Whitworth used the residual stiffness model to propose a cumulative damage model [22]. In this model the damage function is defined as: $D = \left[\frac{H \cdot (1 - \bar{S})^a}{1 - \bar{S}^a}\right] \cdot \frac{n}{N}$, where $\bar{S} = S/R(0)$ is the normalized applied stress range,

$R(0)$ is the ultimate strength, S is the applied stress range and a and H are parameters. When $D = 0$ no cycles have been applied and when $D = 1$ failure has occurred. This model degenerates into the Miner damage model when a becomes unity, i.e. when the stiffness degrades linearly until failure. This model has been extended to predict the remaining life of specimens subject to variable amplitude loading. Whitworth used the variable amplitude approach to convert a number of cycles at a particular stress to a number of cycles at a reference stress. These stress values are summed and when the values equal one, failure occurs [22].

The aforementioned models take factors such as stress, strain, stiffness and number of cycles and develop abstract material properties to develop a formulation. Other researchers have investigated other properties as an indication of fatigue. The challenge with these models is that they all require knowledge of the load/stress applied to the composite. With FBG sensors this data is not available; only the strain is sensed.

2.2. Application of fatigue life prediction models to FBG based RUL

The relevant data collected from an FBG is in the form of strain and number of cycles. As described above, the stiffness of composite materials under fatigue loading gradually decreases over time. This means that the modulus of elasticity is not constant, it is a function of the load history and the stress-strain relationship (Hooke's law) can no longer be applied to extract the magnitude of stress from strain. Therefore a suitable model cannot use stress as an input; it must use the strain.

A promising method of predicting the remaining useful life using only strain was developed by Natarajan et al [13]. The method relies on the strain energy release rate and takes advantage of the fact that it is linear throughout Stage II. It follows a similar approach to the fatigue modulus concept proposed by Hwang and Han [19].

To apply this model the material must be characterized to obtain a relationship between applied strain, ultimate strain and the energy release rate. The method assumes that there is a specific amount of strain energy in the material that is released before it enters Stage III, at which point it is past its useful life. The strain energy can be determined before fatigue loading and used to predict the number of cycles to failure. An example of the progression of the release of strain energy from a composite during fatigue is shown in Figure 2. This method can be employed as a cumulative model if the energy is summed over each cycle. In this research it is proposed to

use this method to calculate the released energy on a per-cycle basis using strain data obtained from embedded FBGs to predict the remaining life. The complete derivation of this method is presented in [13]. An abbreviated version is presented here along with a modification so it can be applied to FBG acquired strain/cycle data.

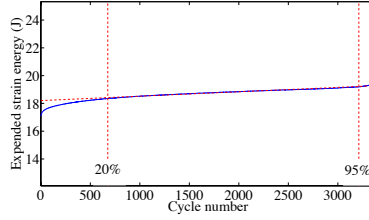


Figure 2: Expanded strain energy during fatigue loading

The variation of expended energy can be described as:

$$\frac{dU_j}{dN_j} = f(\varepsilon_m, \varepsilon_{sr}, U_j, C_t) \quad (1)$$

where U_j is the expended energy, N_j is the load cycle, ε_m is the mean strain, ε_{sr} is the strain range, C_t is the composite type. Equation (1) can be written in terms of the number of cycles:

$$N_j = \int_{U_0}^{U_j} \frac{dU}{f(\varepsilon_m, \varepsilon_{sr}, (U_j - U_0), C_t)} \quad (2)$$

where U_0 is the initial strain energy prior to fatigue initiation and:

$$U_j = U_0 \cdot g(\varepsilon_m, \varepsilon_{sr}, (U_j - U_0), C_t) \quad (3)$$

where the function: $g(\varepsilon_m, \varepsilon_{sr}, (U_j - U_0), C_t)$ must be determined experimentally. Differentiating Equation (3) with respect to N_j :

$$\frac{1}{U_0} \frac{dU_j}{dN_j} = g' \{ \varepsilon_m, \varepsilon_{sr}, (U_j - U_0), C_t \} \cdot f \{ \varepsilon_m, \varepsilon_{sr}, (U_j - U_0), C_t \} \quad (4)$$

and rearranging (4):

$$f \{ \varepsilon_m, \varepsilon_{sr}, (U_j - U_0), C_t \} = \frac{1}{U_0} \left(\frac{dU_j}{dN_j} \right) \left(\frac{1}{g' \{ \varepsilon_m, \varepsilon_{sr}, (U_j - U_0), C_t \}} \right) \quad (5)$$

The right hand side of Equation (5) must be evaluated for $\varepsilon_m, \varepsilon_{sr}$ keeping the other parameters constant.

The energy release rate: dU_j/dN_j (the rate of energy expended per load cycle) is linear throughout Stage II, therefore the energy release rate for the material at various strain levels can be determined experimentally. The function: $f(\varepsilon_m, \varepsilon_{sr}, U_j, C_t)$ can then be determined by plotting the variation of the energy release rates with maximum induced strain.

The data obtained during fatigue loading should be load and deflection. This data is then used to calculate the strain energy U_n at any cycle: $U_n = \frac{P_n \delta_n}{2}$, where P_n is the load at n cycle and δ_n is the deflection a n cycle.

The amount of energy released at 90% of the life cycle (when the material enters Stage III) compared to the initial amount of energy changes based on the ratio: $r = U_f/U_0$. Failure is assumed to occur at this point as the material is no longer intact and dangerously close to catastrophic failure, therefore: $N_f = N_{90\%} = 0.9N_{ult}$.

The slope of Stage II is the expended energy per cycle or the energy release rate: dU/dN . This can be obtained for each specimen by performing a regression analysis of the expended energy data in Stage II. The energy release rate is found to be constant and is characteristic of the constitutive material under similar loading conditions and increases with an increase in induced strain.

Experimental data of the variation in energy release rates with normalized maximum induced strain is fit to a power law:

$$\frac{dU}{dN} = a \left(\frac{\varepsilon_{max}}{\varepsilon_{ult}} \right)^b \quad (6)$$

where ε_{max} is the maximum induced strain of the material, ε_{ult} is the ultimate static strain of the material (assumed to remain constant throughout the lifetime) and a and b are fatigue coefficients.

Since the coefficients a and b are invariant for a particular material under a given load type, the fatigue life can be written as:

$$N_f = \frac{U_0 - U_f}{a(\varepsilon_{max}/\varepsilon_{ult})^b} \quad (7)$$

where U_0 is the initial strain energy of the material at ε_{max} before fatigue loading, U_f is the sum of the expended strain energy at the end of Stage II and N_f is the fatigue life just before entering Stage III.

Since the specimen is loaded linearly up to the mean strain level before applying fatigue load, the expended energy of the material before fatigue loading is the energy at the mean level. The energy of the material at 0 cycles can be written as:

$$U_0 = \frac{P_{mean}^2 l}{2AE} \quad (8)$$

where P_{mean} is the mean level of the cyclic load, E is the modulus of elasticity in the loading direction, l is the span (gage length) and A is the cross sectional area. The fatigue life of a material can be obtained experimentally for a particular loading from Equations (2) and (6), at N_f and written as:

$$N_f = \frac{U_0 - rU_0}{a(\varepsilon_{max}/\varepsilon_{ult})^b} = \frac{(1-r)U_0}{a(\varepsilon_{max}/\varepsilon_{ult})^b} \quad (9)$$

Life prediction can be accomplished by summing the energy released under various load amplitudes for the corresponding number of cycles and finding N_f after inserting the total expended energy into Equation (9). In the case of an FBG based SHM system, the magnitude of the strain is sensed on every cycle. With this method it is possible to sum the energy on a cycle-by-cycle basis using data obtained from the FBG.

To calculate the energy released during one cycle, Equation (6) is integrated with respect to N over one cycle, ie. from N_j to N_{j+1} and ε_{max} is replaced with $\varepsilon_j^{(FBG)}$, the maximum strain value recorded by the FBG during cycle j . This leads to:

$$\Delta U_j = a \left(\frac{\varepsilon_j^{(FBG)}}{\varepsilon_{ult}} \right)^b \quad (10)$$

when $(N_{j+1} - N_j) = 1$.

The energy released during each cycle can then be summed during the life of the composite to get the total expended energy up to that cycle: $U_{expended} = \sum_{j=1}^n \Delta U_j$. The remaining life can be estimated: $U_{remaining} = (1-r)U_0 - U_{expended}$, where $U_{remaining}$ is the remaining energy left in the material before failure. Equation (7) can be modified to convert the remaining energy into the number of remaining cycles:

$$N_{n-f} = \frac{U_{remaining}}{a(\varepsilon_{expected}/\varepsilon_{ult})^b} \quad (11)$$

where N_{n-f} is the remaining life at cycle n , $\varepsilon_{expected}$ is the expected strain level for the remainder of the life. For example, $\varepsilon_{expected}$ could be the average maximum strain from the previous portion of life or if the component was expected to be under harsher loading, $\varepsilon_{expected}$ would be greater than the average maximum strain. With Equation (11) various fatigue cycle scenarios could be predicted for various loading cycles by modifying the value of $\varepsilon_{expected}$. The addition of Equations (10) and (11) to the fatigue life prediction technique developed by Natarjan [13] allow for a stepwise addition of expended energy. This is a novel approach to remaining useful life prediction that allows a prediction to be made at each cycle.

3. Experimental Verification

Experimental validation is required to explore the potential of this technique. This involves producing fatigue specimens with and without embedded FBG sensors, testing them to characterize the material then testing and applying the failure model to specimens that contain embedded FBGs.

3.1. Specimen preparation

A number of processing methods exist for composite materials. One method that is particularly suitable to produce composite parts satisfying stringent specifications of the aircraft industry is the Resin Transfer Molding (RTM) technique. RTM can produce high quality near net-shape parts with high fiber volume fractions, two high quality surfaces and little post processing in a fully contained system that eliminates human operator exposure to chemicals and reduces the chance of human error. For these reasons RTM has been selected to produce the specimens for this study. A sophisticated laboratory-scale apparatus has been designed and built with the ability of embedding fiber optics into the composite component. This apparatus is used to produce flat panels $620mm \times 320mm \times 3.5mm$ that are processed into specimens for fatigue testing.

The laminate selected for this research is $[0/90]_{6S}$ E-glass fiber with epoxy resin. The fiber used is Metyx LT300 E10A 0/90 biaxial E-glass stitched fabric with $161gsm$ in the 0° orientation and $142gsm$ in the 90° orientation, summing to $313gsm$ total. The selected resin is Araldite LY 564 epoxy resin with XB 3403 hardener produced by Huntsman Corporation. The panels undergo an initial cure at $65^\circ C$ for 24 hours with a post cure at $80^\circ C$ for 24 hours. Three panels were produced for this study and processed into

specimens. Specimens were named with the convention #-##; with the first number indicating the panel they were cut from and second indicating the order in which they were cut. Panel numbering starts at #2 as panel #1 was used for preliminary investigation.

Each panel produces ~ 30 specimens. A tabbing material composed of 1.5mm thick, plain weave E-glass non-crimp fabric/epoxy with a $\sim 20^\circ$ angle on one edge is bonded with West System 105 epoxy and 205 hardener thickened with milled glass fiber with a bond-line thickness of 0.7mm . The panels are cut on a water-cooled diamond blade saw and the edges polished up to 400 grit sandpaper. The final dimensions of the specimens are $280\text{mm} \times 15\text{mm} \times 3.5\text{mm}$ with a 160mm gage length. The length of the specimen is aligned with the 0° fiber orientation.

A special fixture is required to grip the specimen such that the fiber optic ingress location is not under load. The fixture consists of three steel plates, a bar and a pin. Two plates are clamped across either side of the specimen with bolts. One plate has a slot that allows the fiber to egress from the composite. The plates are screwed into the third plate that has a cylindrical pin that interfaces with the machine grips. A stiffening bar is located across the slot to reduce deflection when the bolts are tightened.

3.2. Testing equipment

All tests were performed on an MTS 322 test frame with MTS 647 hydraulic wedge grips using an MTS FlexTest GT digital controller with MTS Station Manager software. Load and displacement data was collected with a built in load cell, model: MTS 661.20F-03 and linear variable differential transformer (LVDT), respectively. Strain was collected with an axial extensometer, model: MTS 634.25F-24. All FBG data was collected with a Micron Optics SM230 interrogator using Micron Optics Enlight software. Temperature data was collected with a K-type thermocouple using a National Instruments NI SCXI-1314 DAQ card in a NI SCXI-1000 chassis with LabVIEW software. The fiber Bragg gratings used in the experiments were 10mm long with a center wavelength of either 1555 or 1565nm supplied by FiberLogix. All data is acquired at a sampling rate of 100Hz .

3.3. Test procedure

First, the material must be characterized by determining the relationship between the stress release rate and strain, i.e. determine the fatigue coefficients (a and b from Equation (6)). To do this, static testing must be

performed to determine the ultimate tensile strain, ε_{ult} . After ε_{ult} is determined, a number of samples at various strain levels are fatigue tested. From this data the strain energy release rate as a function of strain may be determined. Once the values of a and b from the energy release rate curve are determined the specimens with embedded FBGs can be tested. For this study, a number of fatigue tests at each of the following strain amplitudes ($\varepsilon_{max}/\varepsilon_{ult}$): 0.8, 0.75, 0.7, 0.6, 0.5 and 0.4 are performed including two fatigue tests with specimens containing embedded FBGs. A static test is also performed to determine the ultimate strain of the embedded FBG.

Autogeneous heating becomes a concern during fatigue testing of glass fiber reinforced composites as the heat is not quickly conducted to the environment as it is with metallic materials. The fatigue properties of composites are especially sensitive to heat. Generally a fatigue loading frequency of 1-4Hz for glass fiber has been used with no adverse effect, therefore tests are performed at a frequency of 4Hz.

All fatigue tests are constant amplitude strain, tension-tension sine wave tests. The maximum and minimum load and displacement is recorded. The minimum stress on the specimens is 27.6MPa while the maximum load is determined as a fraction of the maximum stress of 318.75MPa. The magnitude of the minimum load was selected to be close to that used by Natarjan [13]. To determine the displacement amplitude to obtain the desired strain, a simple calibration procedure is performed: the specimen is loaded into the machine and a load that will produce the desired amount of stress is slowly applied and released, then applied and released a second time. When the specimen is unloaded there is a residual displacement sensed by the LVDT. This is due to the wedge grips tightening and the specimen slipping slightly before the full clamping force is realized. This zero offset only occurs during the first loading cycle, after that the displacement returns to zero when the load is returned to zero. To account for this nonlinear phenomenon the zero-offset is subtracted from the maximum displacement on the second loading cycle. The fatigue tests are then run at this displacement.

Once the fatigue coefficients are determined, the specimens with embedded FBGs can be tested. Prior to fatigue testing their temperature sensitivity must be characterized in order to account for the temperature change due to autogeneous heating. To do this the specimens and a bare FBG are placed in an oven with three thermocouples. The temperature in the oven is ramped up to 30°C, 40°C, 50°C and 60°C and allowed to soak at each temperature for one hour before the temperature and wavelength is recorded. A plot of

wavelength vs. temperature is constructed for each FBG and linear regression is used to extract an average temperature sensitivity of $0.031nm/^\circ C$ for the specimens and $0.010nm/^\circ C$ for the bare FBG.

4. Results and Discussion

A total of 11 static tests and 33 fatigue tests were performed. The results were processed and a number of test results were rejected due to factors such as their failure mode, outlying results or experimental procedure error. A total of three specimens with embedded FBGs were tested. One specimen was tested statically to determine the ultimate strain of the embedded FBG and two under constant displacement. Prior to fatigue testing, the specimens were calibrated with an extensometer to determine the strain sensitivity of the FBGs. During testing, a thermocouple was fastened to the surface of the specimen to monitor any temperature increase due to autogeneous heating. The FBG embedded specimen tested at a strain level of 0.4 was not tested until failure. The strain energy release rate was still obtained from the test however the number of cycles to failure was not. After the tests were completed and all requisite data was collected it was processed in order to apply the theory to predict the remaining useful life.

4.1. Material characterization test results

Static tests were performed in order to determine the ultimate stress and strain of the material that was later tested under fatigue. The ultimate stress and strain were found to be $318.75MPa$ and $16.31m\varepsilon$, respectively where $m\varepsilon$ is milli-strain.

Once the static tests were complete, the fatigue tests were performed. Peak strain and load data was converted into expended energy per cycle and plotted to produce an energy curve for each specimen as shown in Figure 3 (left). The aforementioned energy release trend is quite apparent in the energy curve plots; an example plot is shown in Figure 2.

Linear regression was used to obtain the energy release rate (dU/dN) throughout the linear region. The average energy release rate and ratio of U_f/U_0 for various levels of induced strain are presented in Table 1. The ratio U_f/U_0 (energy at failure, U_f (90% of total cycles) to initial energy U_0) is significant as it is used in the prediction of the remaining cycles in Equation (9). The average value of $r = U_f/U_0 = 0.856$ was used for predictions.

$\varepsilon_{max}/\varepsilon_{ult}$:	Energy Release Rate (J/cycle):	$r = U_f/U_0$:
0.4	8.705E-08	0.799
0.5	3.337E-06	0.826
0.6	3.352E-05	0.855
0.7	3.736E-04	0.885
0.75	1.307E-03	0.901
0.8	2.592E-03	0.917

Table 1: Fatigue test data

The energy release rate was plotted vs. normalized induced strain, Figure 3 (left). This data was averaged, plotted and fit to a power law curve to obtain the values for fatigue coefficients a and b , of 14.67 and 0.070595, respectively. With a and b determined, the fatigue life could be predicted using Equation (9). The experimental and predicted results are plotted as an $\varepsilon - N$ curve in Figure 3 (right). The number of experimental and predicted cycles to failure (N_f) and percent difference is shown in Table 2.

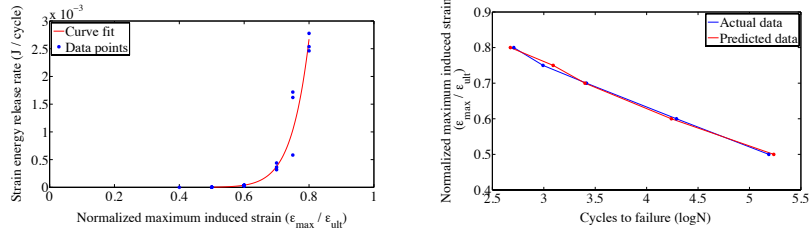


Figure 3: Variation of energy release rate (left) and $\varepsilon - N$ plot (right)

4.2. FBG embedded specimens

One problem that was immediately apparent was that as the FBG was strained, the reflected spectrum broadened, reduced in magnitude and split into multiple peaks making it difficult to accurately track. This is due to the uneven strain field caused by matrix cracking and the fiber reinforcement arrangement as documented by Takeda [5], [23], Shin [14], Okabe [24], Yashiro [25] and others. The peak splitting resulted in an inaccurate measurement of the strain magnitude, either greater or less than the actual strain. As the

$\varepsilon_{max}/\varepsilon_{ult}$:	Experimental N_f :	Predicted N_f :	Difference (%):
0.5	154108	185132	20.13
0.6	19510	17475	-10.43
0.7	2597	2389	-8.00
0.75	1233	982	-20.34
0.8	510	428	-16.17

Table 2: Fatigue life prediction results

peak split, the tallest peak would move to either side of the Bragg wavelength. The interrogator algorithm would track this peak rather than the center wavelength thus resulting in inaccurate strain values.

The reduction in magnitude also presented a problem. One of the settings of the interrogator software is the threshold of the magnitude of the reflected spectrum. The threshold must be set high enough to eliminate noise but not so high that the FBG reflected spectrum is excluded. Under low strain there was not enough of a reduction in magnitude to drop below the threshold, however as the strain increased towards the upper limits the magnitude reduced and in some cases dropped below the threshold causing the interrogator to momentarily lose the signal. This resulted in a number of data points that were recorded as 0. When the peaks were extracted from the full waveform data, missing peaks were given a value that was determined by interpolating between the neighboring peaks. Figure 4 shows the acquired signal from Specimen 3-1 for five second intervals of the fatigue test in the beginning (left) and end (right). The blue lines show the acquired data at an acquisition rate of $100Hz$ while the red circles indicate the peaks and troughs of the data that were extracted from the full waveform.

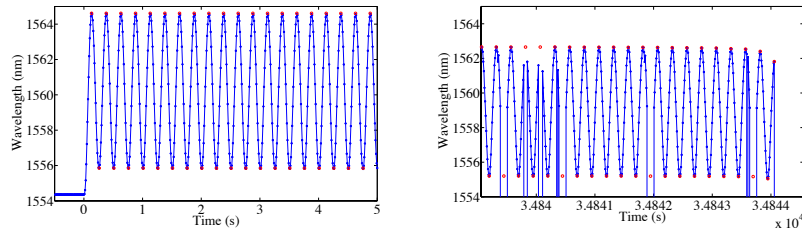


Figure 4: Wavelength vs. time for five second intervals at the beginning and end of the test

The surface temperature of the specimens that was monitored during the tests was converted into a wavelength value ($\Delta\lambda_B$) using the temperature sensitivity described earlier. The wavelength change due to temperature was subtracted from the FBG data.

The first test performed was a quasi-static tensile test to determine the ultimate strain level of the embedded FBG in Specimen 2-2. This information would provide a range of strain levels to conduct the fatigue tests.

Figure 5 shows a plot of strain measured with an extensometer on the left vertical axis and FBG wavelength on the right vertical axis vs. stress. Both strain and wavelength follow a linear increase until roughly 160MPa when there is a small jog in the FBG signal. This is likely due to the FBG reflected spectrum splitting and the peak moving to the lower range of the spectrum. After the jog the increase in the signal remains linear as expected. The strain level measured by the extensometer when the fiber optic broke was $10.323\text{m}\varepsilon$ while the FBG read $10.039\text{m}\varepsilon$ due to the shift. It is also worth mentioning that a loud 'ping' noise was heard when the fiber optic broke/signal was lost.

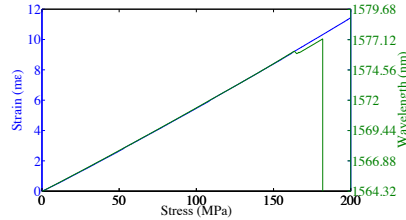


Figure 5: Wavelength and strain vs. stress

Before fatigue tests began, a simple strain characterization test was performed to determine the strain sensitivity of each specimen by straining it and monitoring the Bragg wavelength, displacement and strain in the specimen. FBG sensitivities of $1.2596\text{nm}/\text{m}\varepsilon$ and $1.2691\text{nm}/\text{m}\varepsilon$ were obtained for Specimen 3-1 and 4-2, respectively. The conversion from LVDT acquired displacement to strain was also obtained.

Specimen 3-1 was tested at a maximum induced strain of $0.5*\varepsilon_{ult}$. Figure 6 (left) shows the strain data vs. cycle number throughout the test. The blue line indicates LVDT acquired displacement data and the red line indicates FBG wavelength data. Both data sets are converted to strain for application to the prediction technique. The data measured with the LVDT shows a steady constant strain throughout the entire test as expected. The FBG data

however, initially shows a sharp increase due to autogeneous heating followed by a nonlinear decrease which leads to a linear decrease until roughly 13.5×10^4 cycles when it exhibits a sharp nonlinear decrease until failure. This shows the same trend as the load and is likely due to the break down of the composite resulting in a non-uniform strain field that causes the FBG peak to broaden.

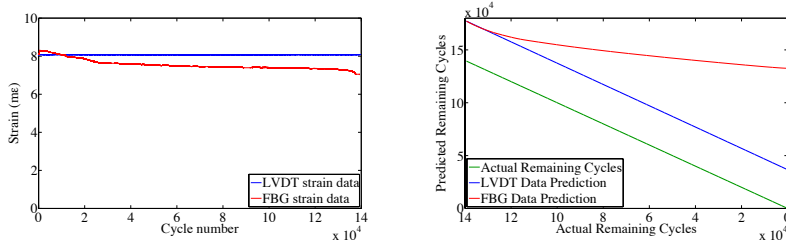


Figure 6: Results for Specimen 3-1: strain data (left) and prediction of remaining cycles (right)

Figure 6 (right) shows the prediction results from the data presented on the left along with the actual failure data. The prediction is made at every cycle based on data from the LVDT and FBG in blue and red, respectively. Since the LVDT data is constant, the predicted number of remaining cycles remains linear with a constant offset from the actual data. The error in these results is a function of the accuracy of the prediction method and experimentally determined fatigue coefficients from Equation (6). The predicted results are within 27% of the actual results at the beginning of the test. This larger than average difference compared to the average results shown in Table 2 can be attributed to the statistical variation in the material properties from specimen to specimen. The predicted results from the FBG data however, are not as accurate due to the reduction in magnitude of the strain signal. Since the prediction formula is based on a power law, a small variation in measured data can result in a large discrepancy between actual and predicted results. For the first 2×10^4 cycles the FBG prediction results are quite close to the LVDT prediction before they drift away to an unreasonable value.

In an attempt to subject the embedded FBG to a lower ε_{max} to obtain a more accurate signal, Specimen 4-2 was tested at a maximum induced strain of $0.4 \cdot \varepsilon_{ult}$. Figure 7 (left) shows the strain data vs. cycle number throughout the test. The blue line indicates LVDT acquired displacement data and the red line indicates FBG wavelength data. Clearly the signal from the FBG is

much closer to that measured by the LVDT than for Specimen 3-1. Naturally this results in a more accurate prediction of the remaining cycles as shown in Figure 7 (right).

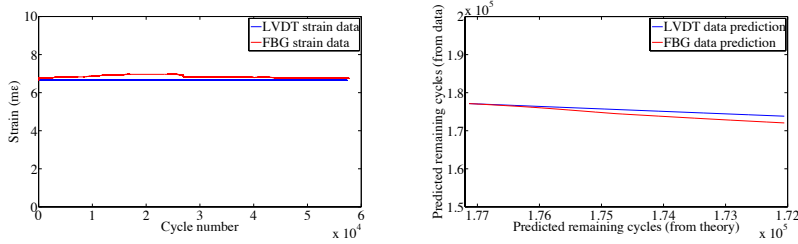


Figure 7: Results for Specimen 4-2: strain data (left) and prediction of remaining cycles (right)

Figure 8 shows a plot of the surface temperature of Specimen 3-1 on the left vertical axis and the applied load on the right vertical axis vs. percent of test. They are presented on the same plot in order to compare their similar trends. The temperature data (blue) shows a sharp increase during the first $\sim 5\%$. This is due to the autogeneous heating that occurs. After the initial peak there is a nonlinear decrease until $\sim 18\%$. After that there is some erratic fluctuation from $\sim 18\%$ to 55% which is likely due to external effects such as ambient temperature change. After that the decrease remains steady and linear until 95% when there is a final change to a greater decrease in temperature until failure. The load follows a very similar pattern aside from the initial sharp increase. From the first cycle to $\sim 15\%$ there is a nonlinear decrease before a constant linear decrease is observed until $\sim 95\%$ when a sharp nonlinear decrease occurs until failure.

Both data sets follow the trend of strain energy outlined in [13]. The temperature change is caused by the work done on the material. When there is a greater load applied then more strain energy is put into the material and therefore more autogeneous heating occurs. As the material starts to degrade and requires less load to reach the specified strain, less energy is put into the material and less heating occurs. Naturally there is a lag in the temperature signal due to the poor conductivity of glass fiber/epoxy composite.

This suggests that while susceptible to external environmental effects, monitoring the surface temperature of composites subjected to fatigue may be used to give insight into the condition of the material.

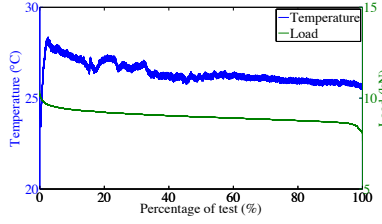


Figure 8: Temperature and load vs. percent of test

5. Concluding Remarks

After testing a total of 11 specimens statically and 33 in fatigue, the fatigue coefficients required to apply the strain energy release rate prediction model to a $[0/90]_{6S}$ glass fiber/epoxy laminate were obtained. In order to explore the concept of using FBGs to predict the remaining cycles throughout the fatigue life, three specimens with embedded FBGs were tested.

The results of the non-FBG embedded fatigue tests closely agreed with previous work by Natarjan [13] showing the same material degradation pattern.

The quasi-static test of the specimen with an embedded FBG showed that the ε_{max} of the embedded fiber optic is $\sim 10m\varepsilon$. The data also demonstrated the peak splitting phenomenon that results in an inaccurate strain level as shown in Figure 5.

During the fatigue test of Specimen 3-1, the recorded data from the FBG sensors did not closely match that of the LVDT displacement data rather its magnitude declined throughout the test. This is due to the degradation of the composite resulting in an uneven strain field in the region of the FBG causing the reflected spectrum to broaden and eventually split into multiple peaks. The algorithm used by the interrogation equipment records the peak with the largest magnitude, which is not always in the middle of the spectrum and therefore not an accurate measure of the strain.

The results of peak splitting is apparent when comparing the FBG data from tests conducted at $\varepsilon_{max}/\varepsilon_{ult} = 0.5$ and 0.4 . When the peak split during the first test, the tallest peak shifted to a lower wavelength and therefore the strain measured is less than the that of the actual strain while the opposite situation occurred with the latter test.

Due to the discrepancy in the FBG measured strain value and actual strain value, the predicted remaining life results are not highly accurate.

For the fatigue test performed on Specimen 3-1 ($\varepsilon_{max}/\varepsilon_{ult} = 0.5$) the FBG based prediction is close to the theoretical prediction for the first 20 000 cycles. The fact that the fatigue life equation is based on a power law results in a small discrepancy in strain producing a large discrepancy in predicted remaining cycles. The fatigue test performed on Specimen 4-2 ($\varepsilon_{max}/\varepsilon_{ult} = 0.4$) produced more accurate FBG strain data. Naturally, the FBG based prediction is much closer to the theoretical prediction for the latter test. A strain amplitude of $\varepsilon_{max}/\varepsilon_{ult} = 0.5$ was selected for the first test to decrease testing time however, in real life a strain of this magnitude would not be seen as the safety factor of composites is generally above 2, therefore a more reliable signal would be obtainable in real situations.

The introduction of Equations (10) and (11) to the fatigue life prediction technique developed by Natarjan [13] are novel, as is their approach to remaining useful life estimation that allows a prediction to be made at each cycle.

The conclusions drawn from these tests suggest that a more accurate and reliable signal from the embedded FBGs is required for accurate results. Three avenues to pursue in order to achieve this are: operate at lower strain level, investigate the use of shorter FBGs (1 – 3mm in length) and develop a more robust FBG interrogation algorithm. The ε_{ult} of carbon fiber is much lower than that of glass fiber meaning a structure composed of carbon fiber would see less strain and therefore an embedded FBG would not degrade as rapidly. To investigate this, the same study should be repeated with carbon fiber rather than glass fiber composites.

Acknowledgements

The authors gratefully acknowledge the funding provided by The Scientific and Technological Research Council of Turkey (TUBITAK) under the support program of scientific and technological research projects (1001), project number: 108M229.

References

- [1] G. Zhou, Damage detection and assessment in fibre-reinforced composite structures with embedded fibre optic sensors-review, *Smart Materials and Structures* (2002).
- [2] C. J. Keulen, M. Yildiz, A. Suleman, Multiplexed FBG and Etched Fiber

Sensors for Process and Health Monitoring of 2- & 3-D RTM Components, *Journal of Reinforced Plastics and Composites* 30 (2011) 1055–1064.

- [3] K. Kuang, Use of conventional optical fibers and fiber Bragg gratings for damage detection in advanced composite structures: a review, *Applied Mechanics Reviews* (2003).
- [4] C. Doyle, A. Martin, T. Liu, M. Wu, In-situ process and condition monitoring of advanced fibre-reinforced composite materials using optical fibre sensors, *Smart Materials and Structures* (1998).
- [5] N. Takeda, Characterization of microscopic damage in composite laminates and real-time monitoring by embedded optical fiber sensors, *International Journal of Fatigue* (2002).
- [6] S. Yashiro, N. Takeda, T. Okabe, H. Sekine, A new approach to predicting multiple damage states in composite laminates with embedded FBG sensors, *Composites Science and Technology* 65 (2005) 659–667.
- [7] N. Takeda, S. Yashiro, Estimation of the damage patterns in notched laminates with embedded FBG sensors, *Composites Science and Technology* (2006).
- [8] Z. Su, L. Ye, Y. Lu, Guided Lamb waves for identification of damage in composite structures: A review, *Journal of Sound and Vibration* 295 (2006) 753–780.
- [9] A. Othonos, K. Kalli, G. E. Kohnke, *Fiber Bragg Gratings: Fundamentals and Applications in Telecommunications and Sensing*, Artech House Inc., Boston, Massachusetts, (1999).
- [10] B. Harris, *Fatigue in composites*, Woodhead Publishing Limited, Cambridge, England, (2003).
- [11] S. W. Tsai, S. Ha, T. E. Tay, Y. Miyano, S. Shin, *Strength & Life of Composites*, Aero & Astro, Stanford U, (2008).
- [12] J. Degrieck, W. Van Paepegem, Fatigue damage modeling of fibre-reinforced composite materials: Review, *Applied Mechanics Reviews* 54 (2001) 279.

- [13] V. Natarajan, H. Gangarao, Fatigue response of fabric-reinforced polymeric composites, *Journal of Composite Materials* (2005).
- [14] C. Shin, Fatigue damage monitoring in polymeric composites using multiple fiber Bragg gratings, *International Journal of Fatigue* (2006).
- [15] A. Rotem, A Fatigue Failure Criterion for Fiber Reinforced Materials, *Journal of Composite Materials* (1973).
- [16] H. Whitworth, A stiffness degradation model for composite laminates under fatigue loading, *Composite structures* (1997).
- [17] H. A. Whitworth, Modeling Stiffness Reduction of Graphite/Epoxy Composite Laminates, *Journal of Composite Materials* 21 (1987) 362–372.
- [18] J. Yang, D. Jones, S. Yang, A stiffness degradation model for graphite/epoxy laminates, *Journal of Composite Materials* (1990).
- [19] W. Hwang, Fatigue of composites—fatigue modulus concept and life prediction, *Journal of Composite Materials* (1986).
- [20] W. Hwang, K. Han, Cumulative Damage Models and Multi-Stress Fatigue Life Prediction, *Journal of Composite Materials* 20 (1986) 125–153.
- [21] L. Lee, K. Fu, J. Yang, Prediction of fatigue damage and life for composite laminates under service loading spectra, *Composites Science and Technology* 56 (1996) 635–648.
- [22] H. A. Whitworth, Cumulative Damage in Composites, *Journal of Engineering Materials and Technology* 112 (1990) 358.
- [23] N. Takeda, S. Yashiro, T. Okabe, Estimation of the damage patterns in notched laminates with embedded FBG sensors, *Composites Science and Technology* 66 (2006) 684–693.
- [24] Y. Okabe, T. Mizutani, S. Yashiro, N. Takeda, Detection of microscopic damages in composite laminates with embedded small-diameter fiber Bragg grating sensors, *Composites Science and Technology* (2002).
- [25] S. Yashiro, T. Okabe, Estimation of fatigue damage in holed composite laminates using an embedded FBG sensor, *Composites Part A: Applied Science and Manufacturing* (2011).